UNIVERSIDAD DE CONCEPCIÓN
DIRECCIÓN DE POSTGRADO
FACULTAD DE INGENIERÍA - PROGRAMA DE DOCTORADO EN CIENCIAS DE LA INGENIERÍA CON MENCION EN INGENIERÍA QUÍMICA

ATOMISTIC STUDY OF FLOW ENHANCEMENT IN CERAMIC NANOPORES INDUCED BY GRAPHITIC COATINGS

POR

ENRIQUE IGNACIO WAGEMANN HERRERA
CONCEPCIÓN - CHILE 2018

Tesis para optar al grado de Doctor en Ciencias de la Ingeniería con mención en Ingeniería Química

Tutor: Dr. Harvey A. Zambrano
Departamento de Ingeniería Química
Facultad de Ingeniería - Universidad de Concepción

Co-tutor: Dr. Jens H. Walther
Departament of Mechanical Engineering
Technical University of Denmark

Advisor	:	Dr. Harvey A. Zambrano
Co-advisor	:	Dr. Jens H. Walther
Examination Committee	:	Dr. Eduardo Cruz-Chu
		Dr. Andrés Córdoba

A mis padres.

Abstract

Carbon nanotubes and graphene are nanostructured carbon allotropes that, as a result of their remarkable physical properties, hold a great potential to become the fundamental building blocks for a wide range of foreseeable functional nanodevices. In particular, these materials have demonstrated extremely low friction to water flow. Hence, attracting a great interest for being used as fluid conduits, integrating complex nanofluidic devices with applications in technological fields such as desalination, chemical separation, nanosensors and Lab-On-a-Chip units. The low friction measured between water and graphitic materials has been associated to the presence of slippage in the fluid-solid interface, which is a consequence of atomic level smoothness of graphitic surfaces and to the generally accepted weak interaction between these surfaces and water. Nevertheless, recent experiments have reported that the effect of airborne contaminants and the presence underlying substrates can alter significantly the wettability of graphene. Therefore, in order to achieve an optimal design of nanofluidic devices, a comprehensive understanding of slippage in a water flow confined between graphitic materials is still lacking.

In this thesis, we employ the molecular dynamics technique to study the fluid flow in pores fabricated with graphene layers and carbon nanotubes. In particular, the present work focuses in understanding how the physical properties of graphene, carbon nanotubes and underlying substrates determine the water flow through nanoconduits. Furthermore, an important aspect of the study is to measure the performance of graphitic materials to work as wall coating to reduce the hydrodynamic resistance in nanoconduits. Specifically, this thesis is divided in two main parts. The first part includes an introduction to the research field of nanofluidics and to the technique of molecular dynamics. The second part includes three research works and conclusions.

In the first research work, we conduct a study of water flow nanoconfined between parallel graphene layers at high shear rates. We observe that the crystallographic features of graphene influence the transition of the slip boundary condition at high shear rates, resulting in slip lengths that depend on the direction of the flow. In the second work we evaluate the use of graphene layers as wall coatings in silica nanochannels to induce a flow enhancement. Our models reproduce the experimental translucency to wettability of graphene coating on silica surfaces reported by Rafiee et al.. Moreover, we demonstrate that effectively the use of monolayer graphene as coatings induces an important flow enhancement, despite a decrease in the water contact angle and available channel cross section. Finally, we study the water flow enhancement, resultant of the use of carbon nanotubes as coatings on a cylindrical silica pore. In this study, the atomistic model of a silica pore coated by a single walled carbon nanotube is parametrized and characterized. Thereafter, the interactions between water and the pore are calibrated based on two possible scenarios that reproduce the same wettability. In the first scenario, the carbon nanotube is translucenct to the wettability of the underlying silica surface, thus water interacts with the carbon nanotube and the silica pore. The second scenario reproduces a carbon nanotube that is opaque to the interaction between underlying substrate and water, but whose wettability is tuned

through calibrating the interaction between carbon atoms and water molecules. Furthermore, we evaluate the properties of Poiseuille flow of water in the coated pore. Our results show an important variation in water flow as comparing the two wetting scenarios. We link this difference to the different energy corrugation that they reproduce. Nevertheless, both scenarios present important flow enhancement, demonstrating that the use of single walled carbon nanotubes is advantageous and therefore represents a potential option to reduce hydrodynamic losses in nanoconduits.

Resumen

Los nanotubos de carbono y grafeno son alotropos de carbono nanoestructurados que, como resultado de sus notables propiedades físicas, poseen gran potencial para convertirse en los bloques fundamentales para una gran variedad de aparatos nanofluídicos. En particular, estos materiales han demostrado una extremada baja fricción al flujo de agua. Por lo tanto, han atraído gran interés como conductos fluídicos, que podrian integrar complejos dispositivos nanofluidídicos con aplicaciones en campos tecnológicos como la desalinización, separación química, nanosensores y unidades Lab-On-a-Chip. La baja fricción entre agua y materiales grafíticos ha sido asociada a la presencia de deslizamiento en la interface sólido-fluido, lo que es una consecuencia de la suavidad a nivel atómico de la superficie del solido y de una generalmente aceptada débil interacción con agua. Sin embargo, experimentos recientes han reportado que el efecto de contaminantes adsorbidos y la presencia de substratos subyacentes pueden alterar significativamente la mojabilidad del grafeno. Por lo tanto, a fin de lograr un diseño óptimo de aparatos nanofluídicos, un entendimiento exhaustivo del deslizamiento interfacial en el flujo de agua confinado entre materiales grafíticos es aún requerido.

En esta tesis, empleamos la técnica de dinámica molecular para estudiar el flujo de fluido en poros fabricados con hojas de grafeno y nanotubos de carbono. En particular, el presente trabajo se enfoca en entender como las propiedades físicas del grafeno, nanotubos de carbono y substrato subyacente determinan el flujo de agua a través de nanoconductos. Además, un importante aspecto del estudio es medir el desempeño de los materiales grafíticos actuando como recubrimientos de pared para reducir la resistencia hidrodinámica en nanoconductos. Específicamente, esta tesis esta dividida en dos partes principales. La primera parte incluye una introducción al campo de investigación de la nanofluídica y a la técnica de dinámica molecular. La segunda parte incluye tres trabajos investigativos y conclusiones.

En el primer trabajo investigativo, realizamos un estudio acerca del flujo de agua nanoconfinado entre hojas de grafeno paralelas bajo altas velocidades de flujo. Observamos que las características cristalográficas del grafeno influencian la transición de la condición de deslizamiento bajo altas velocidades de flujo. En el segundo trabajo evaluamos el uso de hojas de grafeno como recubrimientos de pared en nanocanales de sílice para inducir una mejora en el flujo de agua. Nuestros modelos reproducen la translucidez experimental a la mojabilidad del grafeno en superficies de sílice reportada por Rafiee y colaboradores. Además, demostramos que el uso de grafeno monocapa efectivamente induce una importante mejora en el flujo, a pesar de la disminución en el ángulo de contacto del agua y en el área transversal disponible dentro el canal. Finalmente, estudiamos la mejora en el flujo de agua, resultante del uso de nanotubos de carbono como recubrimientos de pared en un poro cílindrico de sílice. En este estudio, el modelo atomístico de un poro de sílice recubierto por un nanotubo de carbono de pared simple es parametrizado y caracterizado. Posteriormente, las interacciones entre agua y el poro son calibradas en base a dos posibles escenarios que reproducen la misma mojabilidad. En el

primer escenario, el nanotubo de carbono es translúcido a la mojabilidad del substrato de sílice subyacente, por lo tanto el agua interactúa con el nanotubo y el poro de sílice. El segundo escenario reproduce un nanotubo de carbono que es opaco a la interacción entre agua y substrato subyacente, pero cuya mojabilidad se puede afinar a través de la calibración de la interacción entre moléculas de agua y átomos de carbono. Adicionalmente, evaluamos las propiedades del flujo de agua tipo Poiseuille en el poro recubierto. Nuestros resultados muestran una importante variación en el flujo de agua cuando ambos escenarios de mojabilidad son comparados. Asociamos esta variación a la diferente corrugación de la energía que ellos reproducen. A pesar de la diferencia en el flujo medido, ambos escenarios presentan una importante mejora en el flujo al ser comparados contra el flujo teórico, demostrando que el uso de nanotubos de carbono de pared simple como recubrimientos es ventajoso y por lo tanto representa una potencial alternativa para reducir las perdidas hidrodinámicas en nanoconductos.

Acknowledgements

First I would like to thank my advisor Harvey Zambrano for the opportunity to write this thesis. His mentoring, guidance and trust have been essential in my development as a researcher. I wish to express my gratitude to my co-advisor Jens Walther for his scientific mentoring and for his invaluable participation in this project. An special thanks to my colleague Elton Oyarzua for his friendship and scientific collaboration, but mostly for making of these four years a fun experience. I would also like to thank my colleagues at the Computational Nanolab; Diego, Nabin and Andrés for their company and the always interesting scientific and non-scientific discussions.

I would like to thank the Department of Physics and Mechanical Engineering at the Technical University of Denmark for the computational support and Petros Koumoutsakos at the Chair of Computational Science at ETH Zurich for allowing me to use the FASTTUBE package. Additionally, I wish to thank Centro CRHIAM Project Conicyt/Fondap No. 15130015 for partial funding this thesis.

I am deeply grateful to my family for their permanent support. In particular, I wish to thank my parents Enrique and Carmen Gloria, for their abiding love, their continuous help and for always encouraging me to reach my goals. They made all of my achievements possible. An special thanks to my godparents Lorenzo and Lorena for all their affection and support. They have always been there for me, specially in my times of need. A huge thanks to my beloved wife Francisca, for her patience, support, company, love and for giving me a reason to try being a better man.

Finally I would like to thank Lady Emily for her constant company. Without her this thesis would have been finished a year earlier.

Contents

List of Figures

List of Tables

Chapter 1

Introduction

The extraordinary optimization of the transport phenomena in physiological conduits, achieved by nature at the nanoscale, has inspired the scientific community to pursuit the current ongoing process of further miniaturization of technological devices. This dream set in motion a microtechnological revolution during the last quarter of the XX century, [6] that led to the development of functional micro-systems and demonstrated the benefits of extreme miniaturization. [7] More recently, technological advances have allowed unprecedented control over the fabrication processes at even lower scales, enabling the manipulation of matter at molecular and atomistic levels. [8] As a result, a new technological field has emerged, Nanotechnology. This field promises novel applications, tied to novel processes and integrated fluidic devices with unparalleled efficiencies. Nevertheless, great promises require enormous efforts to become reality. Therefore, before we can start dreaming of functional and efficient nanoscale integrated devices, a thoroughful knowledge of the transport phenomena at the nanoscale is required.

From a classical fluid mechanics point of view, the required energy to pump a fluid through a channel is directly related to the friction imposed by the wall surfaces of the channel in contact with the fluid. Hence, this friction is tightly related to the ratio between surface area and confined fluid volume, that increases drastically at lower scales. [9] Consequently, huge amounts of energy are required to produce flows in nanoconfinded geometries, and new strategies for reducing hydrodynamic losses in nanoconduits are essential for the development of efficient intregrated nanofluidic systems. In biological cells, nature has tackled this problem by optimizing the entrance geometry of transmembrane channels such the aquaporins entrance, while maintaining them short. [10] However, engineering applications are likely to require channels of considerable larger lengths (tens to hundreds of nm) than those in cell membranes with typical thickness within few nm, making the need for new strategies to reduce hydrodynamic drag in artificial nanochannels.

Due the enormous ratio between wall surface and confined fluid volume in nanoconduits alters hydrodynamic properties such as interfacial slippage, it represents a great opportunity to achieve further optimization of transport phenomena at the nanoscale. [11,12] Scientific evidence has associated the presence of hydrodynamic slip at the solid-liquid boundary to the particular smoothness of the solid material [13–16] and to a relative weakness of the solid-liquid interaction. [16, 17] A class of materials that shares these properties, among many others, are the graphitic materials. In particular, carbon nanotubes and graphene display an extremely low resistance to water flow. [18–29] Owing to this finding, these materials have attracted great interest over the last two decades, as promising nanomaterials for channels with wide range of applications, such as desalination, [30] nano Lab-On-a-Chip units [31] molecular sieving and chemical separation

membranes. [32] Consequently, they are one of the most prominent candidates to become basic building blocks for future nanofluidic devices.

The generally accepted hydrophobicity of graphene has been the subject of intense debate, due to recent reports on the effect of airborne contaminants on the wettability of supported graphene and graphite. [33, 34] These studies suggest that graphitic materials are more hydrophilic than previously expected and that the widely accepted hydrophobicity of graphitic materials is caused by adsorbed contaminants. Additionally, reports on the effect of the underlying substrate on the wettability of supported graphene has put the spotlight on our understanding of graphene-water interface. Indeed, an intense debate started with the so-called "transparency to wettability" of graphene reported by Rafiee et al. in 2012. [35] Through the measurement of the water contact angle on substrates coated by an increasing number of graphene layers, the authors suggest that a monolayer graphene does not disrupt the interactions between the underlying substrate and water. Not long after, Shih et al. [36] demonstrated that, despite being an atomically thin material, graphene cannot be transparent to the wettability of the substrate, but "translucent", i.e., semi-transparent. Further studies have expanded this debate, by reporting translucency to wettability, [37–41] whereas others contradict it. [42,43] The translucency to wettability can open the door to very important nanofluidics applications. Therefore, it is an interesting phenomena that deserves further investigation.

In this thesis, trough molecular dynamics simulations, we evaluate the use of graphitic materials to induce an enhancement in nanoconfined flow of water. The research consists of three major studies. In the first study, we investigate the effect induced by the crystallographic features of graphene on the nanoconfined flow of water at high shear rates. In the second study, we evaluate how the use of single layer graphene as coatings on silica nano channels can induce an enhancement in the flow of water. Finally, we extrapolate the translucency to wettability of graphene to its allotrope, carbon nanotubes, and evaluate the water flow enhancement induced by employing single walled carbon nanotubes as coatings in a cylindrical silica nano pore.

1.1 Outline of the Thesis

This thesis is structured as follows:

Chapter 2 - Nanofluidics. This chapter consists of a brief introduction to nanofluidics and reviews relevant interfacial phenomena, such as wettability, slippage and interfacial fluid structuration. Moreover, a description of carbon nanotubes and graphene and their properties is included.

Chapter 3 - Computational simulations of atomistic systems. This chapter comprehensively reviews the molecular dynamics technique employed in the present work to simulate the studied systems.

Chapter 4 - Water flow in graphene nanochannels: Slip divergence and the role of chirality. In this chapter MD simulations of the flow of water confined between graphene layers at high shear rates are performed. The effect of the crystallographic features of graphene is studied by changing the direction of the flow.

Chapter 5 - Monolayer graphene-based coating to induce water flow enhancement in silica nanochannels. In this chapter MD simulations of water flow confined inside of a silica channel, internally coated by graphene monolayers, are conducted to evaluate the reduction of hydrodynamic losses induced by the coatings.

Chapter 6 - Reduction of viscous losses in silica nanopores induced by carbon nanotube

coatings. In this chapter, the atomistic model of a cylindrical silica nanopore, coated by a single walled carbon nanotube is created and characterized. Then, the effect of the translucency to wettability of atomically thin materials on the hydrodynamic properties of water is studied by simulating the flow of water confined within the pore.

Chapter 7 - Conclusions.

Chapter 2

Nanofluidics

Nanofluidics is, in a broad sense, a subdiscipline of fluid mechanics that studies the behavior, manipulation and control of fluids inside and around nanoscalar structures, i.e. structures in which at least one characteristic dimension is in the nanometer order ($1 - 100\,\text{nm}$). [44, 45] As a subdiscipline of fluid mechanics, it has inherited many classical tools, methodologies and knowledge from its macroscalar counterpart. However, despite tremendous effort has been devoted to investigate fluid behavior in nanoconfinement, [10, 11, 13, 17–20, 29, 46, 46–74] a comprehensive understanding of fluid dynamics in nanochannels and nanopores is still lacking. Indeed, as confinement is increased and the system size is reduced approaching the atomic domain, some effects non-familiar to the classical fluid mechanics start to come up, making classical equations and assumptions incapable to provide precise predictions of the fluid behavior in the nanoscale. [46]

In nanoconfined fluid flows, the extremely large ratio between contact area and confined fluid volume derives in fluid phenomena highly influenced by the system surfaces, [6] making the interaction between walls and fluid a non trivial subject. Therefore, comprehensive understanding of the physical phenomena in the fluid-solid interface becomes crucial to achieve a proper description of a fluid in nanoconfinement. In this chapter, interfacial phenomena relevant to this thesis are reviewed.

2.1 Fluid-solid interfacial phenomena

As confinement increases and the thickness of the solid-fluid interface becomes comparable to the available width, interfacial effects become dominant. Therefore, proper understanding of the interfacial physics is key to describe and predict the hydrodynamic properties of the fluid in the nanoscale. This section will discuss some relevant physical phenomena related to the solid-liquid interface.

2.1.1 Wetting

Wetting is the ability of a liquid to spread over a solid surface. This property is a result of the balance between the adhesive and cohesive intermolecular forces that arise from the interaction of three phases; solid, liquid and gas. This phenomena is typically quantified through the contact angle (θ), represented on Figure 2.1. In this figure three interfaces can be observed (SL, LV and SV), each one with its respective surface tension (γ). The intersection line between the three interfaces (O) is known as the contact line and is the location where the contact angle is

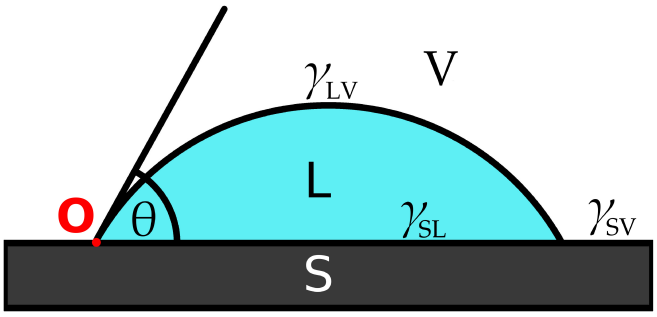

Figure 2.1: Water contact angle of a droplet on top of a solid surface. Source: Own elaboration.

measured. Depending on θ, the solid is commonly described as hydrophilic, as θ tends to 0 and complete wetting is achieved or hydrophobic if θ is higher than 90°.

In the macroscale, wetting phenomena can be accurately described through equation 2.1, that corresponds to the Young's equation and represents a balance between the tensions imposed by each surface on the contact line and simplified for a planar system. [75]

$$\cos\theta = \frac{\gamma_{SV} - \gamma_{SL}}{\gamma_{LV}} \tag{2.1}$$

However, for microscopic size droplets the tension produced on the triple phase contact line gains importance and produces a deviation between the measured macroscalar and microscalar contact angle. A common approach to capture this effect is to modify the Young's equation by by including a term that depends on the size of the droplet, resulting on: [71, 76–79]

$$\cos\theta = \cos\theta_{\infty} - \frac{\tau}{\gamma_{LV}}\frac{1}{r} \tag{2.2}$$

where θ_{∞} represents the macroscopic contact angle that can be predicted using the unmodified version of the Young's equation, τ is the line tension, γ_{LV} is the surface tension in the liquid-vapor interface and r is the droplet radius. The term $\frac{\tau}{\gamma_{LV}}$ is expected to be a constant, therefore it is possible to estimate a macroscopic angle by measuring the contact angle in microscopic droplets of varying size and applying a linear fit to the obtained values. [80]

2.1.2 Fluid structuration at the solid-liquid interface

The interaction between solid and liquid in the vicinity of the surface gives rise to the so-called solvation forces. These forces are short ranged and oscillatory in nature and depend not only on the fluid properties, but also on the chemical and physical characteristics of the solid. [81] As a consequence of these forces, the interfacial fluid tends to order itself in layers normal to the surface of the solid. The interfacial ordering or structuration manifests as oscillations in the density profile of the fluid that decay towards the bulk density far away the solid surface. [75] In Figure 2.2 we present an example of the radial density profile of water confined inside a carbon nanotube.

In the same way as solvation forces do, the interfacial structuration properties depend on the solids surface characteristics. Among the solid properties that have an effect on the fluid structuration we can find:

- Wettability; Wettability is highly influenced by the strength of the interaction between solid and fluid. Therefore, wettability has a strong influence over the fluid structuration in the interface. [57]
- Surface chemical groups; The presence of hydrophilic groups on the solid surface can generate a local order towards them on polar molecules such as water, that can affect the rest of the fluid structuration. [82]
- Surface roughness; In smooth surfaces the fluid structuration will have no ordering within the layers. Surface roughness can modify this behavior by introducing a disruption to the solvation forces. As a consequence, it is possible to observe no interfacial ordering on high roughness surfaces. [75]
- Periodic lattice structure In the same way surface roughness can modify the liquid structuration, periodic lattice structures on the solid can produce a lateral ordering within fluid layers. For instance, the crystalline characteristics of carbon nanotubes induce a structuration on the water confined within them. [13, 52]

If confinement is increased, the ratio between interfacial and bulk fluid thickness is expected to increase. Therefore, the properties of the overall fluid in nanoconfinement will not only depend on the bulk properties, but also on the interfacial ones. For instance, it has been reported that an increase in confinement leads to a decrease in the effective viscosity of the confined fluid. [28] Moreover, if confinement is further increased to a regime wherein the bulk condition is no longer present, the fluid becomes purely interfacial and thus the solvation forces will tend to overlap, resulting on interfacial structuration properties that depend non-monotonically on the available volume. [18, 20, 28, 52]

In the particular case of water nanoconfined between graphitic surface, fluid structuration in the interface plays a key role in the determination of the hydrodynamic properties of the fluid. [12] For instance, the overall fluid density inside carbon nanotubes is highly influenced by the diameter of the tube. [52] The interaction between water and carbon atoms produces an oscillatory density profile of the interfacial water, that leads to a decrease in the overall density of the fluid with the reduction of the nanotube diameter. For nanotubes of smaller diameter, water becomes a non-continuum fluid whose molecules order themselves in a single line parallel to the nanotube axis. [83] Furthermore, the crystallographic features of graphitic materials can also induce an arrangement of the fluid, tangential to the surface of the solid. [13] The tangential ordering of the fluid highly influences the interfacial slippage of water on these materials. [13,14]

2.1.3 Slip boundary condition

Over the last two centuries one of the main foundations of the classical fluid dynamics has been the no-slip boundary condition, namely the assumption that the liquid adjacent to the solid surface moves at the same speed as the surface. [11, 84] Despite not being based on any physical principle, [69, 85] the no-slip boundary condition has prevailed due to its proven accuracy in the description of macroscalar viscous flows. [11, 15, 85, 86] Nevertheless, in the last decades this assumption have been called into doubt, due to the continuously growing evidence of interfacial

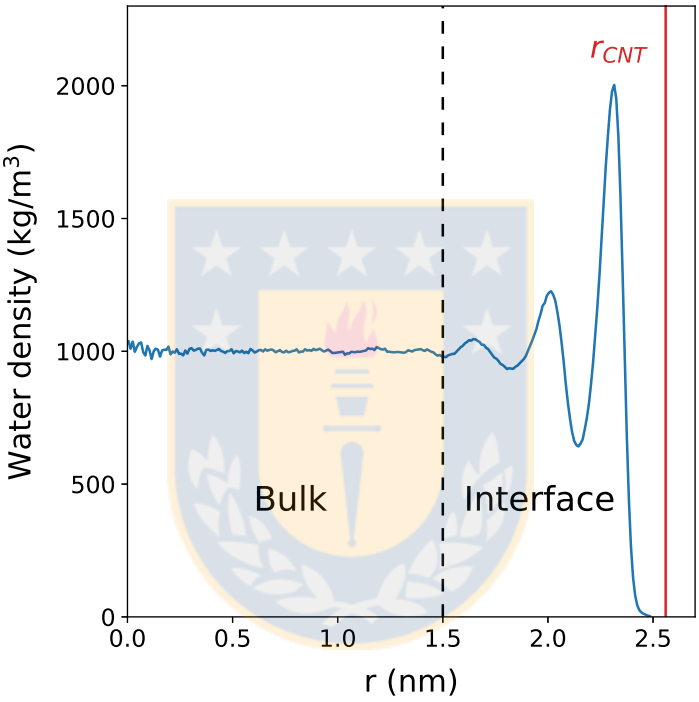

Figure 2.2: Radial density profile of water confined inside a carbon nanotube. The density profile presents oscillations near the carbon nanotube wall that decay towards the bulk of the fluid in the center of the nanotube. Source: Own elaboration.

slip of Newtonian fluids on the micro and nanoscale coming from experiments [21,51,84,85,87,88] and computational simulations. [14–16, 23, 49, 89, 90] Furthermore, while minor deviations from the no-slip boundary conditions may have negligible effects on macroscale liquid flow behavior, they could be of great significance in micro and nanofluidic systems. [91] Moreover, interfacial slip leads to a decrease in the hydrodynamic resistance to transport a fluid in a channel. [11] Therefore, proper understanding and control of the slip phenomena are of major importance in the development of novel nanofluidic devices.

Slippage is commonly quantified through the slip length (l_s), [11] proposed by Navier. [92] The Navier slip boundary condition (equation 2.3) defines that the slip velocity (u_s), i.e. the difference between the tangential velocity of the fluid and the solid surface, scales proportionally with the shear rate at the interface ($\frac{\delta u}{\delta y}$). [86] Furthermore, the proportional factor between the u_s and $\frac{\delta u}{\delta y}$ corresponds to l_s.

$$u_s = l_s \frac{\delta u}{\delta y} \tag{2.3}$$

The slip length can be interpreted as the distance between the solid surface and the virtual point where the velocity becomes zero, [6] as depicted in Figure 2.3. In the most common situation l_s is finite and associated with a positive slip velocity. [75] However, if the interaction between solid and fluid is sufficiently strong, the interfacial fluid can stick to the wall, [86] resulting in a negative l_s. Note that a l_s equal to zero recovers the no-slip boundary condition.

In general, the slip length is known to increase with the water contact angle (WCA) [11, 17, 38, 49, 50] and decrease with the surface roughness. [11, 38, 87] Therefore, hydrophobic surfaces with smooth roughness are expected to present an important slippage. However, other factors can also have an influence on l_s. In particular, there is evidence that the shear rate can modify l_s. [16, 51, 62, 73, 84, 93] This situation, although controversial, can result in a transition of the boundary condition from no-slip to slip with constant l_s at low shear rates, [51] or from constant to increasing and unbounded l_s at high shear rates. [90] In Chapter 4 we study the transition of l_s at high shear rates and how the crystallographic features of the solid surface, in particular the structural anisotropy of graphene, can have an influence on it.

For a more detailed description of interfacial slip and the phenomena involved we refer the reader to [11, 50, 87].

2.2 Graphene and Carbon nanotubes as fluid conduits

Graphene (GE) and Carbon nanotubes (CNT) are two nanostructured carbon based materials that hold great importance for the development of novel application in nanotechnology based devices. [94] Since the "rediscovery" [95] of the CNTs by Iijima et al. in 1991 [96] and the first report of the synthesis, identification and characterization of stable monolayer GE by Geim, Novoselov and collaborators in the early 2000s, [97, 98] these materials have brought enormous attention from the scientific community due to their remarkable electronic, chemical and mechanical properties. [94, 99] This section provides a brief description about CNTs and GE.

2.2.1 Graphene

Graphene is a two-dimensional material [100] formed by sp^2-hybridized carbon atoms, [101] ordered in a single atom thick crystalline honeycomb structure. This hexagonal unit is also the fundamental unit for other carbon allotropes, such as fullerenes, CNTs and graphite. [100] Hence,

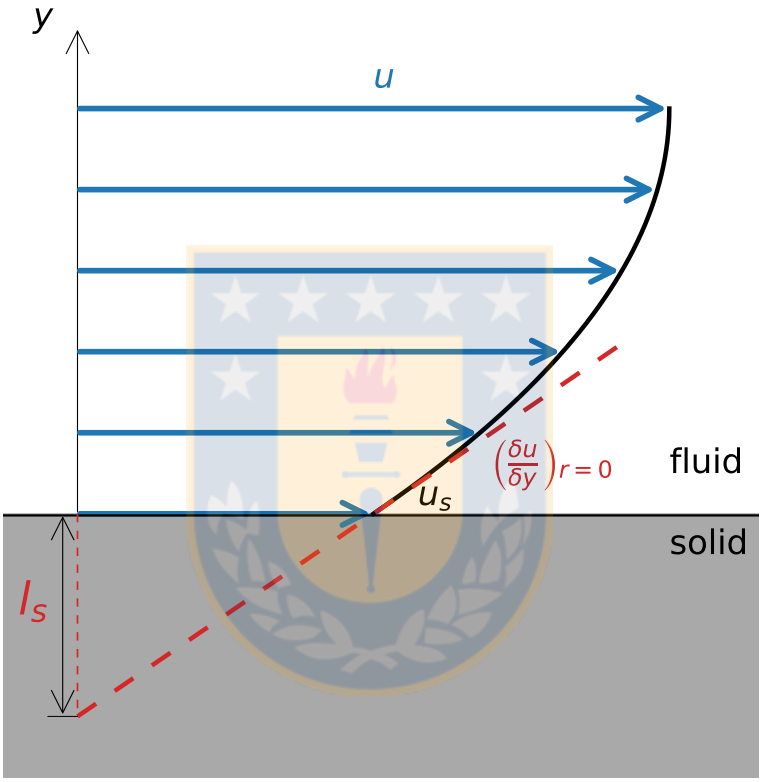

Figure 2.3: Schematic representation of the Navier slip boundary condition. u denotes the velocity of the fluid, u_s denotes the velocity of the fluid at the surface, i.e., the slip velocity and l_s denotes the slip length. Source: Own elaboration.

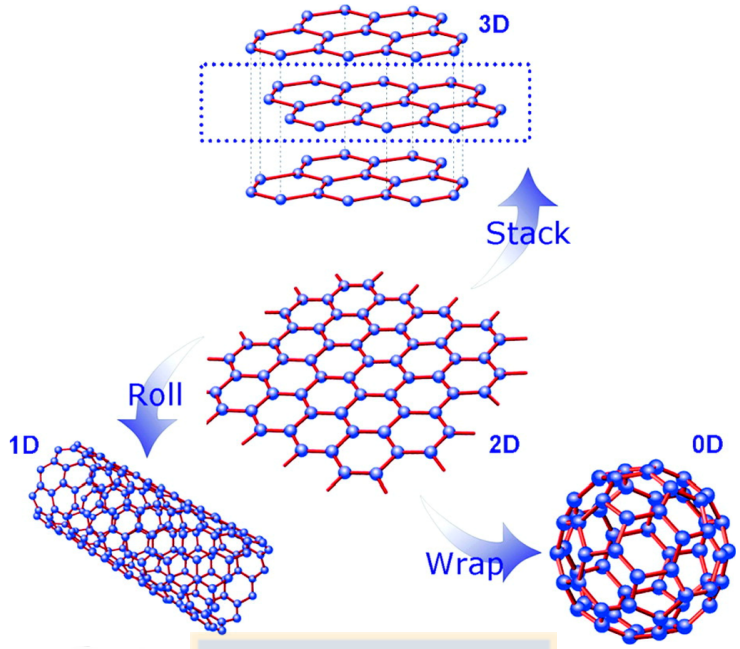

Figure 2.4: Graphene as the basic building block for other carbon allotropes. A fullerene is obtained by wrapping a graphene sheet, CNT by rolling it and by stacking monolayer graphene, graphite is obtained. (Reprinted from ref. [1])

by applying physical transformations to graphene it is possible to obtain the three mentioned allotropes, as depicted in Figure 2.4. Therefore, graphene can be considered the "mother" of this family of carbon allotropes. [94, 99, 100] Before the work of Geim and Novoselov, [97, 98] two dimensional crystals were thought to be thermostatically unstable. [100,102,103] Thus, graphene was considered merely an "academic" material used to describe the physical properties of the other allotropes. [100,102] Consequently, the experimental synthesis of graphene attracted great attention and inspired the ongoing search of novel 2D materials, [104] their unique properties and possible applications. [105] In particular, graphene has shown excellent physical properties, such as high electric [106] and thermal [107] conductivities, large flexibility [108] and optic transparency, [109] making it a promising material for a wide range of applications. [99,102] For a more detailed description of graphene, its properties and possible applications we reefer the reader to the literature. [94, 99, 110, 111]

2.2.2 Carbon nanotubes

Carbon nanotubes (CNT) are hollow cylinders formed by the same hexagonal fundamental unit than graphene. [99, 103, 111, 112] CNTs can be classified by the number of conaxial graphitic walls that compose them, into single walled CNT (SWCNT) or multi walled CNT (MWCNT). SWCNT have a diameter that can range from 0.3 nm [113] to 5 nm, [102] whereas the diameter of MWCNT can range from few nanometers to tens of nanometers. [102] Moreover, CNTs can have very large length to diameter ratios (with lengths up to several microns). [114] Therefore, CNTs are deemed as one dimensional structures. [110]

If considered as a rolled graphene sheet (Figure 2.4) the atomic structure of CNTs can be classified by the chirality vector ($\vec{C}_h$) of the tube, i.e., the direction on which the sheet is rolled.

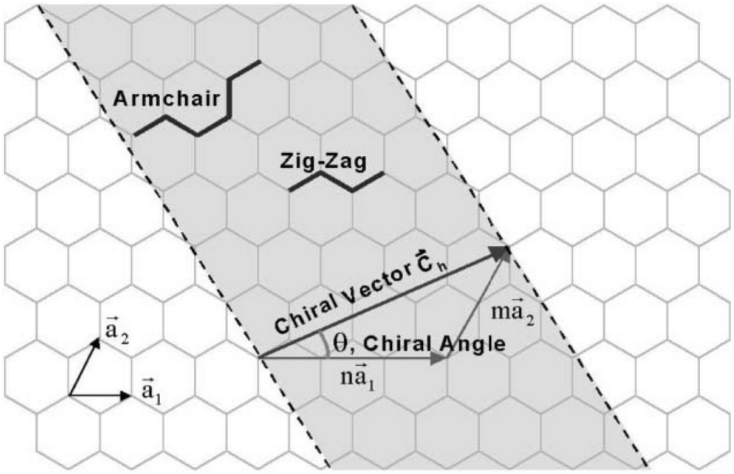

Figure 2.5: Schematic representation of the chiral vector. (Reprinted from ref. [2])

The chirality vector can by described by the following equation:

$$\vec{C}_h = (n, m) = n\vec{a}_1 + m\vec{a}_2, \quad \text{where} \quad (n, m) \in \mathbb{N},\ n \geq m \tag{2.4}$$

$\vec{a}_1$ and $\vec{a}_2$ are unit vectors which are depicted in Figure 2.5, along with $\vec{C}_h$. The chirality vector has two limiting values; $n = m$, classified as "armchair" CNTs and $m = 0$, corresponding to "zig-zag" nanotubes. Intermediate cases are deemed as "chiral" CNTs. The chirality of a CNT has an important influence over the physical properties of the tube. For instance, armchair CNTs are metallic, whereas zig-zag and chiral CNTs can be semimetals if $\frac{n-m}{3} \in \mathbb{N}$, otherwise they are semiconductors. [114] Furthermore, the diameter of the CNT can be estimated by the following equation:

$$D_{CNT} = \frac{l_0}{\pi}\sqrt{3\left(n^2 + nm + m^2\right)} \tag{2.5}$$

where l_0 is 0.142 nm and represents the length of the C-C bond. [115]

Due to the structural features of CNTs, they are employed in macro and nanoscale devices as a structural reinforcement in composite materials. [111] In addition, since a CNT is a cyllindrical hollow structure, they are promising candidates to become nanofluidic conduits. [112]

2.2.3 Flow of water confined inside carbon nanotubes and graphene channels

Experimental studies reporting faster than expected water transport in aligned carbon nanotubes membranes in the early 2000s, [25, 27, 116] attracted a considerable interest to the flow of water nanoconfined between graphitic surfaces, due to the potential uses in a wide range of applications, such as water desalination, [30] nanodelivery [112] and Labs on a Chip. [31] Fast water transport has been linked to an ultra-low friction owing to a significant interfacial slip velocity between water and the graphitic surface, [13, 18, 19, 28, 60, 117, 118] that translate into large slip lengths. Studies based on computational simulations have revealed that these large slip length are a result of the surface smoothness of the graphitic materials [13, 14] and a generally accepted weak interaction between the carbon atoms and water. [18, 28] Moreover, confinement can also have an influence in the fluid transport, as there is evidence that the effective lip length in CNTs decreases monotonically with larger nanotube diameter, [18, 20, 60] approaching the slip length

in a planar graphene surface at large diameters. [18] This variation in the effective slip length has been linked to confinement, as it can produce a decrease in the effective water viscosity inside CNTs, due to the increase in the ratio between interfacial and overall sectional area. [28, 117] In this study, we take in consideration all these mentioned factors, in order to evaluate how the water transport nanoconfined between different graphitic surfaces can achieve an enhancement when compared to the flow of water confined between hydrophilic silica surfaces.

2.2.4 Graphene transparency to wettability

In 2012 Rafiee et al. [35] reported measurements of WCA over several substrates, with a varying number of coating graphene layers. Their experimental results showed that the WCA increased as the number of graphene sheets increases, with a value approaching the one measured on graphite. Furthermore, the WCA measured on substrates that typically interact with water through van der Waals interactions, coated by monolayer graphene, was similar to the one measured on the respective uncoated substrate. Nevertheless, they also found that for glass, a substrate whose wettability is highly influenced by the hydrogen bonding with water, [54] the measured contact angle was neither the one measured on the bare substrate, nor the one measured on graphite, but a value in between. They called this new property of graphene, "wetting transparency". Furthermore, this wetting transparency is related to the extreme thinness of graphene, and thus the capability of the fluid to still interact with the underlying substrate despite the barrier represented by the graphene layer between them.

Not long after, Shih et al. [36] explored further this phenomena by conducting theoretical, computational and experimental works. Their results showed that the separation between fluid and substrate, imposed by the monolayer graphene, was large enough to screen some of the interaction between them, and thus claimed that graphene could not be transparent to wettability, but "translucent". [119] Moreover, they demonstrated that wettability of the coated substrate was also influenced by the strength of the interaction between solid and fluid, explaining the results of Rafiee et al.. [35] Further studies about the degree on which graphene is translucent to wettability support this idea, [37–41] whereas others contradict it. [42, 43] Therefore, the transparency to wettability has been a subject of intense debate. Another important aspect of graphene wettability is the recently reported effect of the adsorbed airborne contaminants over the measured WCA on graphene. [33] Furthermore, more recent studies have intensified this debate as they have proven that chemical or voltage doping modify the Fermi level of graphene, and consequently the interaction between graphene and water. [120, 121]

The translucency to wettability of graphene could have important technological applications [35] due to the chemical stability of graphene when lying on a substrate. [122] Hence, graphene layers could be employed as a passivation layer, thus avoiding undesired surface chemical effects and maintaining active part of the interaction between underlying substrate and fluid. Nevertheless, it could also present issues, as the resulting increase in the coated substrate wettability can reduce the interfacial slippage, [17, 117] when compared to pristine graphene. Therefore, in order to design efficient nanofluidics devices based on graphitic coatings, a comprehensive knowledge of the influence of the underlying substrate on the wettability and interfacial slippage of the supported graphene is required.

In chapter 5, we evaluate how a graphene monolayer coating can induce an flow enhancement when compared to the bare substrate, in a coated silica channel with walls that reproduce the WCA reported by Rafiee et al.. [35] We explore further the effects of wetting translucency over the nanoconfined water flow in chapter 6, by extrapolating this effect to the, also atomically

thin, walls of CNTs.

2.3 Computational modeling of nanofluidic systems

Computational methods have played an important role to understand the behavior of nanoconfined fluids complementing experiments and providing new insights. [13, 15, 28] In particular, Molecular Dynamics (MD) simulations provide an atomistic description allowing detailed studies of the solid-liquid interfaces, capturing the effects from applied fields and the molecular ordering which dominate flows in and nanostructures. [13, 20] In this thesis, a systematic study of transport mechanisms to drive fluid in nanoconfinement is reported. Specifically, large-scale massively parallel Non-Equilibrium MD simulations are conducted to study the interfacial phenomena of water in contact with graphitic surfaces and how its implementation in nanofluidic devices could lead to a reduction in the energy consumed to pump water in nanoconduits. The following chapter reviews some important concepts of the MD technique employed in this study.

Chapter 3

Computational simulations of atomistic systems

The rapid increase of the available computational power during the second half of the 20th century [123] has provided the tools for the development of a new, now consolidated, branch of science; the computational modeling and simulation of physical systems. [124] The use of computational simulations has allowed the study of a wide range of physical systems, that increase in complexity from simple gases [125,126] to complex biological systems. [127–129] In this technique, physical phenomena are described by mathematical models which consist of a representation of the system of interest and a set of rules determining the behavior of the system. Moreover, computer simulations have been capable to provide useful information and predict the behavior of systems whose complexity has rapidly increased over time. When compared to experimental approaches, simulations are advantageous in the sense that they give control over most (if not all) the involved variables, complementing experiment but also allowing to study phenomena that can not be captured experimentally by the current technology. [130] But of course, due to the inherent nature of simulations, the quality of the predictions is tied to the goodness of the employed models and the properties they are capable of reproducing. In that sense, computational simulations will never surpass experimentation. Nevertheless, thanks to the marriage between computational simulations and strong theoretical background, important advances in science have been made. [131–133]

When it comes to simulating physical systems two main approaches can be distinguished; continuum and non-continuum approaches. [124] As their names hint, the main difference between these two descriptions is the way on which matter or physical properties are modeled. In the first one, matter is generally depicted as a continuum medium, with physical properties described by balance equations with boundary conditions obtained from experiments and/or theoretical predictions. A good example of continuum based methods is the Computational Fluid Dynamics (CFD) technique, that numerically solves the Navier-Stokes equations under different initial and boundary conditions. This technique has proven to be of great utility in simulating many multiscalar phenomena, [134–136] although tends to fail when the scale is reduced and the influence of the discrete nature of matter rises. [137] On the other hand, non-continuum approaches describe matter as a collection of discrete components and is the interaction between these components who rules the reproduced physical properties. In simulations based on non-continuum approaches the interactions between particles are described by mathematical models which include parameters which should be obtained or calibrated from experiments and/or first principles studies. An

example of this kind of approach are quantum and molecular methods. The quantum methods rely on a quantum chemistry description of atoms, by solving a simplified electronic Schrodinger equation. [138] This simplification is possible due to the Born-Oppenheimer approximation, that decouples the motion of the electrons and nucleus that conform an atom. [139] These techniques are capable of capturing and reproduce quantum phenomena or predict how atoms interact, but due to the high computational cost involved they are limited to small size systems. [124] In contrast, molecular methods describe atoms as mass points (or in some cases charge points) that interact through empirical energy potential functions. [124,139,140] Examples of molecular approach based methods are the Monte Carlo (MC), Molecular Mechanics (MM), and Molecular Dynamics (MD) techniques.

3.1 Modeling particle interactions

In methods based on a molecular description of matter, the interactions between particles are modeled using empirical energy potential functions or just potentials for simplicity. These potentials can be divided into two groups, non-bonding and bonding interactions. Moreover, the total potential energy of a system is the result of the sum of the potential energy of each interaction. [124]

$$U(r^N) = U_{Nonbonding} + U_{Bonding} \tag{3.1}$$

In an effort to maintain simplicity and reducing computational costs, potentials are generally "pairwise", i.e., the interaction between two particles is modeled as function of the distance between them. [4] Although, higher order potentials that include terms to capture the influence of third bodies can be found on the literature. [130]

3.1.1 Nonbonding or intermolecular potentials

The interaction between two particles that are not bonded is usually divided in two parts, long ranged and short ranged. [141] Short ranged interactions include attractive and repulsive forces resultant of London dispersion and Pauli repulsion respectively, while long ranged include forces arising from atomic electrostatic charges.

Short ranged van der Waals interactions

Potentials that model the van der Waals interactions between particles are required to reproduce a repulsive force when the particles are close to each other i.e., Pauli repulsion, and an attractive force i.e., London dispersion [81] if they pull apart. [141] Short range particle description has historically evolved from rigid sphere models, [142] to the modern soft sphere potentials. The later generally contains a repulsive term that quickly increases as particles move closer each other and an attractive term that decays as particles move away.

Lennard-Jones potential

One widely used potential is the so-called Lennard-Jones (LJ). This potential is composed of an attractive term that decays as r^6 and a repulsive term that grows as r^{12} and tends asymptotically

to infinity as r becomes zero.

$$U_{\alpha\beta}(r_{\alpha\beta}) = 4\varepsilon_{\alpha\beta}\left[\left(\frac{\sigma_{\alpha\beta}}{r_{\alpha\beta}}\right)^{12} - \left(\frac{\sigma_{\alpha\beta}}{r_{\alpha\beta}}\right)^{6}\right] \tag{3.2}$$

where $\varepsilon_{\alpha\beta}$ represents the potential depth, $\sigma_{\alpha\beta}$ is the distance where the potential becomes zero and $r_{\alpha\beta}$ is the distance between the center of mass of the particles. By replacing the exponent of the repulsive or attractive terms, alternate forms of the LJ potential can be derived. [141] For example a 18-6 LJ potential has the form:

$$U_{\alpha\beta}(r_{\alpha\beta}) = 4\varepsilon_{\alpha\beta}\left[\left(\frac{\sigma_{\alpha\beta}}{r_{\alpha\beta}}\right)^{18} - \left(\frac{\sigma_{\alpha\beta}}{r_{\alpha\beta}}\right)^{6}\right] \tag{3.3}$$

Buckingham potential

Based on the electronic structure theory, that states that repulsion comes from the overlap of electronic wave functions, [139] the Buckingham potential replaces the repulsive term in the LJ potential with an exponential term. The Buckingham potential has the following form,

$$U_{\alpha\beta}(r_{\alpha\beta}) = \alpha_{\alpha\beta}e^{\left(-\frac{r_{\alpha\beta}}{\rho_{\alpha\beta}}\right)} - \frac{C_{\alpha\beta}}{r_{\alpha\beta}^{6}} \tag{3.4}$$

where $\alpha_{\alpha\beta}$, $\rho_{\alpha\beta}$ and $C_{\alpha\beta}$ are adjustable interaction parameters.

Long ranged electrostatic interactions

Electrostatic interactions produce forces resultant from the interplay between charged particles. [139] A common approach to describe these charged particles is to assign partial charges, located at the center of mass of each atom, as point charges. [139] By following Coulomb's law [139] it is possible to compute the potential energy between two charged particles as Equation 3.5.

$$U(r_{\alpha\beta}) = \frac{q_\alpha q_\beta}{4\pi\epsilon_0 r_{\alpha\beta}} \tag{3.5}$$

where q_α and q_β represent the partial charges of the involved particles and ϵ_0 is the vacuum permittivity. Alternatives for the efficient computation of the long ranged electrostatic interactions are discussed in section 3.2.6.

3.1.2 Bonding or intramolecular potentials

Potential energy due to bonding interactions is generally modeled by the sum of three contributions, where each one corresponds to one of the basic internal movements that a molecule can do; bond stretching, angle bending and bond torsion, [140] as depicted in Figure 3.1.

$$U_{bonding} = U_{bond} + U_{angle} + U_{torsion} \tag{3.6}$$

The potential energy curve, resultant of the stretching and lengthening of a molecular bond is properly described by a Morse potential, [140] that has the form:

$$U(l) = D_e\{1 - \exp[-a(l - l_0)]\}^2 \tag{3.7}$$

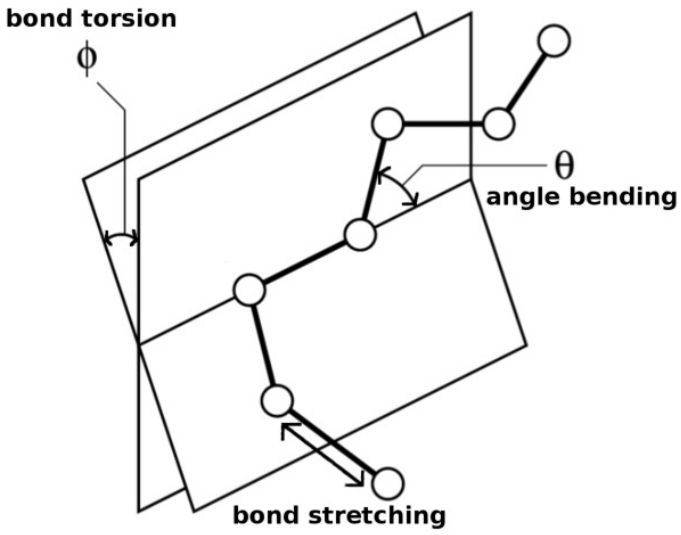

Figure 3.1: Schematic representation of the three basic internal movements of a molecule; bond stretching, angle bending and bond torsion. (Adapted from ref. [3])

where D_e corresponds to the minimum potential energy, a is a constant that depends on the frequency of the bond vibration and l_0 is the bond's reference length. Another bonding potential corresponds to a derivation of the Hooke's law. This potential describes the bonds vibration as a harmonic motion. [140] The vibration frequency of this potential can be tuned through the force constant k_l. The Hooke potential has the following form:

$$U(l) = \frac{k_l}{2}\left(l - l_0\right)^2 \tag{3.8}$$

The angle bending term is usually described using the Hooke's law model: [140]

$$U\left(\theta\right) = \frac{k_\theta}{2}\left(\theta - \theta_0\right)^2 \tag{3.9}$$

where k_θ is a force constant and θ_0 is the reference angle. A variation to this potential corresponds to the harmonic cosine potential: [124]

$$U\left(\theta\right) = \frac{k_\theta}{2}\left(\cos\theta - \cos\theta_0\right)^2 \tag{3.10}$$

Usually bond vibration and angle bending represent most of the contribution to the bonding potential energy, therefore many force fields do not include a bond torsion term, although it gives information about the structural properties of molecules [140]. In contrast, force fields used to describe organic molecules include the bond torsion term due to the particular complexity of the molecules involved. The bond torsion potential is usually expressed as a cosine series expansion: [124]

$$U(\omega) = \sum_{n=0}^{N} \frac{V_n}{2}\left[1 + \cos\left(n\omega - \gamma\right)\right] \tag{3.11}$$

where V_n corresponds to an adjustable constant that gives qualitative information about the rotation barriers [140] and γ is a face factor that give the angle reproducing the lowest energy configuration. Potentials that capture more complexity and include more variety of internal movements can be found on literature. [140]

3.2 Molecular Dynamics

The molecular dynamics technique is a computational method that describes matter as a collection of discrete elements representing atoms or molecules that interact dynamically with each other via empirical potential energy functions. [5, 130] MD has been used to study, model and predict a wide range of physical phenomena, such as thermodynamic properties of fluids [143,144] or solids [145–147], biological systems, [128, 133, 148] fluid dynamics, [18, 20, 149] among many others. [131] This technique relies on the Newton's second law of motion to describe the dynamic behavior of each particle: [5]

$$\vec{f}_i = m_i \vec{a}_i \tag{3.12}$$

with the force acting on each particle estimated from the potential energy resultant of each pairwise interaction that involves the particles in the system of interest:

$$\vec{f}_i = -\sum_{1}^{j \neq i} \frac{\partial}{\partial \vec{r}_i} U(r_{i,j}) \tag{3.13}$$

note that each atom is described by its type, mass, charge, coordinates ,i.e., position inside the simulation box and instantaneous velocity.

In this work all simulations are carried out by employing the FASTTUBE molecular dynamics package. [150] This package has been extensively used to study liquids confined inside carbon nanotubes, [151] wettability of graphene surfaces, [80] imbibition of water into silica nanopores, [59,65] thermophoretic phenomena, [66, 67, 152, 153] electrokinetic transport of aqueous solution inside silica nanochannels, [68,154] and transport of water in contact with graphitic surfaces. [23]

3.2.1 Numerical integration of the equations of motion

In MD simulations, the equations of motion are solved using a finite difference method that discretizes time into small time steps, [5] separated by an interval δt. In each time step the force acting over each particle is computed and then, by using the Newton's second law of motion, the acceleration of each particle is calculated. Based on the calculated acceleration, the new position, velocity and acceleration of the atoms is updated via the use of Taylor series expansions. [5,140].

$$r(t+\delta t) = r(t) + v(t)\delta t + \frac{1}{2}\delta t^2 a(t) + \frac{1}{6}t^3 b(t) + \frac{1}{24}\delta t^4 c(t) + ... \tag{3.14}$$

$$v(t+\delta t) = v(t) + \delta a(t) + \frac{1}{2}\delta t^2 b(t) + \frac{1}{6}\delta t^3 c(t) + ... \tag{3.15}$$

$$a(t+\delta t) = a(t) + \delta t b(t) + \frac{1}{2}\delta t^2 c(t) + ... \tag{3.16}$$

Several algorithms based on the previous Taylor expansions of the position, velocity and acceleration of a particle are used to update the particles properties. In particular, the Leap-frog algorithm [155] updates the atoms position from a velocity computed in a half time step $t + \frac{1}{2}\delta t$:

$$v\left(t+\frac{1}{2}\delta t\right) = v\left(t-\frac{1}{2}\delta t\right) + \delta t \cdot a(t) \tag{3.17}$$

$$r(t+\delta t) = r(t) + \delta t \cdot v\left(t+\frac{1}{2}\delta t\right) \tag{3.18}$$

The velocity at a time t can be computed as:

$$v(t) = \frac{1}{2}\left[v(t+\frac{1}{2}\delta t) + v(t-\frac{1}{2}\delta t)\right] \tag{3.19}$$

The error of this algorithm scales with t^3 and while it explicitly computes velocity, it cannot directly compute the potential and kinetic energy at the same time due to the fact that the computation of velocity and position are not simultaneous. [5]

3.2.2 Thermodynamic ensembles

An ensemble is a large number of realisations of a system, all considered at the same time, where each one of them represents a possible state of the system. [124] Consequently, a thermodynamic ensemble consist of all possible states and microstates of a system that is being restricted in base to properties that characterize a macroscopic system. The concept of ensemble has great importance in molecular dynamics, as based on principles of statistical mechanics, they allow to extract macroscopic properties from averaging the behavior of the particles inside a microscopic system. [4] There are several thermodynamic ensembles, each one representing a macroscopic system and therefore useful for the study of different experimental scenarios. In particular two ensembles are employed in this study:

- **Microcanonical (NVE):** This ensemble describes an isolated system, i.e., a system that has a constant number of particles, volume and energy over time.
- **Canonical (NVT):** This ensemble describes a system that is in equilibrium with a thermal bath at an specific temperature, i.e., a system that has a constant number of particles, volume and temperature over time.

Thermostat

The canonical ensemble describes a system that is in weak contact with a thermal bath. To reproduce this situation in a MD simulation the use of thermostats is required. Four basic methodologies are used to couple the system to a thermal bath: [124]

- Coupling through the use of stochastic forces that act over random particles.
- Strong coupling through exact correction of the kinetic energy.
- Weak coupling through perturbations to the particles velocity.
- Extension of the system dynamics, while increasing the degrees of freedom.

In this work system temperature is controlled by employing the Berendsen thermostat. [156] This thermostat uses the weak coupling method by rescaling the particles velocities after being computed by the equations of motion. The temperature change due to the thermostat following:

$$\frac{dT}{dt} = \frac{T_0 - T}{\tau_T} \tag{3.20}$$

where T_0 is the temperature of the thermal bath and τ_T is a coupling constant. The value of the coupling constant rules the coupling strength between bath and system. The velocity of each particle coupled to the thermostat will be rescaled using a scaling factor defined as:

$$\lambda = \sqrt{1 + \frac{\delta t}{\tau_T}\left(\frac{T_0}{T} - 1\right)} \tag{3.21}$$

3.2.3 Simulation box and periodic boundary condition

A simulation box corresponds to a virtual volume that contains the simulated system. The chosen size and shape of the studied simulation box will depend on the properties and characteristics of the studied system. Moreover, it is a common practice to employ periodic boundary condition (PBC) in MD simulations. This means that an array of replicated images is defined, each one connected to the original simulation box. Each particle inside the original box interacts with the nearest image or particle in the periodic array, following the minimum-image convention. [3] Furthermore, if a particle leaves the simulation box through one of its faces it will return through the opposite boundary of the simulation box. This situation is depicted in the two dimensional example presented in Figure 3.2. In this figure a particle leaves the simulated box (red) and enters the contiguous replicated image of the simulation box. The use of PBC allows to study bulk properties, while avoiding the need of explicitly imposing boundary conditions. [5] Consequently, the required system size and computational cost are reduced.

3.2.4 Cut-off radius

The computation of each pairwise interaction in the system requires the calculation of the distance between each simulated particle and subsequently, to obtain the forces, the evaluation of each potential involved within each interaction. This pairwise determination of the forces between particles is known as the numerical N-body problem, which requires an enormous number of calculations. [157] To reduce the required computational cost the use of cut-off radii can be implemented. [139] A cut-off radius (r_{cut}) truncates a potential in a specified distance, which means that if the distance between two particles is larger than r_{cut}, their interaction will not be computed. [86] Of course, the use of such a scheme produces discontinuities in the involved forces and the total energy of the system becomes non-conservative. To tackle these problems, the use of shifted and smoothed potentials is implemented. In the shifted potentials, a shifting function is employed to modify the entire potential function in a way that the energy becomes zero in r_{cut}. In the other hand, switched potentials use smoothing functions to modify the "tail" of the potential function to ensure that it remains continuous and smoothly becomes zero in r_{cut}. [139] Examples of truncated, shifted and switched Coulomb potentials are presented in Figure 3.3. Note that the chosen r_{cut} must be large enough to capture the relevant part of the interaction.

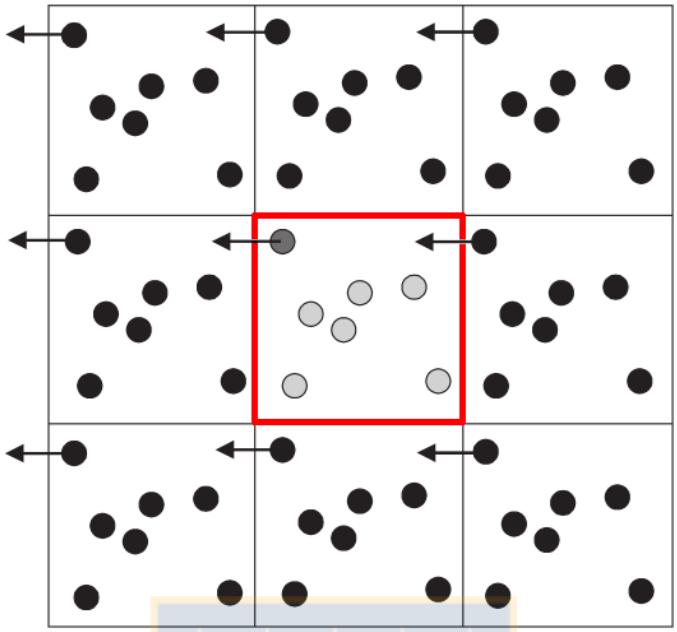

Figure 3.2: Two dimensional representation of the imposed periodic boundary condition and replicated images array. (Adapted from ref. [4])

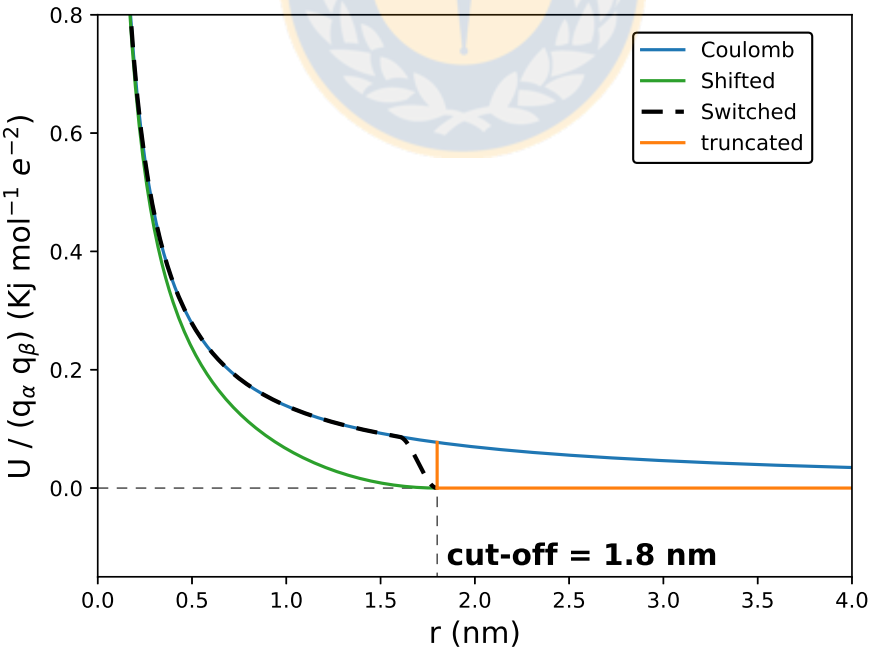

Figure 3.3: Difference between original, truncated, switched and shifted Coulomb potentials. A cut-off radius of 1.8 nm is employed in this example. Source: Own elaboration.

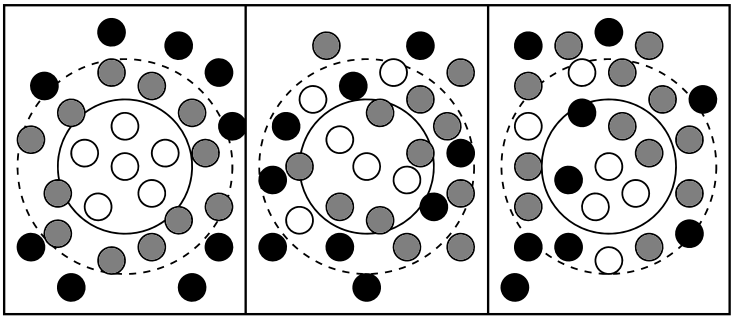

Figure 3.4: Two dimensional representation of the Verlet neighbor lists. The continuum line represents r_{cut} and the discontinuous one r_{list}. (Reprinted from ref. [3])

3.2.5 Neighbor list

While the use of cut-off schemes represents a reduction in the number of required computations, the evaluation of the particles distances still represents an enormous computational cost. [3] To tackle this problem, in 1967 Verlet suggested the use of the now called Verlet neighbor lists. [158] This method consists in the use of lists for each particle that contains all the particles within a r_{list} distance during a specific period of time. Before each successive integration, the distance between paired particles in these lists is computed. Therefore, this methodology significantly reduces the number of pairwise distances that are evaluated. A graphical representation of this method is depicted in Figure 3.4. Note that in order to ensure that all the interactions within r_{cut} are computed, r_{list} must be larger than r_{cut}. Of course, due to the dynamic nature of the systems in a MD simulation, the lists must be updated over time. Consequently, the r_{list} distance and frequency of the update during a simulation have to balance computational efficiency and precision. In that sense, larger lists result in a greater computational cost, however requiring a lower update frequency. [3]

An alternative to the Verlet neighbor lists, that is specially useful for large systems, is the use of cell-lists. This method divides the simulation box into smaller cells of dimensions equal to r_{cut}. The distance between particles is computed between particles within the same cell and between particles of neighbor cells. The update of the cells is faster than the Verlet neighbor lists algorithm, therefore it can be done in each integration time step. [3]

3.2.6 Ewald summation

Electrostatic interactions are of long ranged nature, which means that they slowly decay with the distance separation between charges. In some applications, direct truncation of these potentials is not suitable. [139] In contrast, direct computation of the Coulomb potential can represent a enormous computational cost due to the large amount of interactions that must be computed in a typical molecular simulation. Computing pairwise the electrostatic potential energy between all the particles on a cubic simulation box of L dimensions and its periodic images through the Coulomb potential requires the evaluation of:

$$U_{electrostatic} = \frac{1}{2} \sum_{N^{\circ}boxes=0}^{6} \sum_{i=1}^{N} \sum_{j=1}^{N} \frac{q_i q_j}{4\pi\epsilon_0 |r_{\alpha\beta} + L|} \tag{3.22}$$

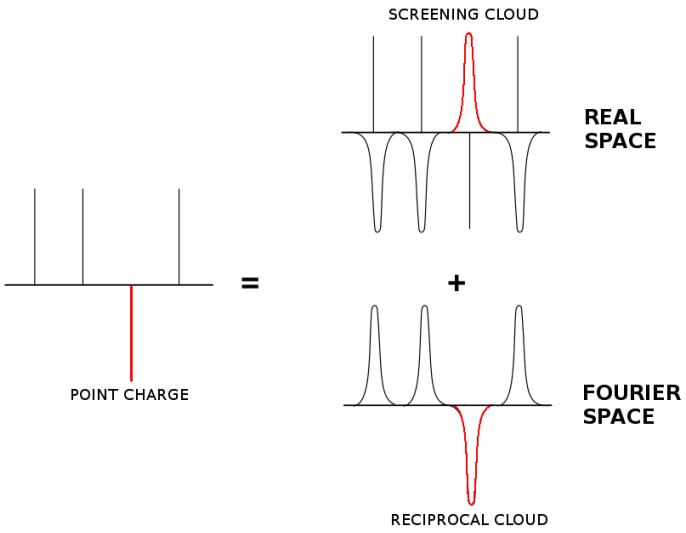

Figure 3.5: Graphic representation of the Ewald summation. (Adapted from ref. [5])

which converges very slowly and also conditionally. [5] In the Ewald summation method this direct calculation is replaced by a faster converging series, composed of a near-field and a far-field term. [139] The near-field contribution is obtained by screening each point charge by a diffuse electronic cloud of opposite charge. This electronic cloud has a Gaussian distribution of its charge density (eq. 3.23) and decays quickly with the distance. Following this assumption, it is not required to compute the interaction between point charges beyond the screening cloud. In fact, an increase in the overall system charge is induced. Therefore, an equal cloud with opposite charge must be included to compensate the artificially increased charge. This mathematical game is represented on Figure 3.5.

$$\rho_{Gauss}(r) = -q_i(\alpha/\pi)^{\frac{3}{2}} \exp\left(-\alpha r^2\right) \tag{3.23}$$

Where α is an ‘ parameter that gives shape to the charge distribution. The resulting potential energy from the interaction with a charge distribution is computed using a Fourier transform, resulting on an expression with faster convergence:

$$U_{electrostática} = \frac{1}{2V}\sum_{k\neq 0}\frac{4\pi}{k^2}|\rho(k)|^2 \exp\left(-k^2/4\alpha\right) - (\alpha/\pi)^{\frac{1}{2}}\sum_{i=1}^{N} {q_i}^2 + \frac{1}{2}\sum_{i\neq j}^{N}\frac{q_i q_j \mathrm{erfc}(\sqrt{\alpha} r_{\alpha\beta})}{r_{\alpha\beta}} \tag{3.24}$$

This expression includes the contribution of three terms; the reciprocal term that corresponds to the contribution of the reciprocal cloud, the constant or self term and the real space term of the screened point charge with its correspondent cloud. [159] Note that this expression requires two cut-off radii, k_c and r_c, one for the Fourier space and the other for the real space. It is convenient to use the same value for both cut-off, because most of the studied systems involve short and long ranged interactions. [5]

Mesh based methods

Although the use of Ewald summation represents a significant improvement in the required com-

putational cost when compared to the direct evaluation of the Coulomb potential. Nevertheless, the computational cost of the Fourier space term of the Ewald summation scales with $N^{3/2}$, making it inefficient for large systems. [5] A more efficient alternative for the evaluation of the reciprocal space of the Fourier transform is the use of particle-mesh approaches, which efficiently compute discretized forms of the Poisson equation via the interpolation of the point charges into a grid via the use of the Fast Fourier Transform. [159] In the same way that the Ewald summation method does, particle mesh methods are divided into a short-ranged and a long-rage contribution, being the first one computed directly and the second one using a particle-mesh scheme. The implementation of these methods reduces the computational cost to a minimum of $N \log N$. [159] Nevertheless, these particle-mesh approaches can be imprecise due to the interpolation involved, hence the mesh has to be fine enough to reduce the imprecisions related to the interpolation. Examples of these methods are Particle Mesh Ewald (PME), [160] that evaluates the forces by analytically differentiating the energies and a modified version of this method; Smoothed PME (SPME), [161] that computes the reciprocal sums through the B-spline interpolation of the reciprocal space structure factors onto a regular grid.

Chapter 4

Water flow in graphene nanochannels: Slip divergence and the role of chirality

Parts of this chapter have been published in: Enrique Wagemann, Elton Oyarzua, Jens H. Walther, and Harvey A. Zambrano. "Slip divergence of water flow in graphene nanochannels: the role of chirality." *Physical Chemistry Chemical Physics*, 2017, 19(13), 8646-8652.

4.1 Introduction

Nanoscale fluid dynamics has attracted considerable interest as part of the current fascination with nanotechnology and the consequent attempt to design and fabricate integrated nanofluidic devices such as Lab-On-a-Chip (LOC) units and nanoscale sensor systems. [162–166] The flow of water in nanoconfinement has been extensively studied, [13, 21, 51, 167, 168] however many fundamental questions remain open and are yet the subject of intense debate. It is well recognized that the physics of fluids at the nanoscale is dominated by the large surface-to-volume ratio inherent to this scale, [18,21,24,59,65,153] thus interface transport phenomena greatly impacts the fluid behavior. [69,169–171] Technologically, nanofluidics has become interesting as the basis for further miniaturization of microfluidic devices. Indeed, the possibility of extending the LOC concept to the nanoscale, the potential role of carbon nanostructures as highly efficient fluid conduits, [21, 24, 27, 116, 167, 172] the development of novel drug storage units, biochemical devices, nanofilters and nanosensors are paradigmatic examples of the importance of nanofluidics.

Graphene is a carbon allotrope which consist of a single plane sheet of carbon atoms arranged in a symmetric hexagonal lattice. [100] The chirality of a graphene sheet is determined by the in-plane orientation of the hexagonal lattices. [173] The isolation of a single sheet of graphene [98,100] has led to the fast development of many promising applications [110,174–176] including its potential utilization in a wide variety of functional parts in nanofluidic devices. [177–179] Therefore, a comprehensive understanding of transport of water confined inside or in contact with graphene layers is important for the design of nanofluidic devices. [58]

In macroscale fluid dynamics, the multi centenary assumption of a no-slip boundary condition at solid walls is in the core of our understanding of fluid transport. [180] Nevertheless, over years persistent doubts have been expressed. [15, 21, 58, 88] Indeed, studies of flow in micro- and nano-confinement have found a constant slip length in Newtonian liquids. [19] Furthermore,

recent investigations have concluded that the amount of slip depends on the local shear rate at the solid surface [16, 51, 73, 181] therefore the slippage is velocity dependent. Moreover, the wettability of graphene with respect to water is still not well understood [33, 35, 36, 42] and a topic widely investigated in recent years. Furthermore, faster than expected water flow rates have been observed in carbon nanotubes and graphene channels, [18,21,27,116] which have been attributed to an extremely low friction of water with the atomistically smooth walls. [13, 14] This low viscous drag makes graphene a promissory coating material to mitigate hydrodynamic losses in nanochannels.

In this study, we conduct large scale and long time (more than 60 ns) atomistic simulations to investigate water flow dynamics inside graphene nanochannels. Specifically, effects of channel height and graphene chirality on the amount of slip are investigated by computing flux, flow rates, critical shear stress, friction coefficients and flow enhancement. Here, we consider how a Newtonian fluid flow inside a graphene channel responds to variations in the lattice orientation of the confining graphene walls. Our results provide insights into prediction of fluid transport in hydrophobic nanostructures which is essential to develop functional nanofluidic devices.

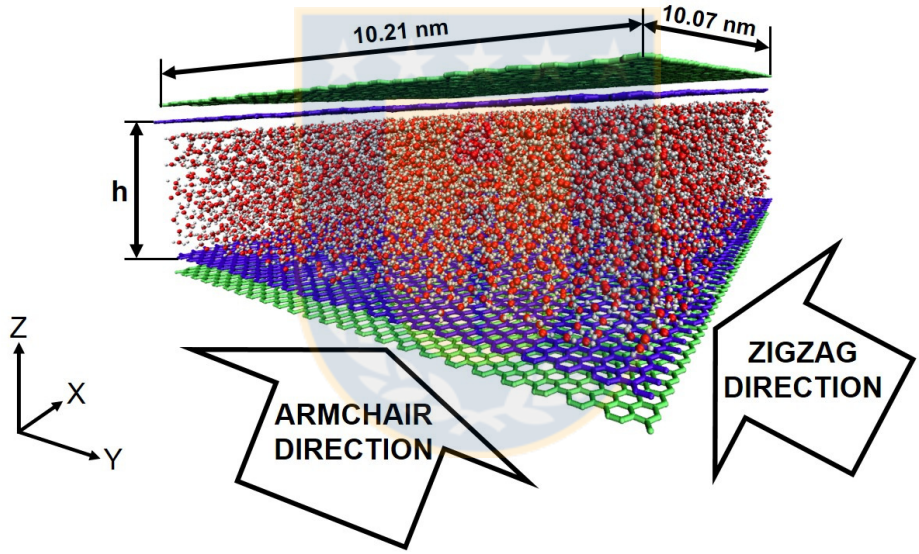

Figure 4.1: Snapshot of the studied graphene channel systems. Water is confined between two walls conformed by two graphene sheets each (green and blue). Two additional fixed graphene layers (not shown) that do not interact with water are used to confine the system. Source: Own elaboration.

4.2 Methodology

To study the hydrodynamical properties of water confined in graphene nanochannels we conducted a series of Equilibrium and Non-Equilibrium Molecular Dynamics (NEMD) simulations. All simulations were carried out using the FASTTUBE MD package which has been used extensively to study liquids confined inside carbon nanotubes and silica channels. [59, 65, 80, 150, 152,

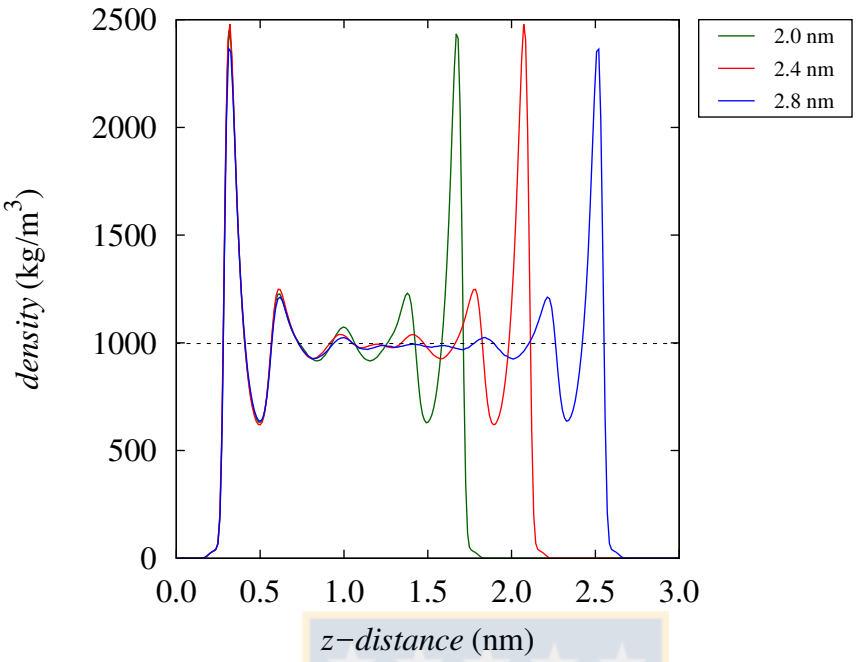

Figure 4.2: Water density profiles inside the graphene channels, for the different studied channel heights. Source: Own elaboration.

153, 153] Our systems confine water between two walls of graphene. The walls consist of parallel A-B stacked bilayers of graphene. [182]

A snapshot of the studied systems is shown in Figure 4.1, where h corresponds to the channel height which is defined as the mean distance between the centres of mass of the carbon atoms in the innermost graphene layers. An orthorhombic box is used with periodic boundary conditions in x and y directions, while free space conditions are applied in the z direction. The x and y dimensions are chosen to minimize artificial strain [118] in the graphene sheet due to the periodic boundary conditions. Two external fixed graphene layers which do not interact with the water molecules are implemented. These layers are added to confine the system thus avoiding the necessity of fixed carbon atoms in the inner layers interacting with water.

To achieve an internal pressure of 1 bar, a size dependent number of water molecules is placed between the graphene walls. Subsequently, one of graphene walls is used as a piston to impose the target pressure and then the carbon atoms in the most external layer are fixed to reproduce a channel with the required mean height. We take special care of the confinement of the system, as the internal pressure is known to affect the slip length. [60, 183] It should be noted that the two inner graphene sheets are maintained flexible and free in all directions during the simulations. Density profiles, presented on Figure 4.2, show bulk and interfacial density in good agreement with previous works [80, 118] and exhibit no difference between the correspondent armchair (AC) and zig-zag (ZZ) cases. The number of water molecules per system are: 5500 water molecules for the 2 nm height channel, 6900 for the 2.4 nm channel and 8310 molecules for the 2.8 nm for the channel with a height of 2.8 nm. After imposing an axial force on the confined water, an initial sliding occurs between the graphene layers which subsequently equilibrate in an A-B-A arrangement [182] as the friction stops the sliding.

The water molecules are described using the classical SPC/E model. [184] In the graphene

sheet, the carbon-carbon valence forces are described using Morse, harmonic angle and torsion potentials. [150, 152, 153] A nonbonded carbon-carbon 12-6 Lennard-Jones potential with parameters $\epsilon_{CC} = 0.4396\,\text{kJ/mol}$ and $\sigma_{CC} = 0.3851\,\text{nm}$ to describe the van der Waals interaction between the carbons within different graphene layers. The water-carbon interaction is modelled by a Lennard-Jones potential with parameters obtained by Werder et al. [80] to recover the macroscopic contact angle of water on graphite of 86°. More details of the employed models and potentials can be found in Appendix A.

Momentum transfer from the solid to the liquid is known to affect slip length [62] thus in order to avoid the direct application of a heat bath to the fluid molecules, viscous Joule heat is subtracted from the system by coupling a Berendsen thermostat [156] to the carbon atoms with a weak coupling constant of 0.1 ps to a temperature of 300 K. We measured the water temperature in each system after steady state is reached to assure effective heat removal. Coulombic and van der Waals interactions are truncated at 1 nm. [60, 80, 150, 153] The leap-frog integration algorithm with a time step of 2 fs is used to integrate the equations of motion. Poiseuille like flow is generated by imposing a constant external field to all water molecules inside the channel. The direction of the external field is systematically changed to study flow in both AC and ZZ directions. Simulations are conducted for more than 60 ns extracting data after the first 5 ns.

4.3 Results

This study reports about water flow in slit graphene channels with heights of 2.0, 2.4 and 2.8 nm. We vary systematically the external field to impose accelerations from 5×10^{10} to 1.6×10^{12} m/s^2 in direction towards the ZZ and AC crystallographic orientations of the graphene walls, respectively. It should be noted that although the pressure gradients, correspondent to the studied external fields, have not been achieved experimentally, new and promissory techniques are being developed to achieve high pressure gradients at the nanoscale. [185] Flow velocity and density profiles across the channels are computed using the binning method. [60]

The velocity profiles are shown in Figure 4.3 and exhibit the expected plug-like flow, displaying high slip velocities. Due to the extremely low curvature of the velocity profiles and the uncertainty related to the thermal noise, slip velocity is estimated from the average flow velocity across the channel. For water flow in nanochannels with graphitic walls, a plug-like flow is expected as numerous studies have reported this behavior. [18, 19, 22, 53, 70, 118, 186] Nevertheless, the flow velocities as a function of channel height depicted in Figure 4.4 show that a parabolic flow profile can still be recovered as a greater signal to noise ratio is achieved by imposing higher external fields. Therefore, the parabolic shape of the profiles suggests that viscosity still has influence on the flow thus in graphene channels, the flow can be described using a modified Hagen-Poiseuille model. [29, 91] Moreover, as higher external fields are applied, the velocity profiles shown in Figure 4.3 reveal that higher velocities are computed for flow imposed along the AC direction which implies lower slip velocities for the corresponding cases with flow along ZZ direction.

Using the method reported by Ritos et al. [70] we compute the water flux and subsequently, from the corresponding flux values, the volumetric flow is calculated as shown in Figure 4.5. At higher imposed external fields, volumetric flow rates confirm that different flow velocities are achieved for AC and ZZ flow directions. Moreover, Figure 4.5 shows that the volumetric flow rate displays a linear response to the imposed external field up to a critical value. Indeed, as the critical value of the external field is reached, the flow rates become flow direction dependent

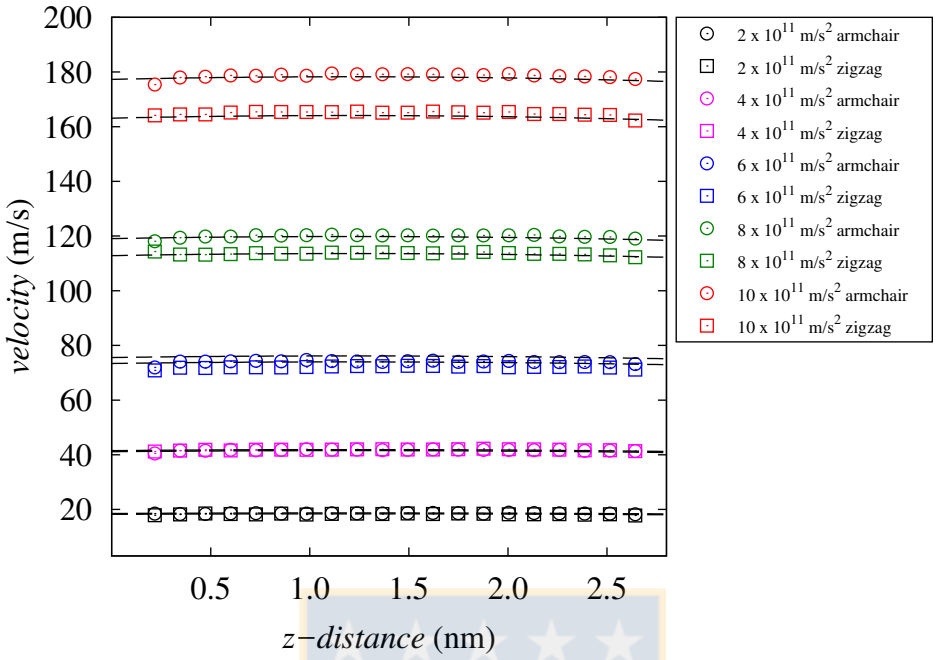

Figure 4.3: Water velocity profiles under different applied external fields for the 2.8 nm height graphene channel case. Black dashed lines represent the modified Hagen-Poiseuille model fit. Source: Own elaboration.

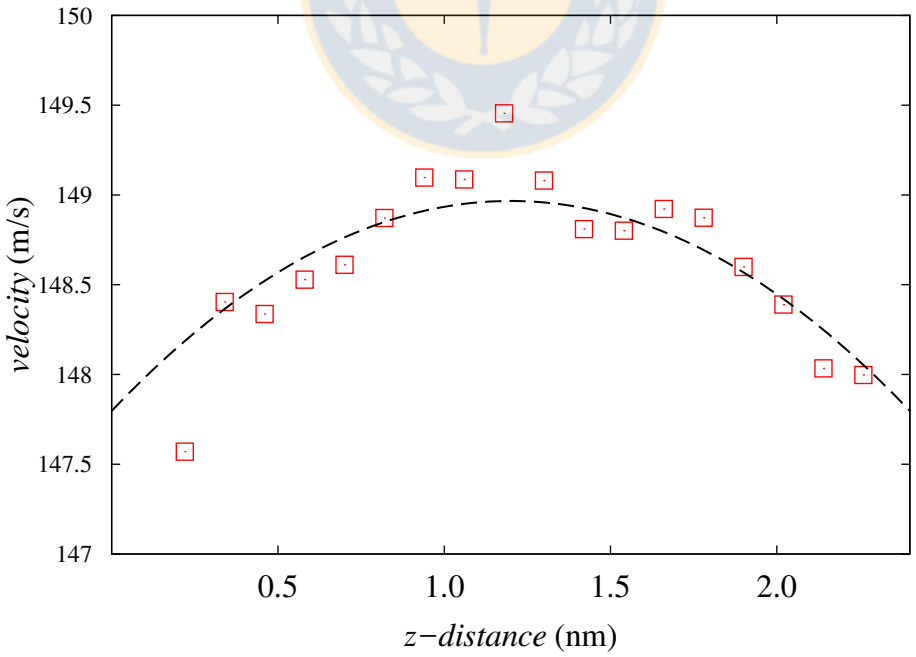

Figure 4.4: Water velocity profile for the 2.4 nm height graphene channel case with an applied external field of 1.2×10^{12} m/s^2 in the zigzag direction. Source: Own elaboration.

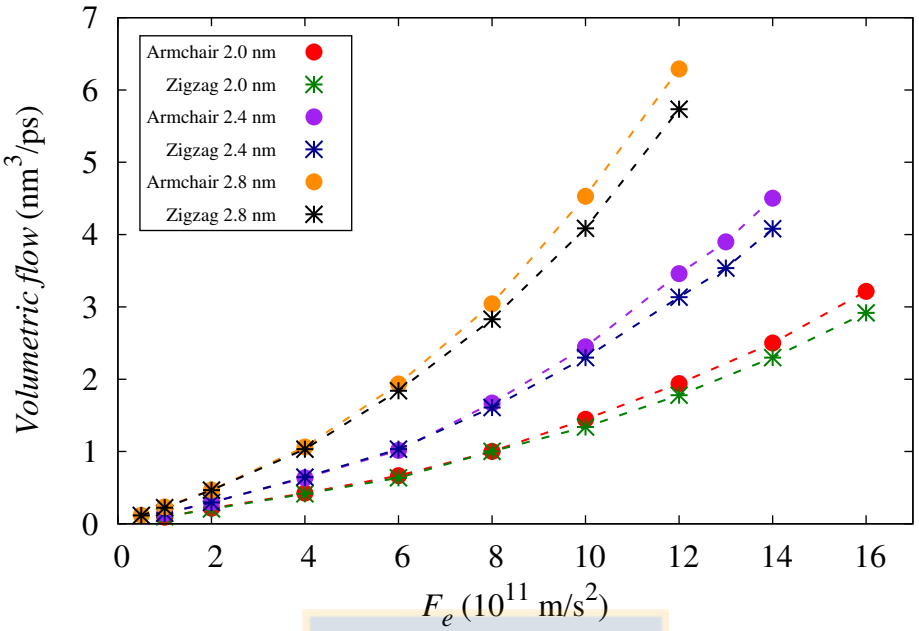

Figure 4.5: Volumetric flow as a function of the applied external field (F_e) for each studied graphene channel cases. Source: Own elaboration.

which indicates that slip velocity (v_s) is chirality dependent after a critical value of flow velocity.

In order to get insight in the relationship between flow rates and the particular flow direction, we refer to the concepts of enhancement (ϵ) and slip length (l_s), criteria widely used to compare flows with a significant slippage. [16,18,19,27,60,187,188] The ϵ corresponds to the ratio between the computed flow (Q) and the theoretical Poiseuille flow (Q_{HP}).

$$\epsilon = \frac{Q}{Q_{HP}} \tag{4.1}$$

Our theoretical flow rates were calculated by feeding the bulk viscosity for the SPC/E model [144] into the no slip Hagen-Poiseuille solution of the Navier Stokes equations, wherein the fluid velocity at the wall vicinity is assumed equal to zero.

$$\frac{Q_{HP}}{w} = \frac{1}{12\mu}\left[\frac{h^3 \Delta P}{L}\right] \tag{4.2}$$

where h corresponds to the channel height. Height is calculated as the average distance between the innermost graphene layers, subtracting the Van der Waals size of the carbon atoms (0.34 nm). ΔP is estimated as:

$$\Delta P = \rho F_e L \tag{4.3}$$

where F_e corresponds to acceleration of the applied external field, L is the channel length and ρ is the overall water density in the channel. w corresponds to the channel width.

Slip length calculations follow the P5 procedure reported by Kannam et al.. [19] This method requires no fit of the computed flow velocities to a theoretical velocity profile as flow in graphene

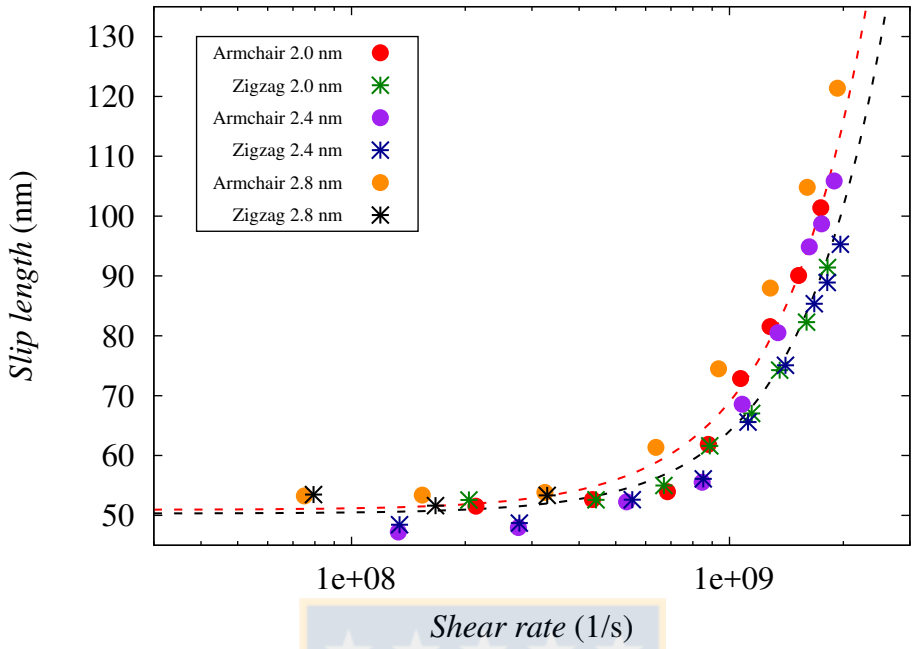

Figure 4.6: Slip length as a function of the shear rate for the studied graphene channel cases. For low shear rate a constant slip length of approximately 50 nm is observed up to a critical shear rate value, where divergence is observed. A difference in the slip length between armchair and zigzag is observed beyond this value. The dashed lines correspond to a power law fit to the AC (red) and ZZ (black) cases and serve as a visual aid. Source: Own elaboration.

channels displays very low curvature profiles and is very sensitive to thermal noise. Based on these procedures, the slip length is calculated from ϵ as:

$$l_s = \frac{h\,(\epsilon - 1)}{6} \tag{4.4}$$

In Figure 4.6 slip length as a function of shear rate $\left(\dot{\gamma} = \frac{v_s}{l_s}\right)$ is shown for all cases. A constant value of the slip length around 50 nm is computed for shear rate values lower than $6 \times 10^8\ \mathrm{s}^{-1}$. After, this critical value of the shear rate, the slip length diverges from a linear behavior. We note that divergence in the slip length values was first reported by Thompson and Troian. [16] In their work they investigate the shear rate effect on the slip length by conducting MD simulations of a simple Newtonian fluid under a Couette flow regime. While systematically increasing the wall velocity, they find a slip length dependence on the applied shear rate. They report no change in the bulk viscocity therefore the shear dependence is not related to a non-Newtonian behavior in the bulk zone of the fluid. Indeed, they propose that the value of shear rate at which nonlinear behavior of slip occurs is determined by the corrugation of the potential surface at the fluid-solid interface. This work has been a subject of controversy during the last two decades. Indeed, several studies have confirmed this behavior, [63, 89, 90, 189] whereas many others have reported no agreement with the slip divergence. [62, 187] Nevertheless, all these studies agree that the slip divergence depends on the rate of momentum transfer between the solid surface and the fluid. In Appendix B.2 we present the shear rate as a function of the shear stress, to demonstrate that the bulk fluid remains Newtonian.

Table 4.1: Slip length for a 2.8 nm height channel with an applied external field of 10×10^{11} m/s^2 in both directions for each case. Source: Own elaboration.

Case	Slip length (nm) Armchair	Zigzag
1 - carbon-carbon nonbonding interaction parameters from [150]	106.8	96.4
2 - carbon-carbon nonbonding interaction parameters from [190]	104.3	95.1
3 - carbon-carbon nonbonding interaction parameters from [191]	104.3	95.1
4 - carbon-carbon nonbonding interaction parameters from [150], water molecules and carbon atoms coupled to the thermostat	109.8	98.3
5 - Position of the carbon atoms fixed, water molecules coupled to the thermostat	80.3	74.2

In our simulations, to ensure a proper description of the graphene-water momentum transfer (with case 1 as reference case), we vary systematically the graphene interlayer distance by using the carbon-carbon intermolecular potentials parametrized by Saito et al. [190] (case 2) and by Girifalco et al. [191] (case 3). In both cases applying the thermostat only to the carbon atoms rather than to the fluid molecules. Moreover, to test, the Joule heat extraction, we conduct simulations with the thermostat coupled simultaneously to the water molecules and to the carbon atoms (case 4) and also with the thermostat connected to the water molecules while maintaining the carbon atoms rigid (case 5). Each case has the same number of water molecules confined in graphene channels with heights of 2.8 nm. An external field of 10^{12} m/s^2 was applied in both crystallographic directions. The results of these simulations are listed in table 4.1, we note that the flow properties exhibit good agreement for the cases with active carbon atoms. Nevertheless, in the case with rigid carbon, a considerable shorter slip length was computed, at least 20% lower than the ones computed in the cases with active carbon atoms as listed in table 4.1. Furthermore, for all cases, significant differences in the slip lengths are computed for the flow along the ZZ and AC crystallographic directions as listed in table 4.1. Further details on the momentum transfer and how it affects the temperature profile can be found in Appendix B.1.

Previous works have explored how slip occurs at the molecular level. [14, 16, 61, 63, 89, 90, 180, 189] In particular, Martini et al. [63] and Wang et al. [90] studying Couette and Poiseuille flow in nanochannels proposed a serie of molecular mechanisms describing the slip development. They find that slip is different depending on the magnitude of the shear stress and the capacity of the fluid molecules near the wall to overcome the potential energy corrugations projected by the wall atoms. It is, slip divergence occurs when the shear reaches a critical value. The results of Martini et al. and Wang et al. at high shear stress agree with the results of Thompson and Troian [16] of Couette flow of a Newtonian fluid. In the present work shear stress (τ) is calculated from the value of the external field (F_e), the number of water molecules (N), the molecular mass (m) and the surface area as $\tau = NmF_e/2A$. [118] Our results, shown in Figure 4.7, are in line with these studies, as after a critical value of τ, around 0.4 MPa, slip length appears to diverge, caused by nonlinearity of v_s with τ. Whereas, for values of τ below the critical shear, our results indicate a constant friction coefficient (λ), which is expected for a Newtonian flow with constant slip length, as $\lambda v_s = \mu \frac{dv}{dz}$ [192], therefore $\tau = -\lambda \times v_s$. Furthermore, when slip divergence is reached a significant difference arise between the flows computed in the armchair and the zigzag crystallographic directions as shown in Figures 4.7 and 4.8.

Chirality dependent water flow in CNTs has been previously reported. [20, 153, 193] Falk et

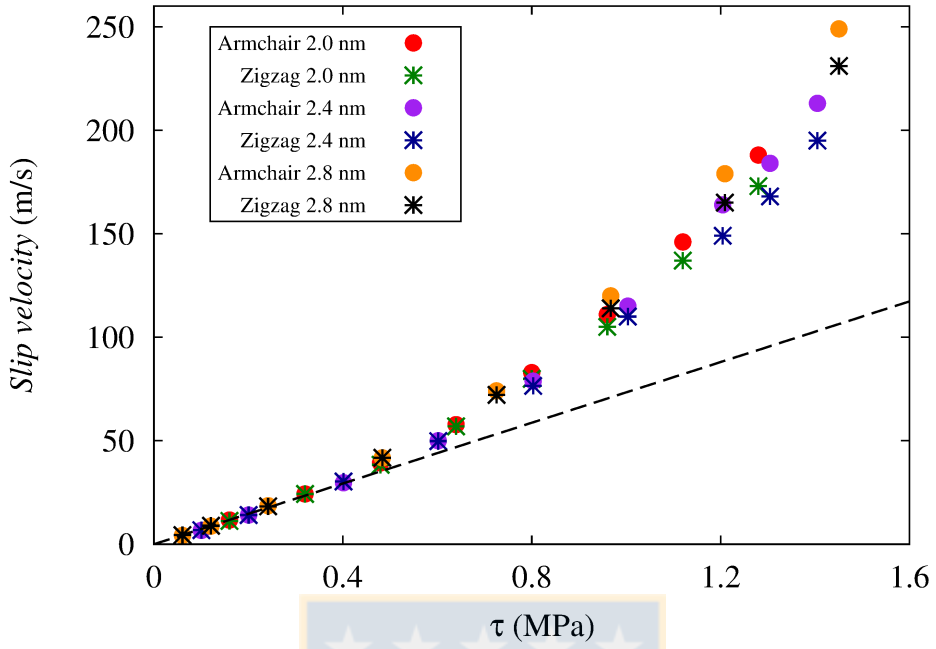

Figure 4.7: Slip velocity as a function of the shear stress for the studied graphene channel cases. Linear dependence between shear stress and slip velocity is found up to a divergence point. Source: Own elaboration.

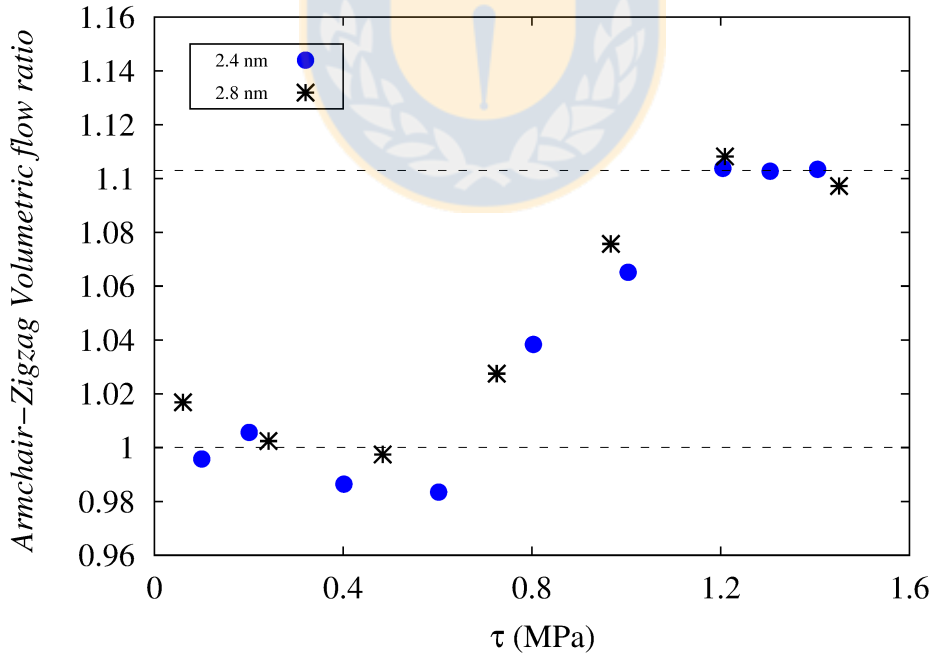

Figure 4.8: AC-ZZ flow ratio vs shear stress for the studied graphene channel cases. Three flow regimes are found; AC and ZZ equal friction coefficient (FC) (equal AC-ZZ flow), a transient regime, and a third regime on which the ratio of AC FC and ZZ FC converge to a constant value around 1.1. Source: Own elaboration.

al. [20] studied the relationship between the slip length estimated from the carbon-water friction coefficient, and the corrugation of the carbon surface energy for different CNT radii. They found that as the CNT radius decreases the energy corrugation felt by a water molecule becomes smoother and consequently the friction coefficient ($\lambda = -\tau/v_s$) decreases nonequally for the AC and ZZ CNTs below a critical radius of 3 nm. For flow in graphene channels at relatively low shear rates, Falk et al. [20] found the friction to be independent of the flow orientation.

In the present work, the slip velocity and the volumetric flow ratio as a function of shear stress depicted in Figures 4.7 and 4.8, exhibit an isotropic flow for shear stress below a critical value of 0.4 MPa in agreement with Falk et al.. [20] Moreover, it is noted that below this critical shear stress, v_s depends linearly to τ therefore the friction coeficient λ is constant for flow in both crystallographic directions. Nevertheless, in Figure 4.7 as the critical shear stress value is reached, the slope of the function v_s vs τ increases, which means that the friction coefficient λ start to decrease resulting in slip divergence.

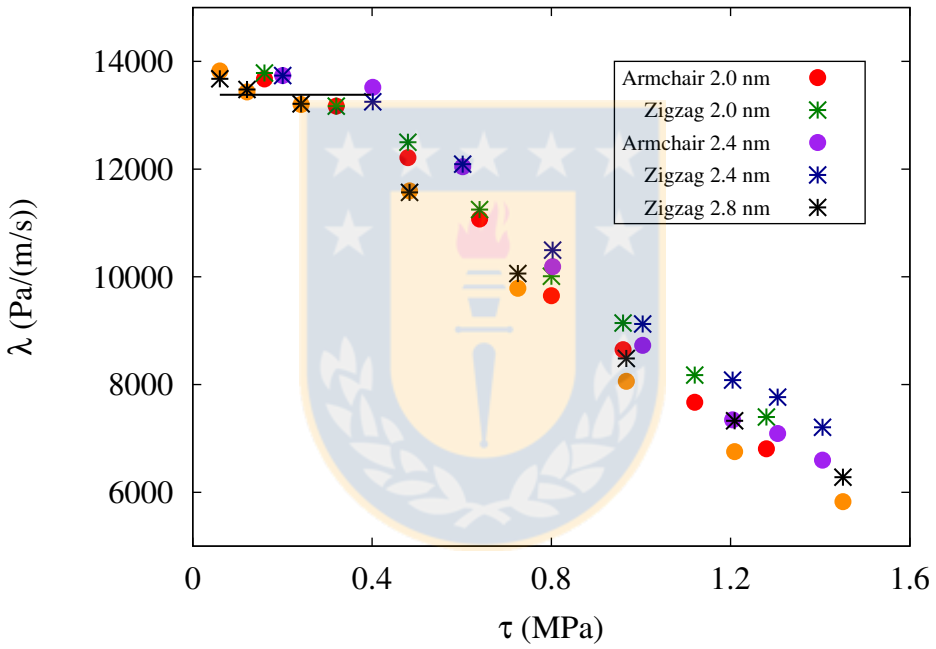

Figure 4.9: Friction coefficient as a function of shear stress for the studied graphene channel cases. The black line represents the mean λ for the non divergence zone. Source: Own elaboration.

In the present study, as the slip divergence occurs, anisotropic water flow is observed which means the flow becomes graphene chirality dependent as depicted in Figure 4.7. Indeed, as confirmed in Figure 4.9 a reduction in the friction coefficient λ leads to the observed chirality dependent flow. This behavior is consistent with the results found by Tocci et al. [14] for water flow on graphene and hexagonal boron nitride sheets. Performing first principle simulations, they found that although for the two sheets the interface presents a very similar structure, the friction coefficients are significantly different. Moreover, in a recent experimental study, Secchi et al. [21] found similar results for flow in CNTs and boron nitride nanotubes that are crystallographically similar. They attribute the differences observed to subtle atomic-scale details of the solid-liquid interface. Furthermore, we believe that anisotropic transport of water in graphene channels at high shear stress is the result of a lower energy dissipation at the wall-fluid surface which originate

from a reduction in the momentum transfer at higher flow velocities. It has been reported that the momentum transfer decreases after slip divergence occurs resulting in a weak friction flow dominated by the relative surface energy corrugation. [15, 16] Specifically, the amount of slip increases with decreasing surface energy corrugation.

In order to confirm the anisotropic fluid flow, we compute the AC/ZZ flow ratio as a function of τ as shown in Figure 4.8 where a ratio equal to 1 is computed for the shear stress below the critical value. Subsequently, as slip divergence occurs, Figure 4.8 shows the AC/ZZ flow ratio start to increase up to a constant value around 1.1, showing the existence of a transition regime wherein momentum transfer is still significant to determine the water flow rates. We believe that as the effect of the interfacial momentum transfer on the flow diminishes, the slip velocity becomes directly related to the surface energy corrugation felt by the water molecules. It should be noted that the surface energy corrugation on the graphene walls is inherently dependent on the particular ZZ or AC flow orientation. [193]

4.4 Conclusions

NEMD simulations were carried out to study flow anisotropy in pressure driven water transport in graphene channels. For low shear rates, a constant slip length of approximately 50 nm is found up to a critical value of the shear stress of 0.4 MPa below which flow is not chirality dependent. As slip divergence occurs, the flow start to be chirality dependent which means the slip velocity vary up to 10% with the particular flow orientation i.e., armchair or the zigzag crystallographic directions. We relate the anisotropic flow within the slip divergence zone to a reduction in the effect of the momentum transfer in the wall-fluid interface resulting in an enhanced effect of the surface energy corrugation felt by the interfacial water molecules.

Chapter 5

Monolayer graphene-based coating to induce water flow enhancement in silica nanochannels

Parts of this chapter have been submitted as a manuscript for publication in Journal of Molecular Liquids: Enrique Wagemann, Diego Becerra, Jens H. Walther, and Harvey A. Zambrano. "Monolayer graphene-based coating to induce water flow enhancement in silica nanochannels".

5.1 Introduction

Last decade fast-growing advances in fabrication techniques have led to the development of functional microfluidic devices integrated by channels with submicrometer dimensions. [45, 194–197] Further miniaturization of these microfluidic systems open the way to achieve fluid transport performance in artificial devices close to that of ultra-high efficient flow through bio-membranes. [55,198] Indeed, the length scale reduction inherent to nanotechnology has led to the emergence of a new technological field, i.e., nanofluidics, the study of the transport of fluids confined in conduits where at least one dimension is just a few nanometers. [45,50,64] Therefore, attaining precise fluid transport in nanochannels is, nowadays, key for a wide range of technological applications such as water desalination [199], chemical separation [195], DNA sequencing [200], drug delivery [201] and Lab-On-a-Chip units. [196]

Despite tremendous effort has been devoted to investigate flows in nanopores [23, 25, 65, 117, 202, 203], a comprehensive understanding of fluid dynamics in nanoconfined geometries is still lacking to design functional and high efficient fluid nanodevices. In fact, transport of nanoconfined fluids exhibits a behavior that departs significantly from that occurring in its micro and macro-scalar counterparts owing to new physical phenomena associated to the extreme confinement, [55, 204, 205] augmented interfacial effects, [14, 206], specific thermal properties [66] and significant steric effects. [207] In particular, the augmented effect of the interfacial fluid properties on the flow through nanochannels makes possible exploitation of surface modifications to alter overall fluid dynamics in nanoconfined fluids. [14, 55, 154, 202, 208, 209]

In general, for fluid transport inside channels the hydraulic resistance or viscous drag is directly related to amount of energy required to pump the fluid. In this context, previous investigations have found that in nanoscale hydrophilic conduits extremely low flow rates are associated to very large hydraulic resistances. [203,204] Nevertheless, recent studies have reported

ultra fast motion of nanoconfined water in contact with hydrophobic walls, i.e., higher than expected water flow rates attained in carbon nanotubes (CNT) and graphene (GE) channels. [18, 21–23, 26, 27, 186] In fact, experiments and computational studies have provided evidence that these measured high flow rates strongly depend on an ultra-low friction at the carbon-water interface that translates into very large slip lengths. [18–20, 23, 117, 186] Indeed, slip lengths that exceed by several times the height of the channel have been reported, with values ranging from nanometers to micrometers. [18, 19, 21, 27] Moreover, this low friction of water in contact with CNT and GE interfaces has been also associated to their atomically smooth graphitic walls and to their generally accepted weak interaction with water. [13, 18, 22, 23, 117, 210] Consequently, GE layers and CNTs are interesting candidates to be used as building blocks in future integrated nanofluidic systems or even as coatings to reduce hydrodynamic drag in hydrophilic nanopores.

In a recent work, Xie et al. [202] reported experimental evidence of fast water transport inside hybrid silica-graphene nanochannels. For water in contact with a graphene surface, they report a slip length of 16 nm with a substantial variation up to 200 nm. This high variability was attributed to induced surface charges in the graphene as a result of the interaction with the underlying silica substrate and to the presence of carboxilic functional groups on the graphene surface due to oxidation. The authors further explore this hypothesis by employing Molecular Dynamics (MD) simulations. Using this technique a slip length on pristine GE of ca. 90 nm is computed, which decreases to 75.2 nm when GE is supported on a silica substrate. They also observe, that an increasing concentration of -COOH groups on the graphene surface results in a decrease in the slip length. For instance, a slip length of 3.3 nm is reported for a concentration of 0.5% -COOH. Despite claiming quantitative agreement with experimental measurements, the simulation results could be significantly influenced by the fact that the viscous heat was extracted by coupling a thermostat directly to the fluid molecules, which is known to affect the transfer of momentum at the nanochannel walls altering the transport properties. [19,211–213] Furthermore, maintaining frozen the positions of wall atoms can result in unphysical behavior of the interfacial water and might artificially alter slippage on the solid surface in the channel. [56, 58, 214] These factors are considered in the present study and special care is taken upon them.

In a recent and accurate experimental study, Li et al. [33] found that ultra-clean supported GE is more hydrophilic than previously assumed, concluding that reported values of water wettability of GE surfaces is a consequence of unintentional hydrocarbon contamination from ambient air. Nevertheless, in foreseeable nanofluidic applications typically, graphene-based devices would be expected to operate in an ambient atmosphere, and therefore exposed to permanent airborne contamination. Furthermore, recent investigations examining the degree to which the underneath substrate affect the water contact angle (WCA) on GE sheets [119–121, 215] have brought water wettability of GE to intense debate. In fact, these studies have reported either full transparency to wettability [35], translucency [35–37, 40, 215] or even total opacity [42, 43] for water in contact with GE supported on different type of substrates. Therefore, showing that the wetting of water on supported GE depends significantly on the specific substrate whereon GE is supported. In particular, for monolayer GE supported on a silica substrate, Rafiee et al. [35] found wetting translucency, reporting a WCA of 49°.

Giant hydraulic resistance is associated to water fluidity in hydrophilic nanochannels therefore drag reduction is a key technological problem related to the development of nanoscale fluidic devices. [51, 203] Graphitic materials like GE sheets displaying large water slippage are excellent candidates to be implemented as wall coating in nanopores to reduce the amount of energy required to transport water in nanoconfinement. In the present study, we employ MD simulations to investigate whether the use of a GE monolayer as wall coating in a hydrophilic silica channel

results in a significant water flow enhancement. In order to determine the degree of transparency to wettability present in our system, we conduct equilibrium MD simulations to measure the WCA on a silica substrate with and without GE coating. Subsequently, we conduct Nonequilibrium MD (NEMD) simulations to estimate the effect of GE coating on water flow rates in a silica nanoslit channel. Our results provide quantitative evidence that GE coating in a silica nanochannel results in substantial drag reduction in water transport which could be an enabling technology for the design and fabrication of efficient integrated nanofluidic devices.

5.2 Computational methods

The simulations in this work were carried out using the parallel MD package FASTTUBE, which has been used extensively to study liquids confined inside CNTs, GE layers and silica channels. [23, 24, 65, 68, 80, 151, 153, 154] The water molecules are modeled using the rigid SPC/E water. [184] The silica atoms are described using the TTAMm potential developed by Guissani and Guillot [216] which is a modification of the classical TTAM potential developed by Tsuneyuki et al.. [217] In this study, we employ the original set of atomic partial charges in the TTAM model which correspond to values of: $q_{Si} = +2.4\,e$ and $q_{O_{SiO_2}} = -1.2\,e$. The van der Waals interactions between silica atoms and water molecules are described using a Buckingham potential with parameters taken from our previous work. [218] The GE-water interactions are described by a Lennard-Jones potential parametrized by Werder et al. [80] to reproduce a macroscopic water contact angle on graphite of 86°. The GE-silica interactions are described employing a Lennard-Jones potential with parameters from Zhang and Li [219] which reproduce the proper substrate-regulated morphology of GE. The carbon-carbon valence forces within the GE sheet are described using Morse, harmonic angle and torsion potentials. [150, 153] More details of the employed models and potential are presented in Appendix A. The leap-frog scheme is used to integrate the equations of motion with a time step of 2 fs. In all simulations, an orthorhombic box is used with periodic boundary conditions in the x and y directions, while free space conditions are applied in the z direction. The x and y dimensions are chosen to minimize artificial strain [118] within the GE sheet due to the periodic boundary conditions. Temperature control is achieved by employing a Berendsen thermostat [156] with a weak coupling constant of 0.1 ps. [23] To account for long range electrostatic interactions, we employ a Smooth Particle Mesh Ewald (SPME) algorithm [161] with a real-space cutoff of 1.0 nm that includes corrections for a slab geometry. [220]

5.3 Results and discussion

5.3.1 Water contact angle

In order to validate the atomistic models and the force fields employed in our simulations, the WCA is measured on both GE coated and bare silica substrates. To this end, MD simulations of periodic cylindrical droplets of water are conducted to reproduce directly the macroscopic WCA, avoiding the line tension effects associated to spherical droplets. [35, 40] A snapshot of the system is presented in Figure 5.1. First, a cristobalite unit cell is replicated to build a crystalline slab. Subsequently, the slab amorphization is achieved by following the annealing procedure reported by Zambrano et al.. [68, 218] More details on the slab amorphization can be found in Appendix C.1. The substrate is then coated by releasing a GE sheet near the silica surface. The GE sheet is periodic in x and y directions. Afterward, the system is equilibrated by connecting

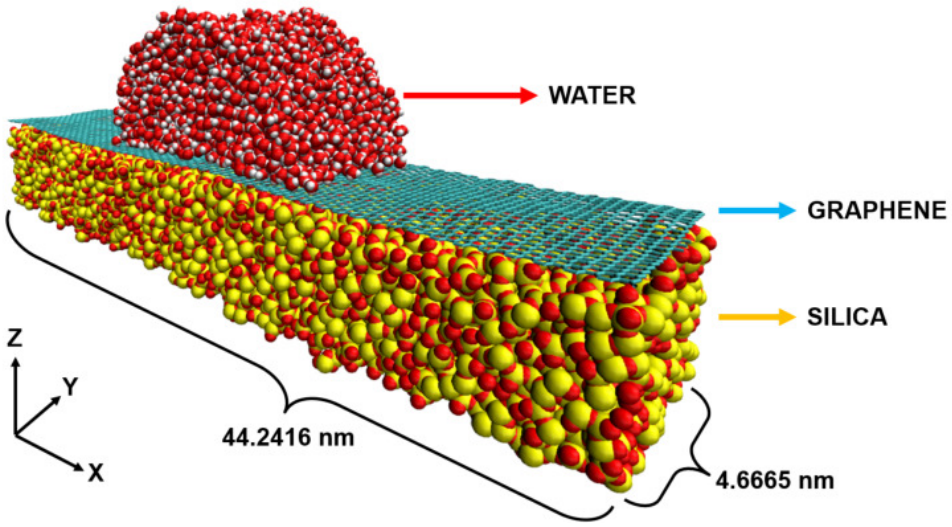

Figure 5.1: Snapshot of a WCA simulation. A cylindrical periodical droplet on top of a graphene coated slab is simulated to avoid effect of the line tension on the measured angle. Source: Own elaboration.

the carbon atoms to a Berendsen thermostat [156] at 300 K while silica atoms are maintained fixed. After the equilibrium state is reached, the GE-silica contact separation is 0.49 nm and the average C-C bond distance is 0.1423 nm, in line with values reported in previous studies. [118] For more details on how the contact separation is estimated, we refer the reader to Appendix C.3. Moreover, we measured the Solvent Accesible Surface Area (SASA) of the surfaces (presented in Appendix C.2). Next, a periodic water slab consisting of 3600 water molecules is released in the NVT ensemble at 300 K during 0.5 ns and when equilibrium state is reached, the water molecules are placed on the substrate surface to create a sessile cylindrical droplet. Then, while in contact with the surface, water molecules are connected to a Berendsen thermostat during another 0.5 ns. Afterward, the thermostat is disconnected and the simulation is conducted for another 0.5 ns in the NVE ensemble. Data are then collected every 0.1 ps during 1 ns of simulation. The density profiles are computed by a binning sampling method (more details in Appenxi C.7). The WCA is evaluated by fitting a circle to the 650 kg/m^3 isochore [151], as shown on Figure 5.2. The near wall region is excluded from the fit. More details of the methodology employed to measure the WCA are presented in Appendix C.4

The WCA measured for the droplet on the silica substrate coated with the GE sheet is 49°, in agreement with the WCA reported by Rafiee et al.. [35] Furthermore, complete wetting is achieved for water on the bare silica substrate. In order to quantify the strength of the solid-liquid interaction, the water binding energy per contact-surface area is computed. We measure values of 135.83 mJ/m^2 and 639.9 mJ/m^2 for the cases with coated and uncoated substrates, respectively. Moreover, we notice that when comparing the measured WCA for the cases with coated and uncoated silica, the observed wettability is in line with the GE translucency to wettability reported by Shih et al. [36] and Rafiee et al. [35] wherein the WCAs were measured on GE layers supported on fused silica substrates.

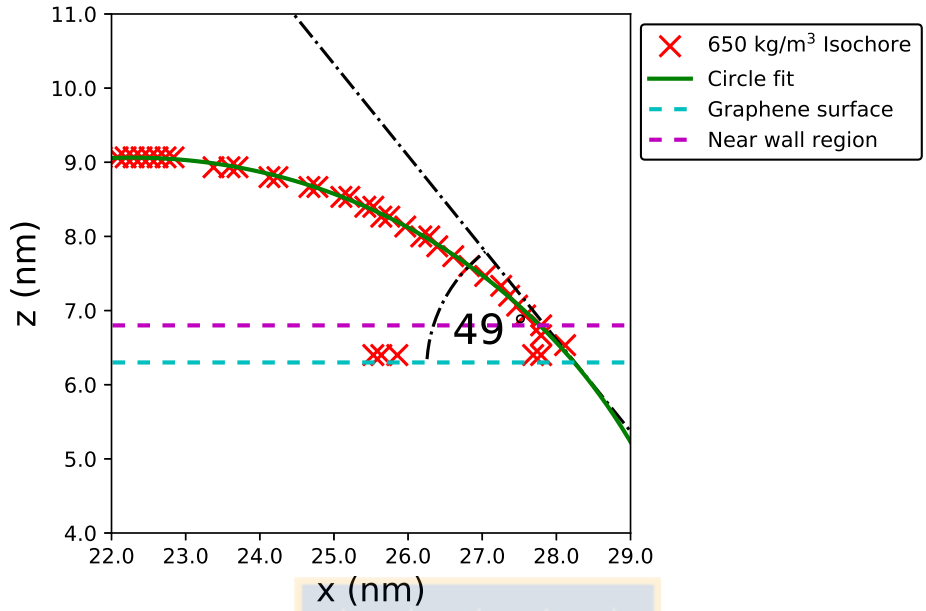

Figure 5.2: Water contact angle in the graphene coated slabs is measured by a circular fitting to the interface. The near wall region is excluded from the fit. Source: Own elaboration.

5.4 Water flow through nanoslit channels

To study flow enhancement induced by GE coating in hydrophilic channels, Poiseuille like flow of water is simulated in a silica nanoslit with and without monolayer GE coating the channel walls. The nanoslit consists of two parallel slabs of amorphous silica, representing the channel walls. A single sheet of GE monolayer is placed on the inner surface of each silica wall. A snapshot of the system is shown in Figure 5.3, where h corresponds to the channel height and is defined as the average distance along the z direction between the two GE sheets. Periodic boundary conditions are imposed along the x and y directions. In the present work, three channel heights are studied; 2.4, 3.4 and 4.4 nm. An internal pressure of 1 bar is attained by employing one of the walls as a piston to impose the target pressure, while the other wall remains immobilized during the channel pressurization. Furhter details of the methodology employed to attain an internal pressure of 1 bar are presented in Appendix C.5. The number of water molecules per system are: 3435 for the channel with a height of 2.4 nm, 5156 for the 3.4 nm channel and 6802 for the 4.4 nm channel. The water confined in the channel is equilibrated for 2 ns and density profiles are extracted using the binning method. The water density profiles are shown in Figure 5.4, displaying bulk and interfacial densities in good agreement with values reported in previous works. [37, 41, 221] Furthermore, the computed density profiles display an water layering in the interface with thickness of ca. 0.85 nm. As depicted in Figure 5.4, the layering thickness is the same for all the cases studied here, hence it does not depend on the particular channel height. Nevertheless, as confinement increases, the ratio between layering thickness and channel height increases. Therefore, it can be inferred that size reduction leads to a scenario wherein interfacial hydrodynamics becomes dominant [28].

After proper water confinement is verified, fluid flow is generated by imposing a constant

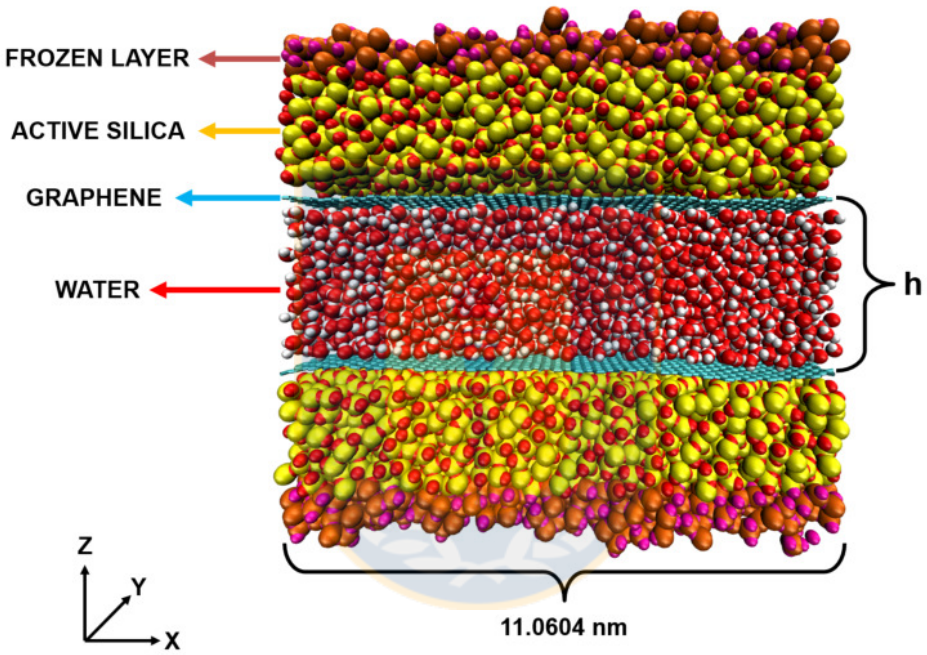

Figure 5.3: Snapshot of the studied graphene coated silica nano-channel system. Water is confined between two parallel amorphous silica slabs. In each slab the internal surface is coated with a graphene sheet. Source: Own elaboration.

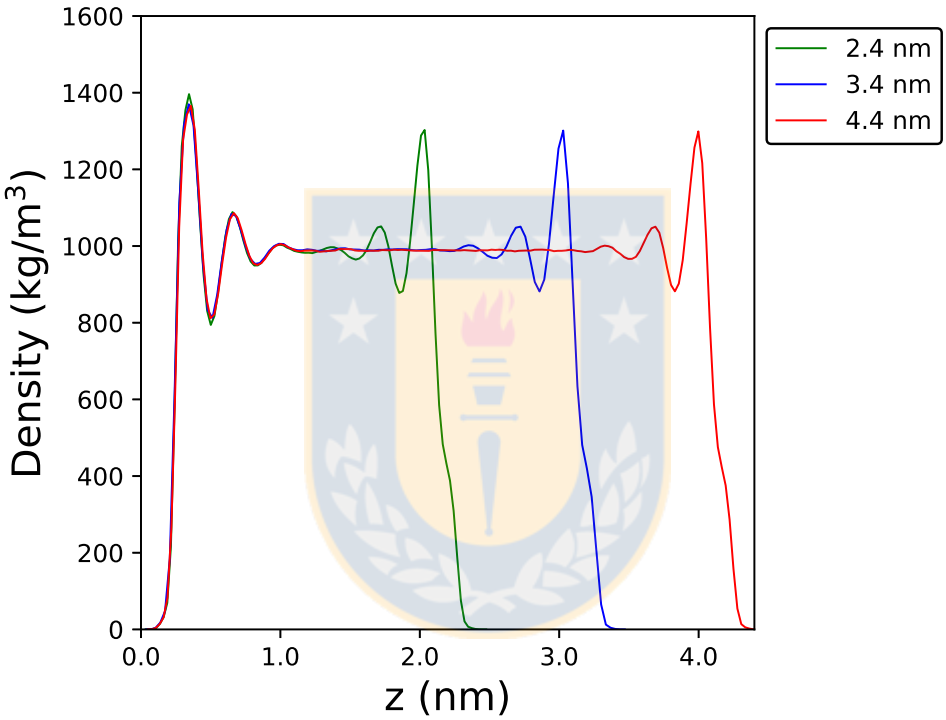

Figure 5.4: Density profiles for the graphene coated silica nano-channels, of different channel heights. Source: Own elaboration.

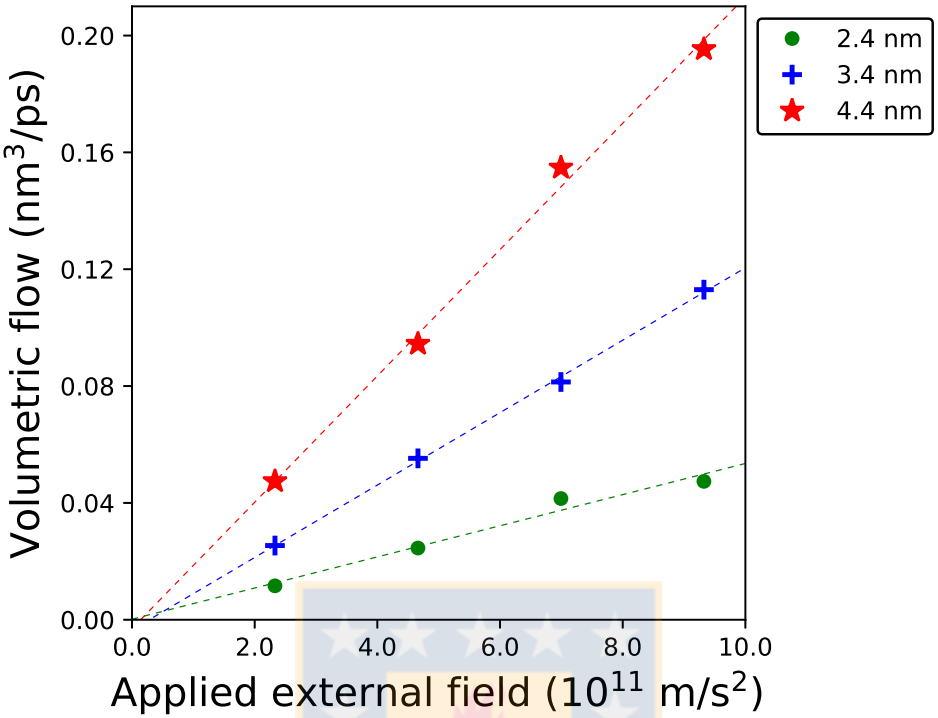

Figure 5.5: Volumetric flow rates measured for the graphene coated silica nano-channels, of different channel heights. Source: Own elaboration.

external field to all water molecules confined inside the channel. In this study, constant external field values ranging from 2.331×10^{11} to 9.324×10^{11} m/s^2 are imposed inside the channels. The employed external fields correspond to pressure gradients ranging from 2.26 bar/nm to 9.04 bar/nm. As shown in shown in Figure 5.3, the removal of the viscous heating is achieved by extracting heat through the silica walls. To this end, the position of the silicon and oxygen atoms within the outermost region of 0.4 nm width, measured from the external surface of each channel wall, is maintained fixed. Whereas silicon and oxygen atoms within the innermost region are maintained active and coupled to the Berendsen thermostat at 300 K. Note that the GE sheets are maintained flexible and not coupled to the thermostat during the simulations. Indeed, we measured the water temperature in the channel after the steady state is reached to ensure effective heat removal through the walls. An example of the measured temperature profiles is presented Figure C.2 of Appendix C.6. The simulations take a couple hundreds of picoseconds to achieve steady state, which is ensured by checking that the velocity of the water's center of mass remains constant over time. Each flow simulation is conducted for at least 30 ns to extract data every 10 ps.

The volumetric flow rates (Q) presented in Figure 5.5 are computed by following the methodology reported in our previous work [23]. Volumetric flow is calculated from the mass flow. The mass flow was measured by computing and averaging the number of molecules crossing 20 equidistant fixed planes in the streaming direction per unit of time. The mass flow is then divided by the overall density of the fluid in the channel to obtain the volumetric flow. The volumetric flow rates are found to depend linearly with the magnitude of the applied external field. Flow enhancement

Table 5.1: Calculated hydrodynamic properties of the water flow inside the graphene coated silica nano-channels. h denotes the channel height, ε the flow enhancement, l_s the slip length, μ_{ef} the effective viscosity, h^* the bare channel height and ε^* the effective flow enhancement. Source: Own elaboration.

h (nm)	ε	l_s (nm)	μ_{ef} (mPa·s)	h^* (nm)	ε^*
2.4	11.3 ± 0.5	3.09 ± 0.26	0.654 ± 0.05	3.0	3.72 ± 0.15
3.4	7.8 ± 0.2	2.99 ± 0.32	0.662 ± 0.08	4.0	3.49 ± 0.07
4.4	6.0 ± 0.1	2.93 ± 0.09	0.658 ± 0.02	5.0	3.21 ± 0.07

(ε) values presented in Table 5.1 are computed as the ratio between measured water flow rates and the corresponding theoretical no-slip Poiseuille flow rates (Q_{HP}). The volumetric flow rates for Poiseuille like flow with no-slip boundary condition are calculated by following equation 5.1, where ρ corresponds to the overall fluid density in the channel, g is the applied external field and μ_∞ is the viscosity of SPC/E water in bulk (0.729 mPa·s) [144]. The channel height is assumed as the average distance between the two parallel GE sheets, subtracting the van der Waals size of the carbon atoms (0.34 nm) [19, 23].

$$Q_{HP} = \frac{h^3 w \Delta P}{12 \mu_\infty L} = \frac{h^3 w \rho g}{12 \mu_\infty} \tag{5.1}$$

As listed in Table 5.1, increasing ε values are observed for channels with decreasing heights, i.e., wherein a higher ratio of surface to confined fluid volume is present. Therefore, our results confirm that GE coatings have a stronger effect on the flow of water inside channels with higher confinement. In nanoconfined Poiseuille flow with finite slip, flow enhancement is directly related to a reduction in the viscous drag. [117, 204] Therefore, the computed ε with values between 6.0 and 11.3 indicate that implementation of monolayer GE coatings in silica nanochannels results in a mitigation of the viscous resistance and thus in a significant reduction in the energy consumption for water pumping. Moreover, ε values around 10 for water flow in a GE coated silica channel imply that similar flow rates can be attained imposing a pressure gradient one order of magnitude lower than expected for a hydrophilic pristine channel.

Figure 5.6, shows velocity profiles for all the cases studied here. The velocity profiles exhibit a parabolic shape with a significant wall slippage, i.e., non-zero flow velocities are computed at the water-wall interface, as found in previous studies of water flow nanoconfined between graphitic. [23, 28, 38, 117] Moreover, we compute the slip length (l_s) for each of channel studied here, by imposing a parabolic fit to the corresponding velocity profiles. These values are listed on Table 5.1. A constant slip length of ca. 3.0 nm is observed for all the cases, which indicates that l_s is not size dependent. It should be noted, that the computed l_s cannot explain the observed flow enhancement if the classical relation between ε and l_s described by equation 5.2 is followed, as a l_s, if at least, 20% higher would be required.

$$\varepsilon = 1 + 6\frac{l_s}{h} \tag{5.2}$$

This scenario has been already assessed in previous studies [28, 117]. In particular Thomas and McGaughey [28] suggested a correction to equation 5.2 due to a decrease in the effective viscosity (μ_{ef}) of the fluid, when compared to μ_∞. They also pointed out that the decrease in μ_{ef} is a result of an increasing effect of the interfacial layering over the fluid, due to higher confinement. By imposing a parabolic fit to our obtained velocity profiles and based on the

Newton's law of viscosity, we estimated μ_{ef} for each channel studied here:

$$\tau = \mu_{ef} \frac{du_y}{dz} \tag{5.3}$$

where $\frac{du_y}{dz}$ is calculated from the parabolic fit to the velocity profile. The values presented on Table 5.1 show a constant μ_{ef}, with values below μ_{∞}, confirming their hypothesis.

In nanoconfined geometries, water is known to slip on both hydrophilic and hydrophobic surfaces. [88, 170, 222] Hence, flow enhancement computed by a direct comparison between the measured flow rate against theoretical no slip Poiseuille flow is not a proper criterion to estimate the real drag reduction in a nanochannel. Moreover, for nanofluidic applications, it is key to understand in a realistic scenario the drag reduction capabilities of GE coatings. Hence, it should be noticed that drag reduction achieved by coating the nanochannel walls is not exempt of cost in terms of changes in the channel geometry. In fact, the presence of the graphene sheet on the channel walls may decrease significantly the cross section of the nanochannel, an effect that can increase significantly the hydrodynamic resistance. [117, 183] Therefore, reducing the flow-enhancing capabilities of GE wall coatings in a realistic scenario. In order to take these factors into account, we compute flow rates of water confined inside nanoslit silica channels with uncoated walls. The bare slit silica channels are built by removing the GE monolayer coating, therefore the bare silica slits have larger cross sections as compared to the corresponding coated channels. An internal pressure of 1 bar is attained by following the protocols already described to fill the channel with water. Notice that the number of water molecules confined in each bare silica channel is higher than in the corresponding case with coated channels. The resulting channel heights, defined as the average distance between the inner surfaces of the silica slabs are: 3.0, 4.0 and 5.0 nm. The applied external field in these three cases corresponds to a value of 9.324×10^{11} m/s^2 which reproduces a pressure equivalent to the higher field applied in the cases with coated channels. Viscous heat is removed by following the protocols already mentioned and the fluid temperature is measured to ensure proper heat extraction.

The velocity and density profiles computed for the studied uncoated channels are presented in Figure 5.7. The velocity profile displays a parabolic shape with zero velocity at the water-solid interface therefore indicating that the non-slip boundary condition is a good assumption for flow inside the uncoated silica nanochannels. Moreover, from our results we compute an efective viscosity of $\mu_{ef} = 0.72 \pm 0.02$ mPa·s. The water density profile displays bulk behavior across the entire cross section of the channel, contrasting with the significant water depletion layer observed in the density profile across the corresponding GE coated channels. To quantify the flow transport efficiency, we compute the "effective" flow enhancement (ε^*) as the ratio between the flow computed in the coated channels (Q_{coated}) and the flow computed in the bare silica channels (Q_{coated}).

$$\varepsilon^* = \frac{Q_{coated}}{Q_{uncoated}} \tag{5.4}$$

Note that this comparison is technologically interesting, as the bare silica channels would represent nanochannels with pristine walls on which the GE coating would be subsequently applied. In Table 5.1 are listed the computed ε^* and the corresponding bare channel height for each case. It can be inferred from data in Table 5.1 that as the channel height increases, a decrease in ε^* is observed. This behavior is similar to the one observed for ε. Furthermore ε^* with values greater than 3.2 were computed which means that implementation of GE monolayer coating in silica nanoslit channels results in a significant decrease of the required energy to pump

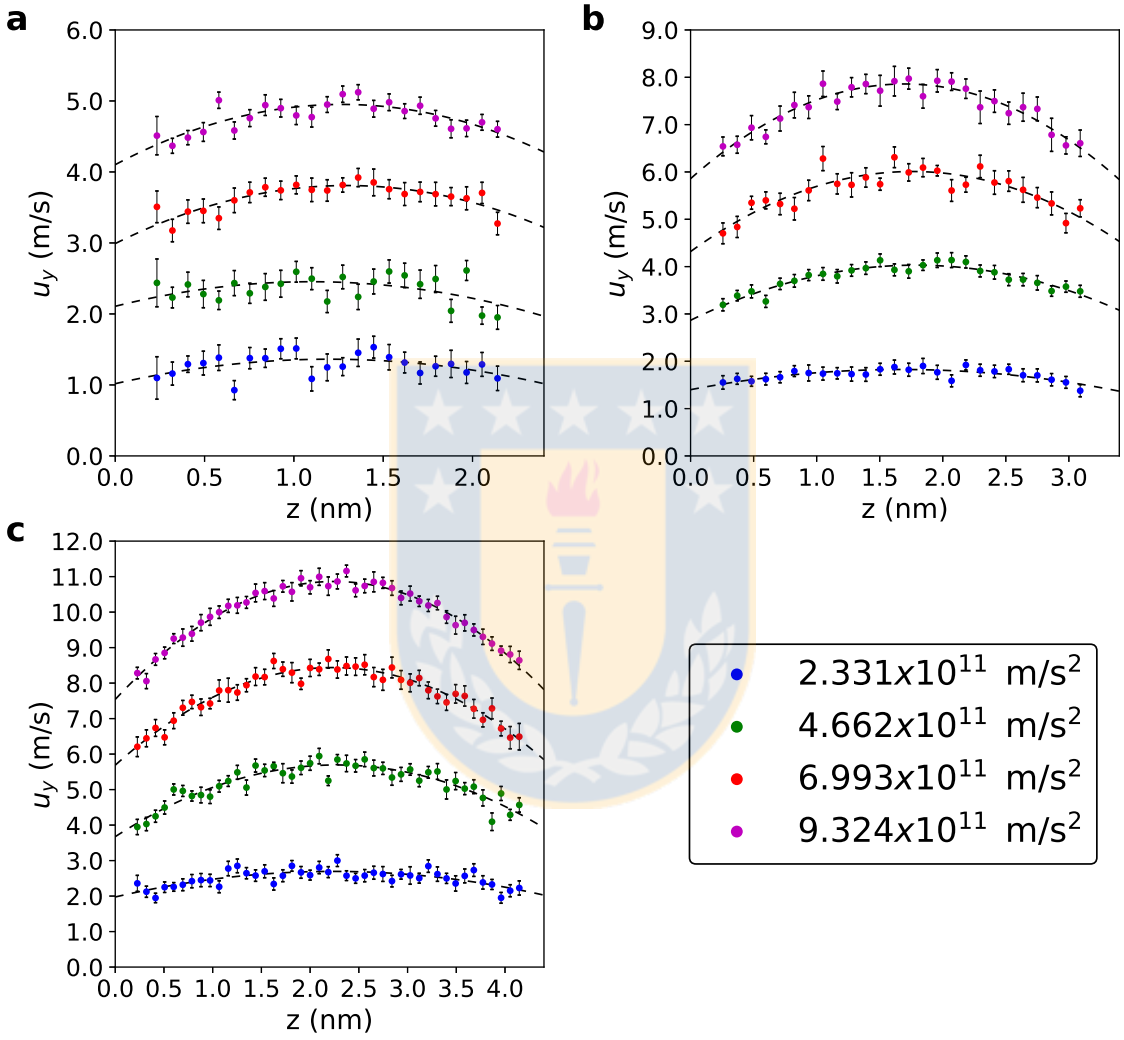

Figure 5.6: Water velocity profiles for different applied external fields in the graphene coated silica nano-channels with heights of A) 2.2 nm, B) 3.3 nm and C) 4.4 nm. The black dashed line depicts a parabolic fit to the measured velocity distribution across the channel. Source: Own elaboration.

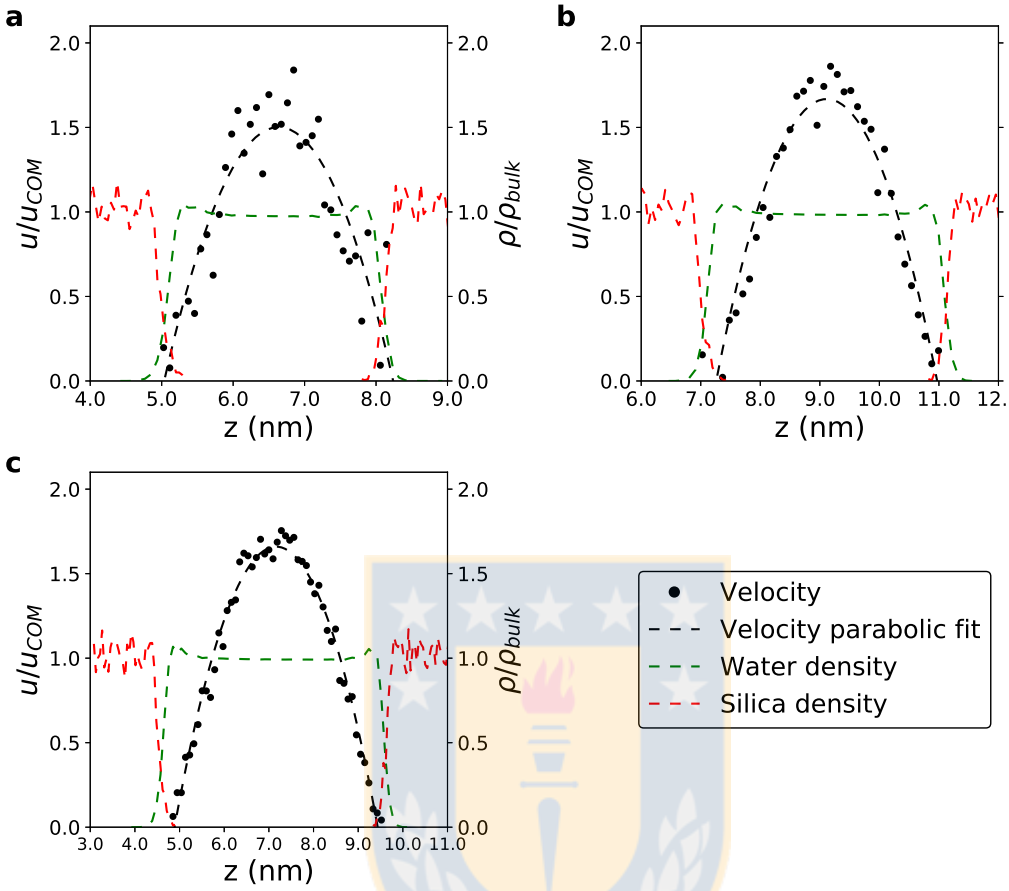

Figure 5.7: Normalized velocity and density profiles for water flow inside the uncoated silica nano-channels with heights of A) 3.0 nm B) 4.0 nm and C) 5.0 nm. Source: Own elaboration.

water through hydrophilic nanoconduits. Moreover, based in these results, we estimate ε^* at larger channel heights, as presented in Figure 5.8. The available channel height for the coated channel is estimated as the distance between graphene layers, subtracting the van der Waals size of the carbon atoms (0.34 nm). The volumetric flow for the coated channels is estimated by assuming a l_s of 3.0 nm and an effective viscosity of 0.66 mPa·s. The available channel height for the uncoated cases is estimated as the distance between graphene layers in the coated channels, adding 0.6 nm. The volumetric flow in the uncoated cases is estimated by assuming the no-slip condition and an effective viscosity of 0.729 mPa·s. We observe that ε^* quickly decreases with the coated channel height, asymptotically reaching the unity at large heights. This result suggests that the use of graphene as coatings induces an important flow enhancement only for channels with small heights.

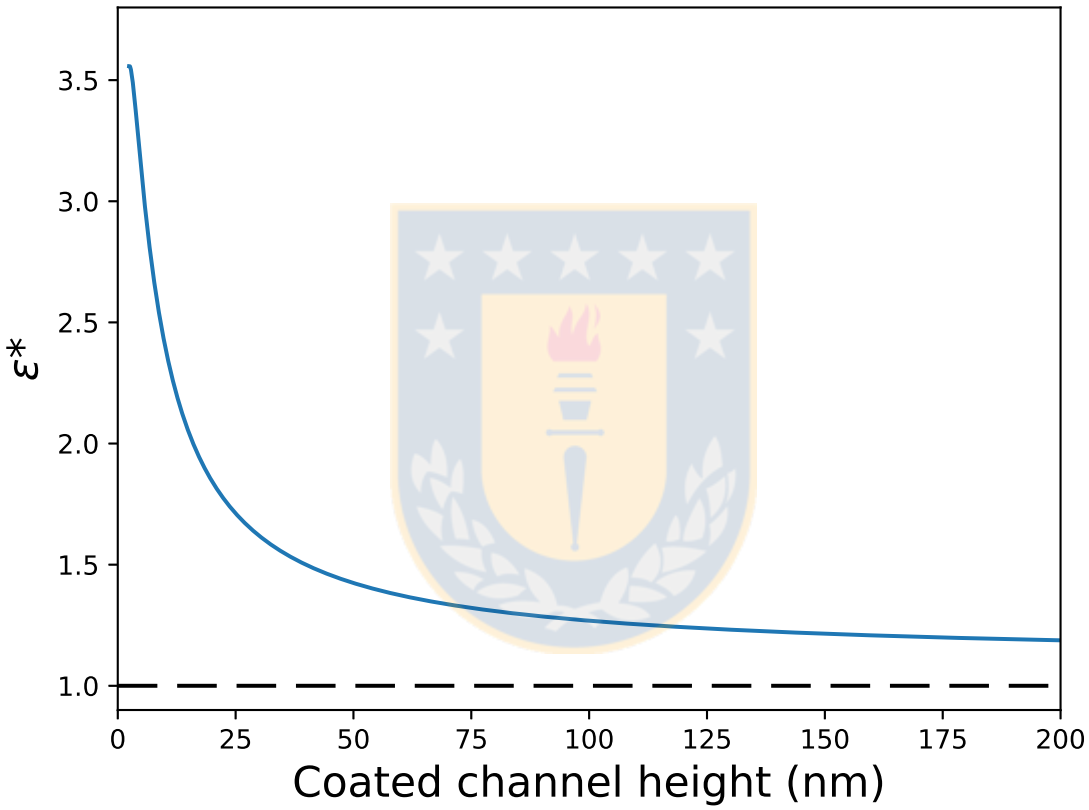

Figure 5.8: Effective enhancement as a function of coated channel height for graphene coated silica nano-channels. Effective enhancement decreases with an increase in the channel height, asymptotically reaching the unity at large heights. Source: Own elaboration.

5.5 Conclusion

MD and NEMD simulations are carried out to evaluate the effect of graphene wall coatings on the hydrodynamic properties of water in hydrophilic nanoslit channels. The nanoslits consist of two amorphous silica slabs which represent the walls of the channel confining the liquid water. The wetting of the slab surface is characterized by the water contact angle and the binding surface energy. The silica substrate coated with a graphene sheet has a WCA of 49°, whereas full wetting is achieved on the bare silica surface. A constant slip length of ca. 3.0 nm is computed for all the cases studied here. Moreover, flow enhancements ranging from 6.0 to 11.3 are computed, when comparing the measured flow rates to the theoretical no slip Poiseuille flow rates. Furthermore, when comparing flow rates in coated channels with heights of 4.4, 3.4 and 2.4 nm to the flow rates computed in the corresponding pristine silica channels, effective flow enhancements ranging from 3.2 to 3.7 are computed. Hence, our results indicate that by using GE as wall coatings leads to a considerable increase in the water flow rates in nanoslits. The flow enhancement in the graphene coated silica nanochannels reported in the present study is a significant step forward in development of functional integrated nanofluidic devices. Moreover, this study provides quantitative evidence that layers of GE could be employed as channel coating to reduce substantially the giant hydraulic resistance associated to nanoconfined liquid transport.

Chapter 6

Reduction of viscous losses in silica nanopores induced by carbon nanotube coatings.

Parts of this chapter are included in an ongoing manuscript which will be submitted for publication. Enrique Wagemann, Jens H. Walther, and Harvey A. Zambrano. "Reduction of viscous losses in silica nanopores induced by carbon nanotube coatings."

6.1 Introduction

The flow of water in nanoconfined geometries is of great scientific and practical interest, due to its potential application in a wide range of technological applications, such as water desalination, [199] Lab-On-a-Chip, [164] nanomedicine [223] and DNA sequencing. [200] As a result of the enormous ratio between surface area and confined fluid volume inherent to nanopores, the hydrodynamic properties of a fluid confined inside nanostructures are highly influenced by interfacial phenomena. Therefore, for hydrophilic nanochannels, fluid flows are generally associated to very large viscous drag. In this context, the design of efficient and functional nanofluidic devices requires new strategies to reduce hydrodynamic resistance to the fluid flow in nanoconduits.

Carbon nanotubes (CNT) are nanostructured carbon allotropes that have attracted great attention in the last decades due to their remarkable physical properties. In the last decade, studies have reported that the flow rates in carbon nanotubes are several orders of magnitude higher than those predicted in corresponding hydrophilic nanoscale pipes assuming no-slip condition. [18, 20, 25, 27, 28, 116] This low resistance to water flow and the proved high mechanical strength and chemical stability make CNTs ideal candidates as basic building blocks in novel integrated nanofluidic devices. In particular, the low friction of water in contact with CNTs has been associated to the exceptional atomic smoothness of their graphitic walls [13, 14] and to the weak interaction between water molecules and the atoms in the CNT walls. [18, 28] Nevertheless, recent reports on the effect of airborne contamintants [33] and the effect of the underlying substrates [35, 36, 119] on the wettability of supported graphene, have put in the spotlight the current understanding on the interaction of water with graphitic materials. Indeed, contradictory reports on how graphene monolayers modify the wettability of coated substrates have aroused intense debate, in particular about the influence of an atomically thin (2D) material on the interaction of water with the underlying substrate. Those studies report the influence of graphene

coating to be from complete transparency [35] to the wettability of the coated substrate to also complete opaqueness. [42,43] In particular, Shih et al. [36,119] suggest that due to its atomically thin walls, graphene is semi transparent, i.e., translucent, to the wettability of the underlying substrate. In this study, we extrapolate the translucency to wettability of graphene to its allotrope, CNT, and evaluate its effect on the hydrodynamic properties of water confined inside cylindrical silica pores.

In two recent studies, Hong et al. [121] and Ashraf et al. [120] studied the effect of voltage and chemical doping on the wettability of substrates coated with graphene. Their results show that the WCA of these surfaces can be tuned, depending on the applied chemical doping and voltage. Moreover, they suggest that this tunnability is a consequence of the shift of the graphene Fermi level, resulting in an effective modification of the interaction strength between GE and water. We take into consideration these factors by simulating the flow of water inside silica nanopores coated by a SWCNT, with an increasing strength of the interaction between CNT and water.

In the present study, we employ MD simulations to investigate whether the use of a SWCNT as wall coating in a hydrophilic silica nanopore results in a significant water flow enhancement. First, the atomistic model of a cylindrical silica nanopore coated by a SWCNT is built and characterized. The interaction between water and the pore is modeled on base of two possible scenarios; The wetting translucency reported by Shih et al. [36, 119] and the tunnability of the wetting of graphene reported by Hong et al. [121] and Ashraf et al.. [120] Subsequently, we conduct NEMD simulations to evaluate the hydrodynamic properties of water confined within the pore. Our results provide quantitative evidence that SWCNT coating the inner surface of a silica nanopore results in substantial flow enhancement in the water transport within the pore. This could represent an enabling technology for the design and fabrication of efficient integrated nanofluidic devices.

6.2 Computational methods

In this work, the simulations were carried out by employing the parallel MD package FASTTUBE, which has been used extensively to study liquids confined inside CNTs, GE layers and silica channels. [23, 24, 65, 68, 80, 151, 153, 154] The water molecules are modeled using the rigid SPC/E water. [184] The interactions between silica atoms are described using the TTAMm potential developed by Guissani and Guillot [216] which is a modification of the classical TTAM potential developed by Tsuneyuki et al.. [217] The CNT-silica interactions are described employing a Lennard-Jones potential with parameters from Zhang and Li [219] which reproduce the proper substrate-regulated morphology of GE. The carbon-carbon valence forces within the CNT are described using Morse, harmonic angle and torsion potentials. [150, 153] For further details on the employed models we refer the reader to Appendix A. The leap-frog scheme is used to integrate the equations of motion. Temperature control is achieved by employing a Berendsen thermostat. [156] Van der Walls interactions are truncated at 1 nm. To account for the electrostatic interactions between silica atoms, and in an effort to reduce computational costs, we employ a shifted Coulombic potential with a cut-off of 1 nm. The long range electrostatic interactions between water molecules and between the pore and water are calculated by employing the Smooth Particle Mesh Ewald (SPME) algorithm [161] with a real-space cutoff of 1.0 nm and a mesh spacing of 0.125 nm.

6.3 Pore setup

To create an amorphous cylindrical silica pore, we chose to amorphize crystalline silica slabs around a CNT, via consecutive thermal annealings. The methodologies reported in previous studies [54, 224, 225] suggest to create an amorphous silica slab starting from a crystalline structure and then drill it and expose it to subsequent thermal annealings. While these procedures generate well defined pores, the roughness on the inner surface of the structure is not properly described due to the initial artificial cutting process. Therefore, in order to avoid the deformation of the CNT due to the presence of artificially large surface roughness, we decide to include the CNT during the annealing procedure (the practical effect of the CNT is to act as a barrier to the silica atoms during the thermal annealing, forcing them to maintain the cylindrical shape of the pore).

The protocols followed here to build the pore consist of several consecutive steps. First, the initial configuration is created. We start with a (39,39) Armchair CNT, which is periodic in the z-direction. The CNT is composed by 6552 carbon atoms and has a length of 10.33 nm and a diameter of 5.289 nm. Then, 15 replicated β crystoballite slabs are symmetrically distributed around the CNT. The resulting system has a "flower-like" shape, as depicted in Figure 6.1 a. Each slab consists of 4096 Si atoms and 8192 O atoms (184320 silica atoms in total) and has dimensions of $10.112 \times 1.264 \times 10.112$ nm. Furthermore, the surfaces of the silica slab pointing towards the CNT project a regular polygon of 15 sides in the xy plane. Hence, the angle between surfaces is 156°. In Figure 6.2, a schematic representation of the initial configuration of the silica slab is shown. The simulation box has an orthorhombic shape, with dimensions of $30.2 \times 30.2 \times 10.33$ nm. These dimensions were chosen to avoid artificial strain in the CNT along the z-direction and to avoid the interaction between the specular images of the silica slab due to periodical boundary conditions in the x and y-directions.

After the initial configuration is generated, the system is annealed by connecting to a heat bath following a protocol based on the work of Zambrano et al.. [218] In this first thermal annealing, silica is heated to 3000 K during 10 ps, followed by a subsequent quenching of the system from 3000 K to 300 K using a cooling rate of $70\,\mathrm{K\,ps^{-1}}$. During this phase a time step of 1 fs is employed. Silica atoms are coupled to the Berendsen thermostat, with a coupling constant of 0.005 ps, while the position of the carbon (C) atoms in the CNT is maintained fixed. Note that C atoms are still interacting with the Si and O atoms. When the simulation ends, we define the atoms whose distance to the center of mass (COM) of the CNT is less than 4.1445 nm (radius of the CNT + 1.5 nm) as atoms in the inner surface of silica (inner silica). Whereas, the rest of the silica atoms are defined as outer silica atoms (outer silica). The resultant system of this thermal annealing is depicted in Figure 6.1 b.

As a result of the initial thermal annealing, the position of the silica atoms is randomized. However, some unwanted features of the initial configuration are still present, such as the remaining "arms" observed in Figure 6.1 b. Therefore, a second process of thermal annealing is conducted to obtain a more homogeneous external pore shape. In this annealing process, the outer silica atoms are heated to 5000 K during 10 ps, followed by a subsequent quenching from 5000 K to 300 K using a cooling rate of $70\,\mathrm{K\,ps^{-1}}$. Moreover, during the annealing, the positions of the C atoms in the CNT and the inner silica atoms are maintained fixed to avoid the modification of the surface features. The simulation is conducted over 250 ps. Afterwards, a simulation to equilibrate the atoms in the inner silica and CNT is conducted. In this simulation, the temperature of the system is maintained at 300 K by coupling the inner silica and C atoms to a thermostat, while the positions of the outer silica atoms are maintained fixed. This simulation

is conducted over 200 ps with a timestep of 1fs. The resultant system is shown in Figure 6.1c.

Finally, atoms in the outer silica are removed to obtain a pore with an orthorhombic external shape coated with a coaxial CNT. The cuts were made to obtain a silica substrate with at least a thickness of 3.4 nm (in the x and y-direction). The final system has dimensions of $12.09 \times 12.09 \times 10.33$ nm. Afterwards, in order to maintain electroneutrality, a ratio of 1 to 2 between the number of Si and O atoms is enforced by randomly removing atoms from the external surface of the system. The final number of atoms in the system is: 29069 Si atoms, 58138 O atoms and 6552 C atoms. Subsequently, periodicity is enforced in all directions by employing a simulation box of dimensions equal to the resultant system.

6.4 Pore characterization

A proper characterization of the pore features is key to analyze the water transport inside the system. Here, we report some relevant features of the generated pore and the methodologies employed to measure them.

6.4.1 CNT radius and bond length

The radius of the CNT is measured by averaging the distance of the C atoms to the COM of the system in the xy plane. A radius of 2.6209 nm, with a standard deviation of 0.0653 nm is computed. No significant variation is observed when comparing the CNT radius before and after the pore setup, as the radius was initially 2.6445 nm. Nevertheless, an increase in the corrugation of the CNT is observed, as the standard deviation of the radius achieved a not zero value. This increased corrugation is a result of the interaction between CNT and the rugosities of the silica substrate. Moreover, an average C-C bond length of $0.14213 \pm 1.6 \cdot 10^{-5}$ nm was calculated by averaging the distance between bonded C atoms. This value suggests a low strain in the CNT. [118]

6.4.2 Uncoated pore radius

In order to estimate the radius of the uncoated pore, i.e., the pore without the inner CNT, the distance between the surface Si and O atoms to the COM of the system in the xy plane is measured. In order to measure the radius, a cylindrical binning sampling method was employed. The bins have a size of 0.2 nm in the z-direction and an angular size of 4.5°. In each bin, the distance of each atom to the COM of the system was computed, and the minimum distance was defined as the radius. Then, the computed radii are averaged. The resulting average radius has a value of 3.155 nm with a standard deviation of 0.285 nm. Furthermore, the standard deviation of the radius is four times larger, indicating larger surface rugosities for the uncoated pore. It should be noted that the measured radii for the CNT coated and bare pore do not consider the size of the carbon atoms nor silica atoms. Therefore, corrections should be made for further analyses.

6.4.3 Silica density profile

The silica density profile, depicted in Figure 6.3, is computed by employing cylindrical binning. Each concentric bin length in the z-direction is equal to the size of the simulation box and has a radial size of 0.01 nm. The density in each bin was computed by summing the mass points of each atom inside the bin and dividing by the volume of the bin. Moreover, in an effort to get

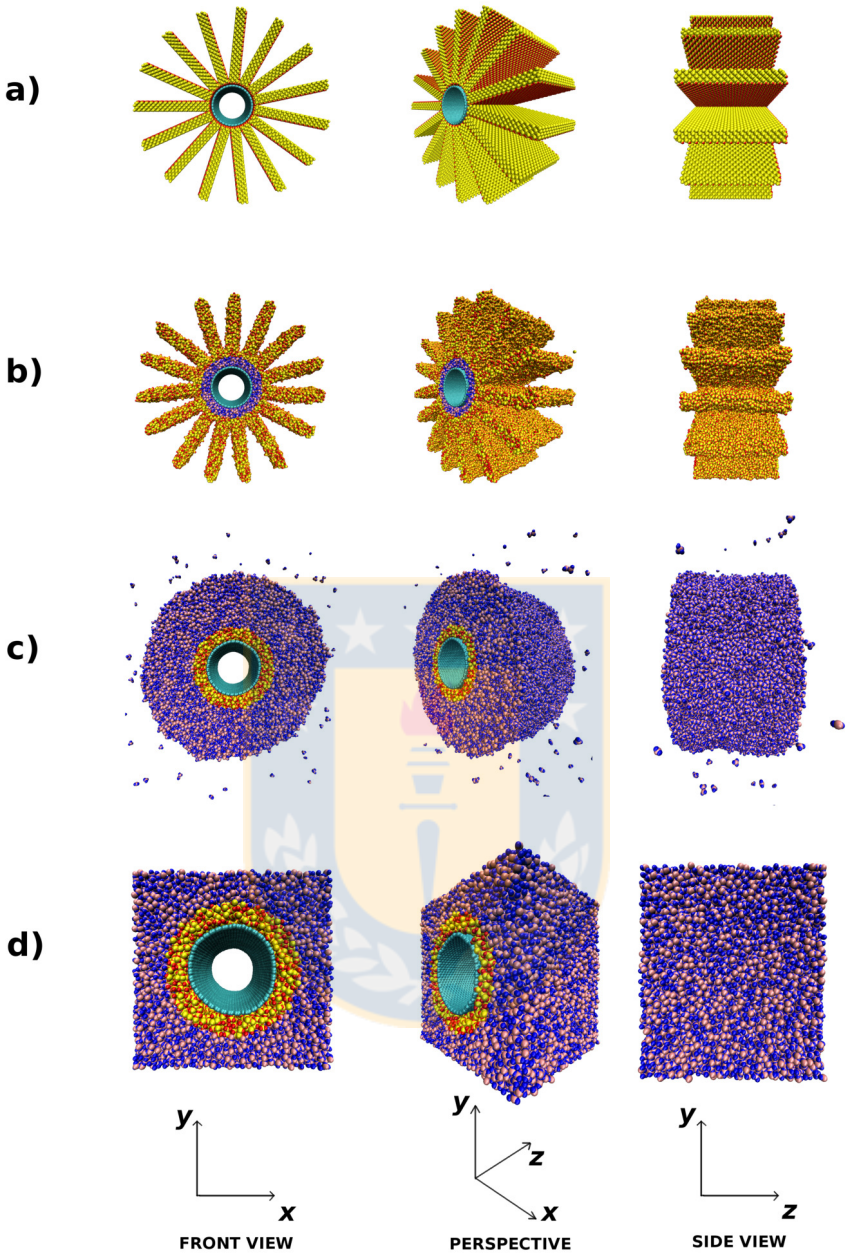

Figure 6.1: Different stages of the silica pore setup. The yellow and red atoms correspond to Si and O atoms. The pink and blue atoms correspond to Si and O atoms, whose positions are maintained fixed. The cyan atoms correspond to C atoms in the CNT. a) Initial configuration. b) Pore after the initial thermal annealing, the positions of the inner silica atoms is maintained fixed during the subsequent thermal annealing. c) Pore after the second thermal annealing, the positions of the outer silica atoms is maintained fixed for the rest of the simulations, while the inner silica and CNT atoms are kept active and coupled to the thermostat. d) Final configuration of the pore, atoms from the external silica are removed to obtain an orthorhombic external shape. Source: Own elaboration.

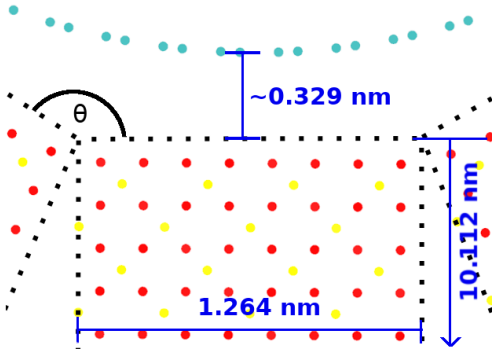

Figure 6.2: Schematic representation of the initial configuration of the crystalline silica slab employed in the construction of the CNT coated silica pore. The yellow dots represent Si atoms, whereas the red atoms represent O atoms and the cyan dots C atoms. Source: Own elaboration.

information about the structure of the silica-CNT-water interface, we fit the density profile to the function:

$$\rho_{SiO_2}(r) = a_1 \cdot \left[1 + \tanh\left(\frac{r - r_0}{b_1}\right)\right] \tag{6.1}$$

where $\rho_{SiO_2}(r)$ is the radial density, a_1 is a constant value proportional to the bulk density, b_2 is a constant value proportional to the thickness of the interface and r_0 is the layer boundary. [54] These parameters are represented in Figure 6.3. From the fitted parameters a bulk density of 2354 kg/m^3 is estimated as $\rho_{bulk} = 2 \cdot a_1$ and a silica interface with thickness of 0.38 nm, as $l_{interface} = 4 \cdot b_1$. Additionally, the point where the bulk density is reached (3.181 nm) is estimated as $r_{bulk} = r_0 + 2 \cdot b_1$. This value is within the statistical error to the radius of 3.155 nm measured as the distance between silica atoms and the COM of the system.

6.4.4 Distance between the CNT and the silica surface

The contact distance between the surface of a substrate and a supported 2D material plays a key role in the translucency to the wettability phenomena, [36,37,119] thus a proper description of the contact surface is essential. Previous computational studies on the wettability translucency have employed crystalline substrates, [37,38,40,226] hence the determination of the contact distance for these systems remains trivial. However, in the present study we employ an amorphous substrate, whose surface presents large non-homogeneous rugosities that difficult the determination of a contact distance. Nevertheless, some distances already measured can shed light on this problem.

A first approach to measure the contact distance consists in calculate the difference between the computed radii, resulting in distance of 0.5341 nm. However, this distance does not consider the van der Waals size of the atoms or the steric effect of the surface roughness. Hence, a correction is made by subtracting the average σ of the C-Si and C-O interactions (0.1881 nm). The corrected contact distance is 0.346 nm. Similar distances (0.5601 nm and 0.372 nm with correction) are recovered when measuring the distance between the CNT atoms and the point wherein silica density reaches bulk value. Moreover, other relevant distances can be measured from the silica radial density profile depicted in Figure 6.3, e.g., the 0.38 nm thickness of the silica interface. Furthermore, a distance of 0.369 nm is recovered when comparing r_{cnt} and r_0.

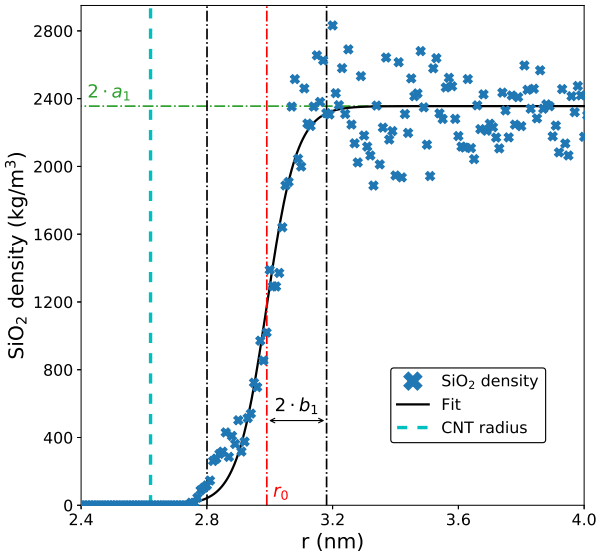

Figure 6.3: Silica radial density profile of the studied CNT coated silica pore. An hyperbolic tangent function (eq. 6.1) is fitted to the density profile to define the interface. Source: Own elaboration.

Despite the difficulties in measuring a contact distance in our system, we measured distances of interest, each one with its own physical meaning. Based on these values, we define a contact distance whose value ranges from 0.34 nm to 0.38 nm.

6.4.5 Surface dangling atoms concentration

The concentration of nonbridging [224] or dangling atoms (DA) has an important influence on the wettability of a silica surface. [54] A dangling atom is defined as an atom that is not completely connected, i.e., fully bonded. In order to measure the concentration of dangling atoms, first the distance between Si and O atoms is measured. If the distance between two atoms is less than 0.2 nm these atoms are considered bonded. Moreover, if a Si atom has less than 4 bonds it is considered as a dangling silicon (DSi). Additionally, if an O atom has less than 2 bonds, it is considered as a dangling oxygen (DO). The number of dangling atoms is then divided by the surface area, which we estimate as the surface of a cylinder whose radius equals to r_0. The position of the dangling atoms in our system projected to the xy plane is presented in Figure 6.4, along with some reference radii. The measured dangling atoms density are: $[DSi] = 0.129\,\mathrm{nm}^{-1}$, $[DO] = 1.875\,\mathrm{nm}^{-1}$ and $[DA] = 2.004\,\mathrm{nm}^{-1}$. These values are in agreement with previous studies. [54, 218]

6.4.6 Solvent Accessible Surface Area

We measured the Solvent Accessible Surface Area (SASA) of the system, i.e, the avalaible area of the pore surface accesible by the water molecules, by employing the SASA command provided in VMD. [227] An expanded atom radius of 0.2 nm was used for this purpose. The SASA was

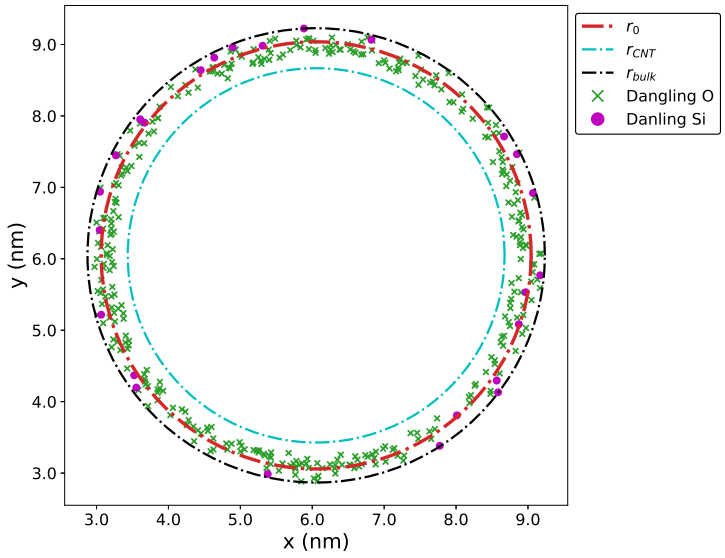

Figure 6.4: Dangling atoms in the CNT coated silica pore system. A silicon atom is defined as dangling if it is bonded to less that 4 oxygen atoms, whereas an oxygen atom is defined as dangling if it is bonded to less than 2 silicon atoms. Source: Own elaboration.

estimated by considering the substrate atoms with a z position between 1.0 and 0.9 nm and x and y positions between 1.0 and 11.0 nm. This procedure allows to ignore in the computation the atoms in the external surface of the pore. For the bare Silica surface a SASA of 191.52 nm^2 was measured, whereas a SASA of 116.78 nm^2 was measured for the coated pore. A clear decrease in the SASA is observed when coating the pore. Moreover, the ratio between SASA and projected surface area for the bare pore is 1.27 and 1.008 for the coated pore, which confirms a decrease in the surface roughness for the coated surface.

6.5 Pore-Water interactions

In this study, the interaction between water and solid is modeled based on two possible scenarios. In the first scenario, CNT is translucent to the wettability of the underlying silica, due to its atomically thin wall. The interaction between water and solid is therefore modeled as the sum of two interactions; water-CNT and water-silica. All the cases that model this scenario will be denominated as "translucency cases" from now on. In the second possible scenario, the underlying substrate influences only indirectly the water behavior by altering the strength of the CNT-water interaction and by imposing a physical corrugation in the CNT, without any direct interaction between underlying substrate and water. Therefore, the interaction between water and solid is modeled only in base of the interaction between carbon and oxygen atoms. The cases that model this scenario will be depicted as "opaqueness cases" for simplicity. Note that in this scenario the CNT atoms still interacts with the silica atoms. However, water molecules do not interact with the silica atoms.

The water-CNT interaction is described using the Lennard-Jones potential betwee O and C

atoms. In the translucency cases, we employ the parameters of Werder et al. [80] that recover a macroscopic WCA of 86° on graphite. The parameters for this potential are $\sigma = 0.319\,\text{nm}$ and $\varepsilon = 0.392\text{kJ/mol}$. In the opaqueness cases, the ε parameter of the potential is tuned to account for an increasing strength of the interaction.

In the translucency cases, the van der Waals interactions between silica atoms and water molecules are described using a Buckingham potential (eq. 3.4) with parameters taken from the work of Zambrano et al. [218] and the work of Hassanali and Singer. [228] The strength of the interaction is systematically increased by modifying the C_{ij} parameter of the interaction between O_{H_2O} and O_{SiO_2} atoms. The values for the used parameters are listed in table 6.1. Further details on the employed potentials can be found in Appendix A. Note that in both scenarios, silica atoms interact with the C atoms in the CNT.

Table 6.1: Silica-water interaction parameters. Source: Own elaboration.

Pair	C_{ij} ($\text{kJ nm}^6\,\text{mol}^{-1}$)	α_{ij} (kJ mol^{-1})	ρ_{ij} (nm^{-1})
O_{SiO_2}-H_{H_2O} [228]	0.0	6.8307×10^3	32.6584
O_{SiO_2}-O_{H_2O} [228]	tuned	2.7401×10^5	31.4355
Si-O_{H_2O} [218]	0.0240	1.0130×10^5	25.0

6.5.1 Energy Landscape

The interaction between the water and the substrate is characterized by measuring the potential energy between a single water molecule and the atoms in the solid. The potential energy is measured in each case by systematically changing the position of the molecule in z, r and θ, as depicted in Figure 6.5. Each displacement corresponds to a Δz, Δr or $\Delta(\frac{\theta}{2\pi} \cdot r)$ of 0.01 nm. Additionally, the molecule is rotated, so it maintains its original angle with respect to the COM in the xy plane. Moreover, we take into account the orientation of the molecule, by averaging 12 cases that represent consecutive 90° rotations of the molecule from its original position with respect to r,z and θ. The position of the C atoms is interpolated into a mesh with a spacing of 0.01 nm x 0.01 nm. The distance of each molecule to r_{cnt} (r_{C-H_2O}) is measured by comparing the position of the O atom with respect to the nodes of the interpolated mesh. Finally, the potential energy measured for molecules with the same r_{H_2O-C} is averaged.

The measured potential energy values as a function of the distance between CNT and water molecule (r_{C-H_2O}) for the translucency cases, as a function of $C_{O_{SiO_2}-O_{H_2O}}$ are presented in Figure 6.6. Additionally, the potential energy values for the opaqueness cases are presented in Figure 6.7. The dashed lines included in the plots correspond to a fit to the Mie potential:

$$U(r_{C-H_2O}) = \left(\frac{n}{n-m}\right)\left(\frac{n}{m}\right)^{m/(n-m)} \varepsilon \left[\left(\frac{\sigma}{r}\right)^n - \left(\frac{\sigma}{r}\right)^m\right] \tag{6.2}$$

For the opaqueness cases, σ was found to be constant, with a computed value of 0.2659 nm. In the same way, n and m are constants with values of 9.184 and 4.033. In contrast, ε was found to increase linearly with $\varepsilon_{C-O_{H_2O}}$, as depicted in Figure D.1 of Appendix D. In the translucency cases, all the parameters are linearly dependent to $C_{O_{SiO_2}-O_{H_2O}}$. The parameters calculated for the opaqueness cases are presented in Figure D.2 of Appendix D. Furthermore, the standard deviation for every average potential energy calculated is depicted in Figure 6.8. In general, the standard deviation in the translucency cases is higher than in the opaqueness cases, indicating that the interaction with silica increases the energy corrugation [20] felt by the water molecule.

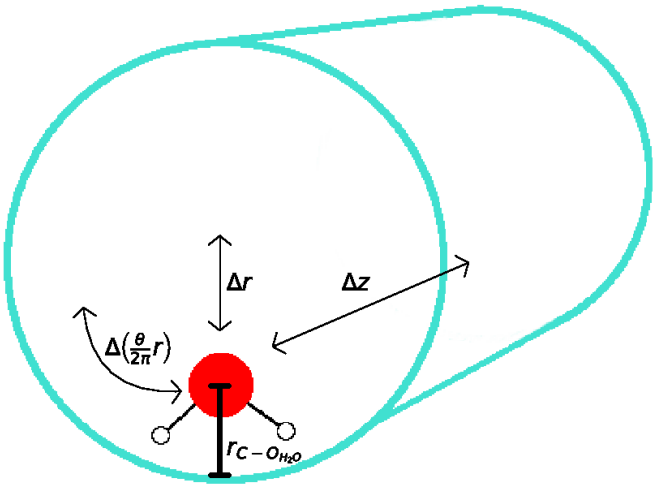

Figure 6.5: Schematic representation of the translations employed to survey the surface potential energy of the CNT coated silica pore. Source: Own elaboration.

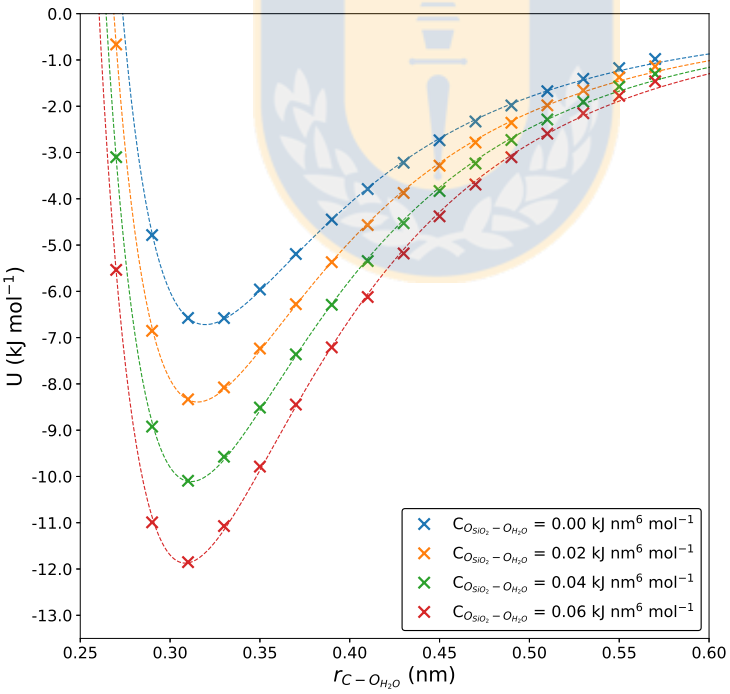

Figure 6.6: Potential energy between a single water molecule and the CNT coated silica pore as a function of the distance between the CNT and the water molecule ($r_{C-O_{H_2O}}$) for the translucency cases. The dashed lines represent a fit to the Mie potential. Source: Own elaboration.

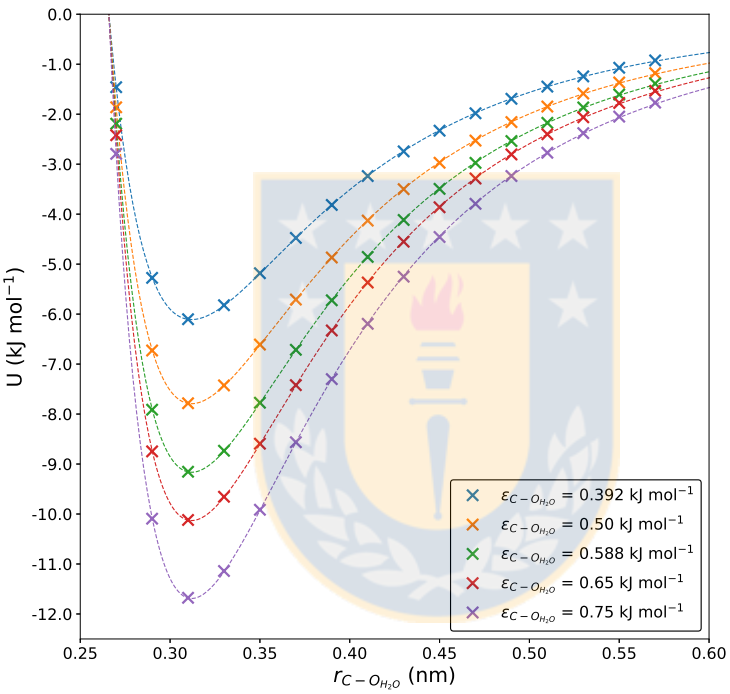

Figure 6.7: Potential energy between a single water molecule and the CNT coated silica pore as a function of the distance between the CNT and the water molecule ($r_{C-O_{H_2O}}$) for the opaqueness cases. The dashed lines represent a fit to the Mie potential. Source: Own elaboration.

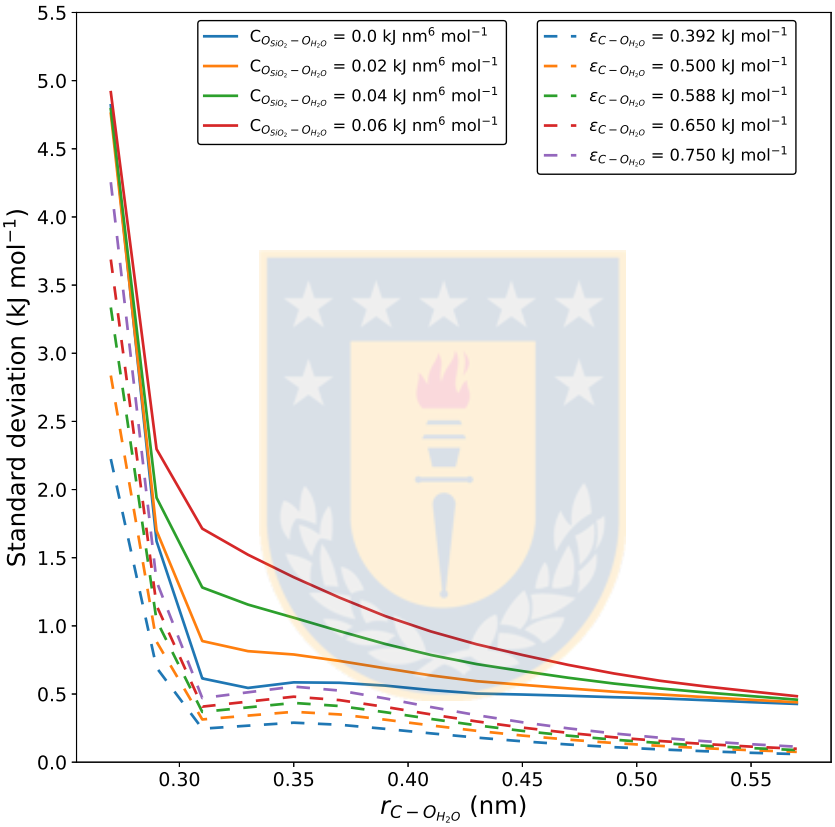

Figure 6.8: Standard deviation of the calculated potential energy between a single water molecule and the CNT coated silica pore as a function of the distance between the CNT and the water molecule ($r_{C-O_{H_2O}}$). In general, the translucency cases present larger standard deviations, indicating larger surface energy corrugation. Source: Own elaboration.

6.5.2 Water contact angle

The water contact angle on the inner surface of the coated pore is measured by confining a water droplet inside it which was previously equilibrated. In order to measure the WCA of a sufficiently large droplet, while avoiding the effect of the periodic boundary conditions, the pore was extended twice along the z-direction. The dimensions of the new system are $12.09 \times 12.09 \times 30.99$ nm and consists of 261261 silica atoms and 19656 carbon atoms. During the simulations to measure the WCA, the positions of the silica and carbon atoms are maintained fixed. The temperature is controlled by coupling the water molecules to a Berendsen thermostat with a coupling constant of 0.1 ps. Moreover, a timestep of 2 fs is used to integrate the equations of motion.

First, a water droplet of 7000 molecules is equilibrated in the pore during 500 ps. In this first step, water molecules are coupled to the thermostat and interact only with the C atoms, using the parameters of Werder et al.. [80] The resulting system is used as an initial configuration for the rest of the systems. The effect of $\varepsilon_{C-O_{H_2O}}$ on the WCA in the opaqueness cases is measured by systematically increasing its value. Additionally, the effect $C_{O_{SiO_2}-O_{H_2O}}$ in the translucency cases is also systematically studied. A snapshot of a WCA system is presented in Figure 6.9. After modifying the parameters in the potential, each system is equilibrated for another 500 ps. In this second step, the water molecules are still coupled to the thermostat. Afterwards, the thermostat is disconnected and the system is equilibrated for 250 ps in NVE. Finally, we simulate 1 ns to extract data every 10 ps. The local water density is computed by employing a cylindrical binning sampling method. Each bin is defined by radially and tangentially dividing a cylinder, with center in the axis of the pore, into bins of size 0.05×0.05 nm in r and z. A schematic representation of the employed binning sampling method is presented in Figure D.3 of Appendix D. In order to find the droplet boundary, each radial layer is fitted to the function: [54]

$$\rho_{H_2O}(z) = a_{H_2O} \cdot \left[1 + tanh\left(\frac{x - x_{0_{H_2O}}}{b_{H_2O}}\right)\right] \tag{6.3}$$

Then, the obtained layer boundaries $x_{0_{H_2O}}$ are fitted to a circular function, as depicted in Figure 6.10. Note that layers associated to large statistic uncertainty are not considered in the fit. The contact angle is calculated as the angle of a line tangent to the circular fit, at the CNT surface. The van der Waals radius of carbon atoms is considered to determine the position of the CNT surface.

In Figure 6.11, the WCA values for the cases of transluency and opaqueness are presented. A linear dependence between WCA values and tuned parameters is observed for both cases, as depicted in the same figure. The computed potential energies, between droplet and substrate, as a function of the tuned parameters and as a function of the WCA are depicted in Figure D.4 and Figure D.5 of Appendix D. When comparing the potential energy resultant of the interaction between the droplet and the pore for cases with the same WCA, a difference is observed with larger values for the translucency cases. This difference hints that, despite reproducing the same wettability, translucency and opaqueness cases reproduce different potential energies landscapes, which is in agreement with the difference observed in the measured potential energies landscapes for a single water molecule inside the pore. Nevertheless, thanks to these measurements, a proper characterization of the interactions between water and the pore based on a macroscopic observable (WCA) is achieved.

6.6 Hydrodynamics of water confined within the pore

Once the physical properties of the pore and its interactions with water are properly characterized, we proceed to study the hydrodynamics of water confined inside the pore. To study the flow enhancement induced by the CNT coatings, Poiseuille like flow of water is simulated in the pore with a SWCNT coating the pore surface.

6.6.1 Filling of the pore

In order to achieve an adequate filling of the pore, we conduct simulations of water confined within the pore. The employed system is depicted in Figure 6.12. We employ two external GE layers, perpendicular to the CNT axis, to confine the water molecules. One of the GE sheets is used as a piston, by applying a constant external field (F_c) in direction parallel to the pore axis on all carbon atoms in the motile sheet, whereas the positions of the carbon atoms in the other sheet are maintained fixed. An internal pressure of 1 bar in the confined water is attained by setting $F_c = 1.35888 \cdot 10^{-4}$ nm/ps^2. Moreover, we employ two internal GE layers to avoid the adsorption of water molecules into the silica substrate and to avoid molecules entering the spacing between CNT and silica, as depicted in Figure 6.12. A circular cut with a diameter equal to the CNT diameter is made to the internal GE layers, and then they are connected to the CNT by linearly modifying z position of the C atoms within a distance of 0.5 away from the cut, resulting in an entrance of the pore with a truncated cone shape. During this set of simulations, the position of the silica and C atoms is maintained fixed. The temperature of the system is controlled by coupling the water molecules to a Berendsen thermostat, with a coupling constant of 0.1 ps. The equations of motion are integrated by employing a timestep of 2 fs.

We study the effect of the employed wettability models on the water filling by systematically increasing the value of $\varepsilon_{C-O_{H_2O}}$ in the opaqueness cases and $C_{O_{SiO_2}-O_{H_2O}}$ in the translucency cases. Each case is equilibrated for 100 ps and then another 600 ps are conducted to extract trajectory data. The number of water molecules per length of the CNT is calculated by averaging the number of molecules inside the pore over time. Note that the effect that the additional GE sheets could have on the filling is avoided by making all the measurements at least 1 nm away from the additional sheets. In Figure 6.13, we present the calculated number of water molecules per length of CNT required to fill the pore at an internal pressure of 1 bar, for both scenarios. A linear fit is applied to the values for both scenarios, as depicted in the same figure, in order to interpolate the required amount of molecules for the subsequent flow cases.

6.6.2 Poiseuille Flow

In this study, fluid flow is generated by imposing a constant external field to all water molecules confined inside the pore. The values of the applied external fields range from 1.5 x 10^{11} to 6 x 10^{11} m/s^2. The employed external fields correspond to pressure gradients ranging from 2 bar/nm to 6 bar/nm. Removal of viscous heating is achieved by extracting heat through the walls. To this end, the internal silica atoms and the carbon atoms of the CNT are coupled to the Berendsen thermostat, with a coupling constant of 0.005 ps. The position of atoms in the outer silica is maintained fixed through all the simulations. Each simulation is conducted for 500 ps in order to reach steady state, and then for another 2 ns to extract data of the trajectories every 10 ps. The radial velocity profiles are calculated by employing a cylindrical binning sampling method, with a radial binning spacing of 0.3 nm. A schematic representation of the employed binning sampling method is presented in Figure D.6 of Appendix D.

The velocity profile exhibits a parabolic shape with significant wall slippage, as depicted in Figure 6.14. The fluid velocity at the CNT surface, i.e., the slip velocity (u_s) in each case is estimated from a parabolic fit applied to each calculated velocity distribution. The slip length (l_s) to each studied system is then calculated by following the P3 procedure of Kannam et al.. [19] This method consists in applying a linear fit to the calculated slip velocity as a function of the applied external field. Then, from the slope (m) of the linear fit, the slip length is calculated as:

$$l_s = \frac{2m\mu_0}{\rho R} \tag{6.4}$$

where, m represents the slope of the fit, μ_0 is the bulk viscosity of the fluid, ρ is the overall density of the fluid (total mass of water in the system divided by the available volume inside the pore) and R is the CNT radius, corrected to consider the van der Waals size of the carbon atoms. Due to the relatively large diameter of the CNT used here, employing the bulk viscosity of the fluid is a suitable asumption. [28, 117] In Figure 6.15, we present this procedure for a translucency case with a $C_{O_{SiO_2}-O_{H_2O}}$ of 0.035kj nm^6 mol^{-1}. The calculated slip length for all the studied cases is presented in Figure 6.16. Moreover, the flow ehnancement (ε), i.e, the ratio between the flow of water inside the pore and the no-slip Poiseuille flow prediction, is depicted in the same figure. The ε is estimated as: [18]

$$\varepsilon = 1 + \frac{8l_s}{D} = 1 + \frac{16l_s}{R} \tag{6.5}$$

The calculated l_s for the translucency cases range from 5 to 30 nm, whereas the l_s calculated for the opaquenes cases range from 25 to 50 nm. In both cases a linear dependence between l_s and WCA is observed. Moreover, the calculated l_s for the opaqueness cases are up to 4 times larger, when compared to the ones calculated for the translucency cases. This difference can be explained by the difference in the surface energy corrugation, depicted in Section 6.5.1, and is consistent with the results of previous studies that have considered this effect on the flow of water confined between graphitic materials. [13, 20, 118]

The calculated ε for the translucency cases range from 10 to 50, meaning that the flow of water in the pore is at least 10 times higher than the one predicted by the no-slip Poiseuille equation. Therefore, an important reduction in the hydrodynamic losses is expected by implementing SWCNT as surface coatings in silica nanopores. Furthermore, the flow enhancement for the opaqueness cases range from 40 to 80 and is significantly larger than the one calculated for the translucency cases.

Whereas CNT is translucent to wettability or not, is an open question. Nevertheless, our results indicate that the use of SWCNT as coatings is a feasible alternative to produce an enhancement in the nanoconfined flow of water, and therefore, to reduce the enormous hydrodynamic losses associated to pump water in hydrophilic confinement. In future works, we expect to confirm this hypothesis even further by simulating the flow of water inside the uncoated pore. Moreover, the importance of the surface roughness, i.e., the energy corrugation felt by the interfacial water molecules, will be studied by simulating the flow of water inside CNTs without the corrugations imposed by the underlying silica substrate.

6.7 Conclusions

MD and NEMD simulations are carried out to evaluate the effect of SWCNT coatings on the hydrodynamic properties of water in a hydrophilic silica nanopore. For this purpose, the atomistic

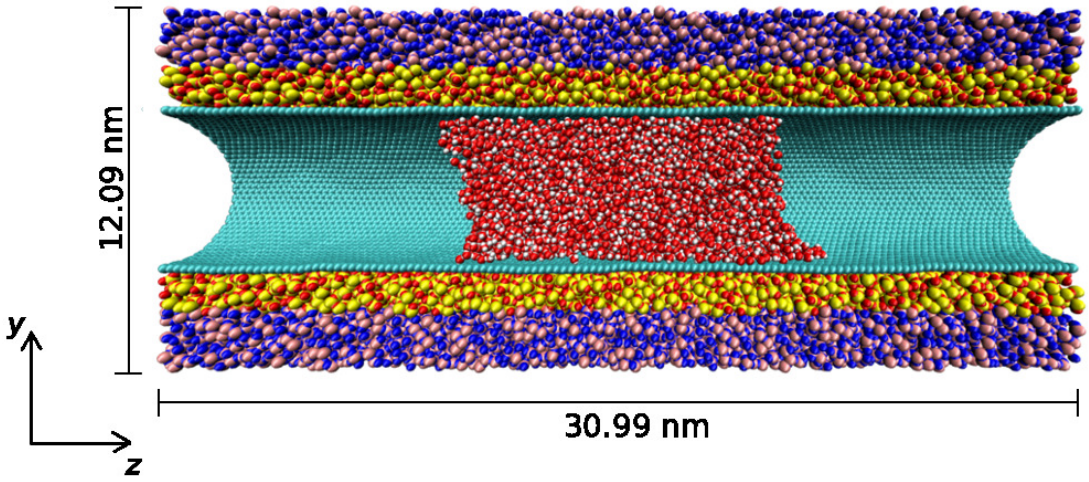

Figure 6.9: Snapshot of a water contact angle simulation. A water droplet is equilibrated inside the CNT coated silica pore to measure the average WCA. Source: Own elaboration.

model of a cylindrical silica nanopore, internally coated by a (39,39) SWCNT, is successfully characterized. The interaction between water molecules and the pore is modeled based on two possible scenarios: the translucency to wettability of CNTs and the tunability of the interaction strength between CNT and water. In the translucency scenario, water molecules interact with the underlying silica substrate atoms and the CNT atoms. In contrast, in the opaqueness scenario water molecules interact only with the carbon atoms of the CNT. In both scenarios the interactions between water and solid walls are characterized by measuring the WCA and the surface energy potential. Moreover, the effect of wettability on the interfacial slippage is systematically studied by simulating Poiseuille flow of water, under different strengths of the water-pore interactions. Our results confirm the dependence between slip length and WCA. Furthermore, different slippage are computed for the two scenarios considered in the present study. These differences in slippage can be explained by the different surface energy corrugation as a result of the particular wettability model describing the interfacial interaction for each scenario. Although the difference between the wettability models, our results indicate that a significant flow enhancement is induced by employing a single walled CNT as coating in hydrophilic nanopores.

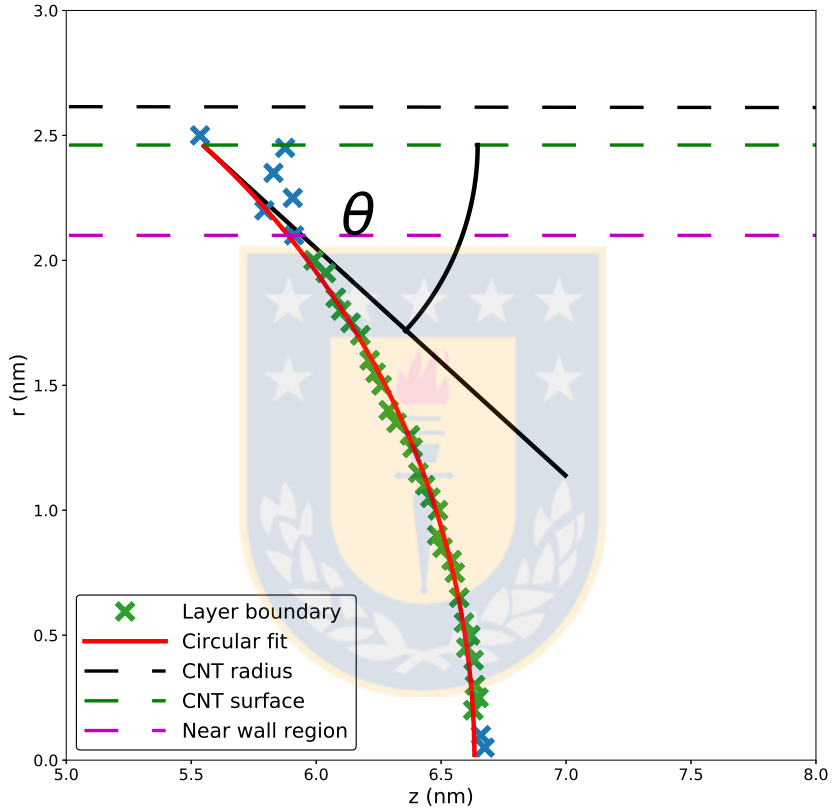

Figure 6.10: Calculation of the water contact angle inside the CNT coated silica pore. The boundary layer, obtained from a fit to equation 6.3 for each radial layer, is fitted to a circular function. The contact angle is then estimated from the circular fit. Data with large statistic uncertainty (blue) are not considered in the fit. Source: Own elaboration.

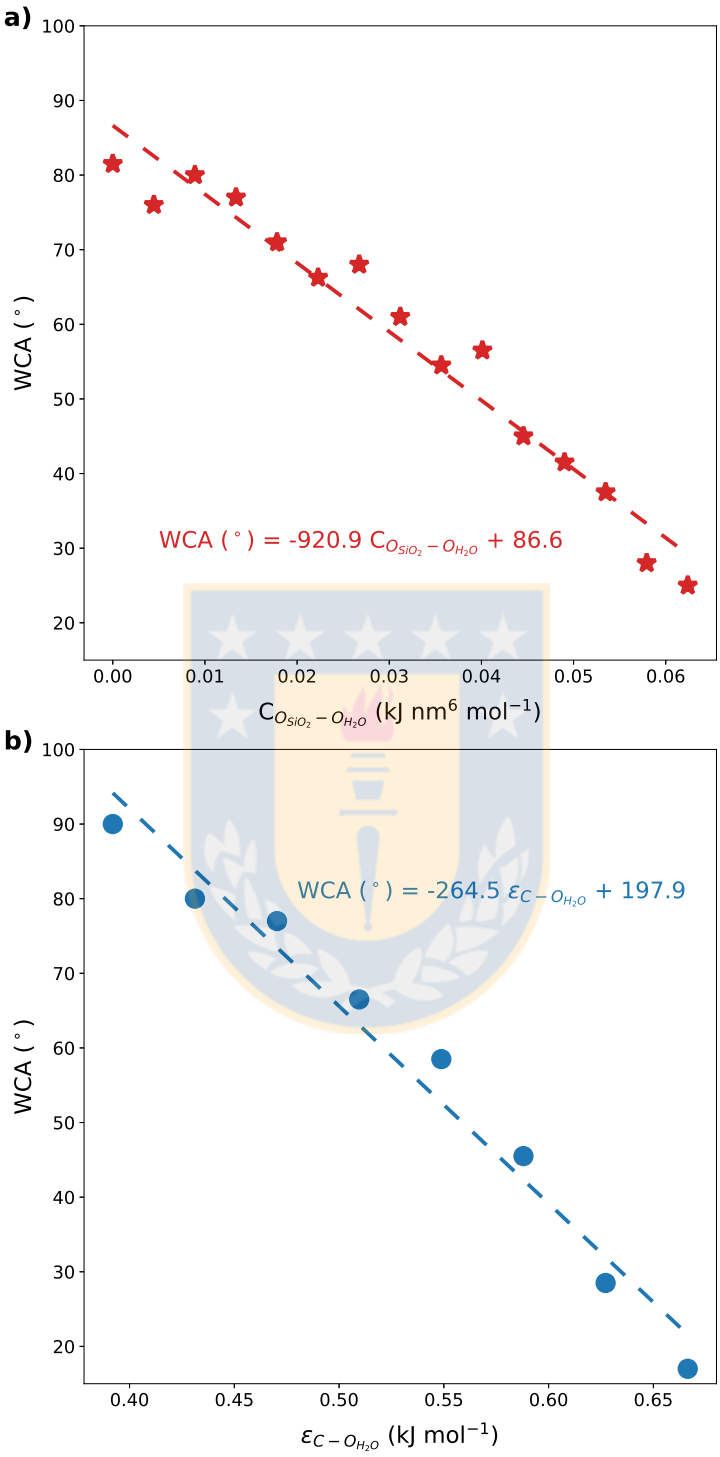

Figure 6.11: Calculated water contact angles in the CNT coated silica pore. a) Contact angle for the translucency cases. b) Contact angle for the opaqueness cases. The dashed lines represent a linear fit applied to the calculated WCAs. Source: Own elaboration.

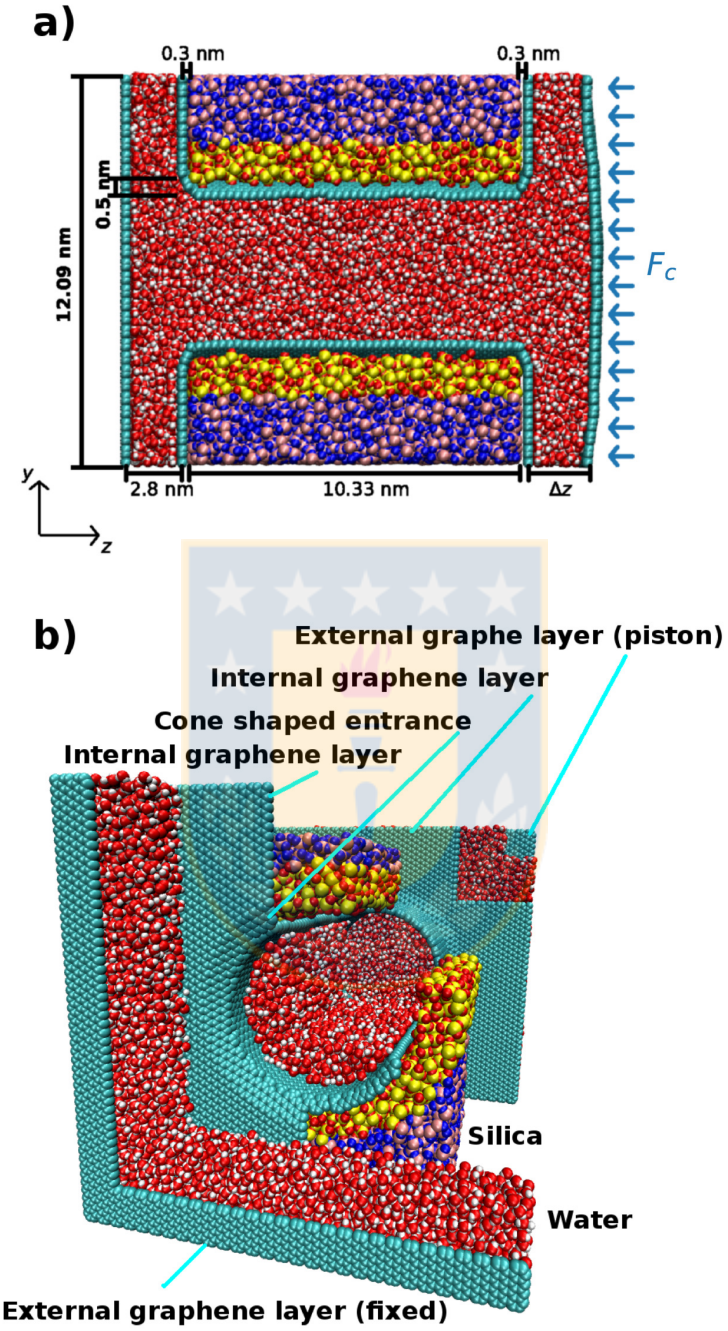

Figure 6.12: Snapshot of a simulation of the filling of the CNT coated silica pore. A graphene layer is employed as a piston to attain an internal pressure of 1 bar. a) Side view. b) Perspective. Source: Own elaboration.

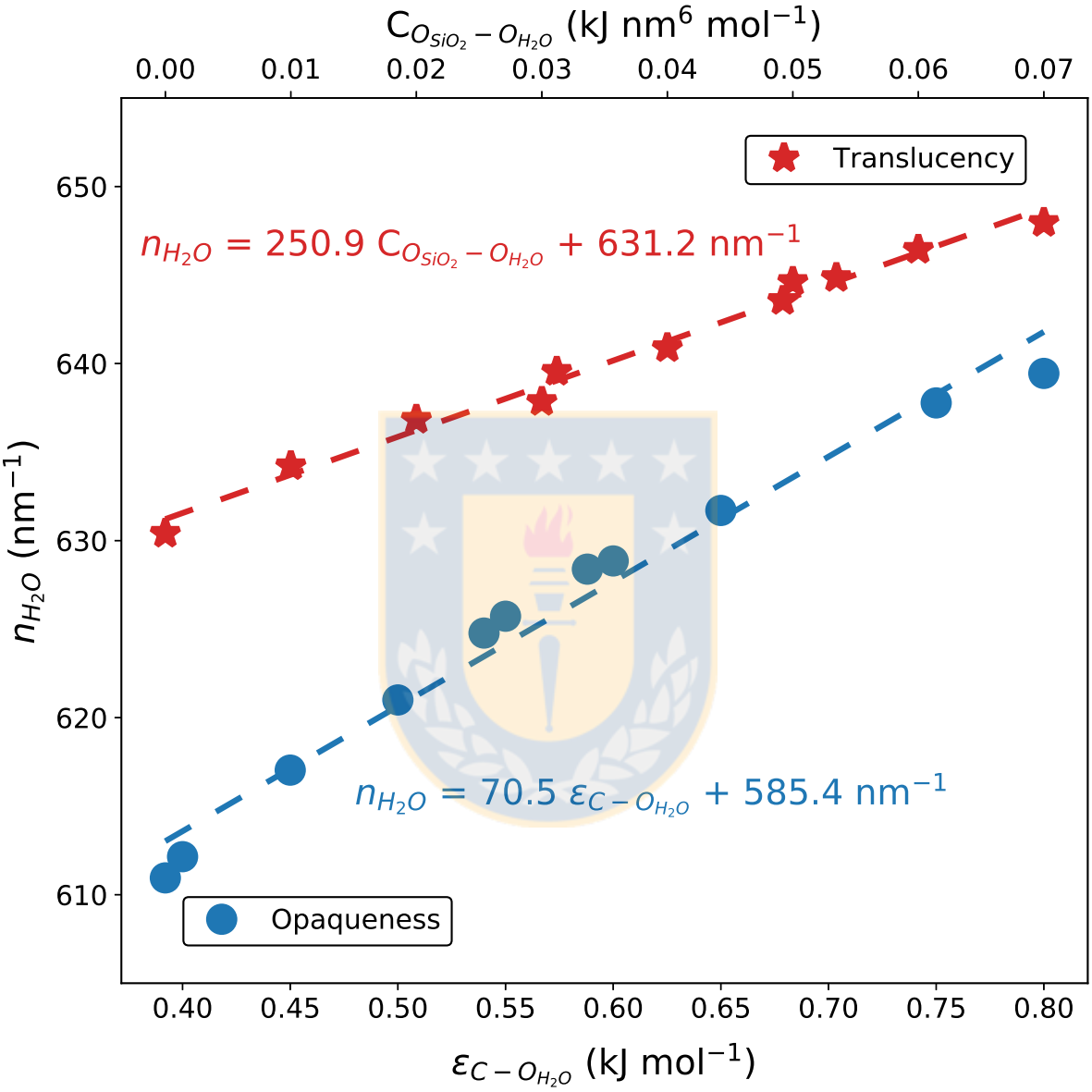

Figure 6.13: Calculated number of water molecules per CNT length required to fill the CNT coated silica pore with an internal pressure of 1 bar as a function of $\varepsilon_{C-O_{H_2O}}$ for the opaqueness cases, and as a function of $C_{O_{SiO_2}-O_{H_2O}}$ for the translucency cases. Source: Own elaboration.

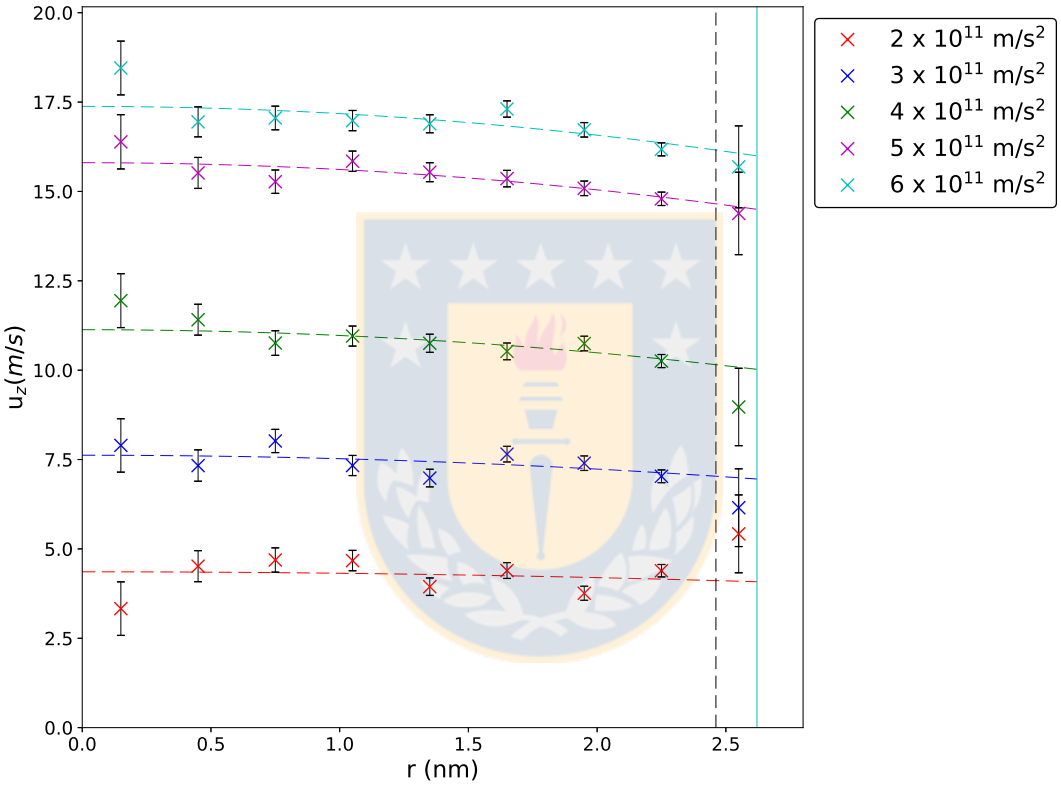

Figure 6.14: Calculated water velocity profiles inside the CNT coated silica pore, for the translucency case with a $C_{O_{SiO_2}-O_{H_2O}}$ of 0.035 kJ nm^6 mol^{-1}, under different applied external fields. Source: Own elaboration.

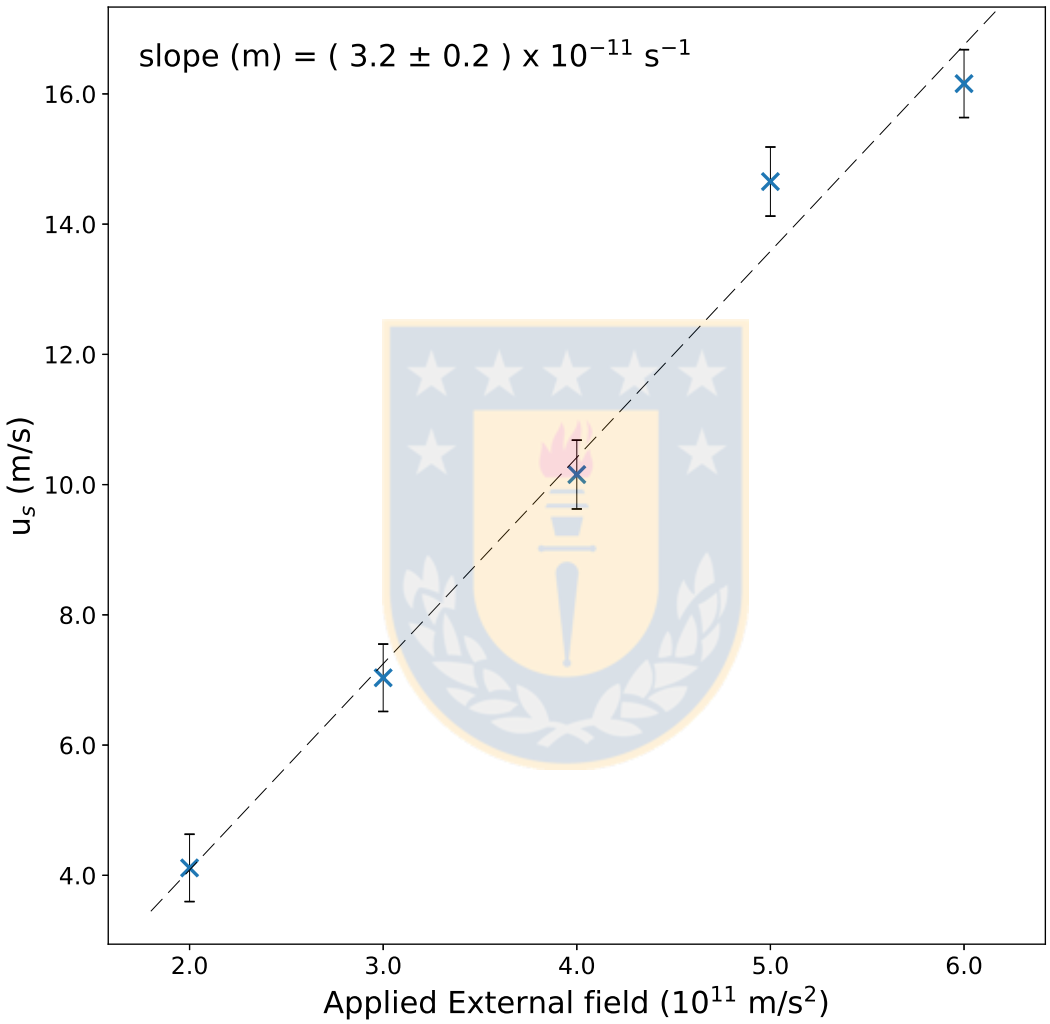

Figure 6.15: Calculated water slip velocities inside the CNT coated silica pore, for the translucency case with a $C_{O_{SiO_2}-O_{H_2O}}$ of 0.035 kJ nm^6 mol^{-1}. The dashed line represents the linear fit to u_s. The slope of the fit is employed to calculate l_s. Source: Own elaboration.

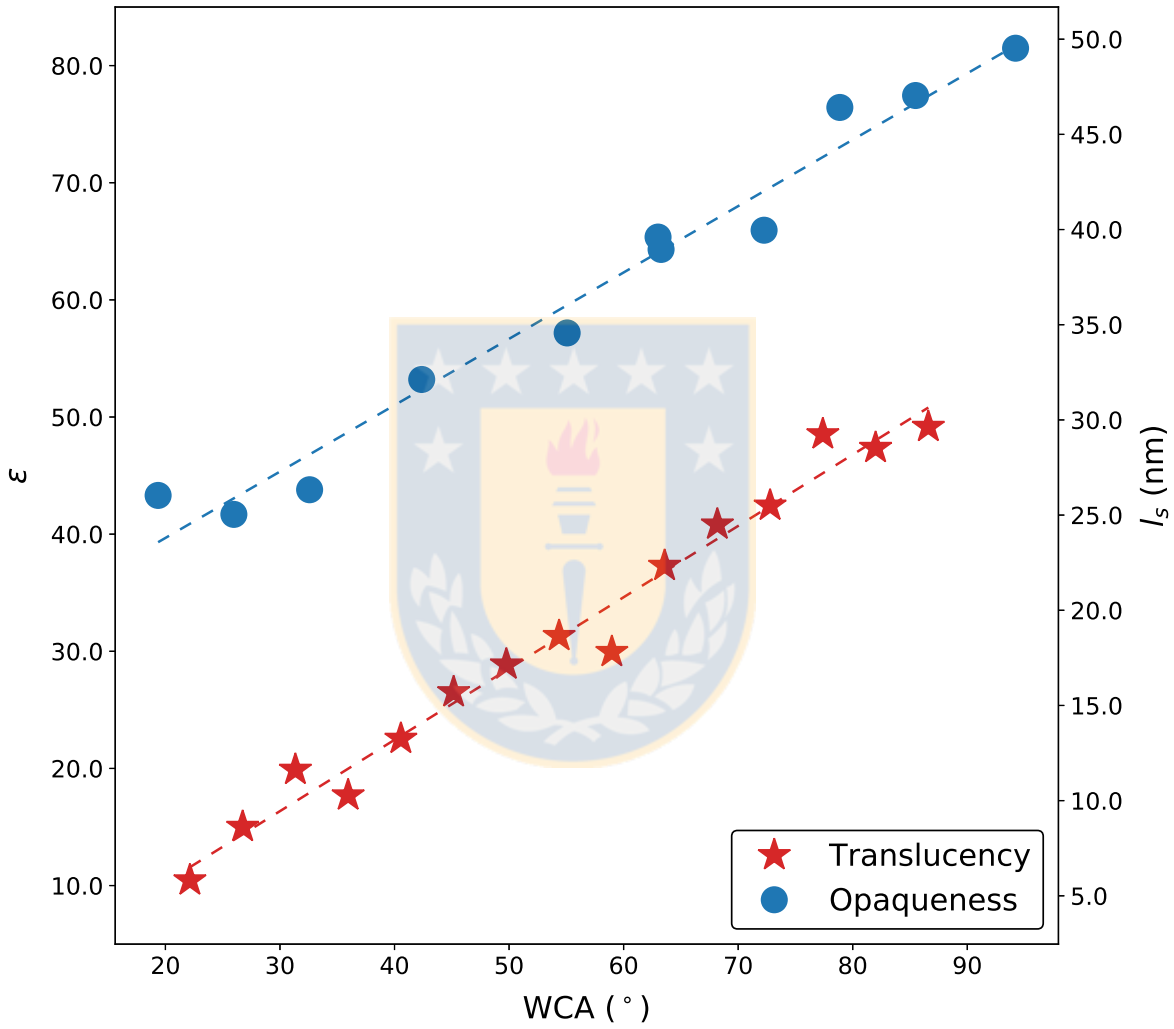

Figure 6.16: Calculated flow enhancement and slip lengths for all the studied cases of water flowing inside the CNT coated silica pore. The dashed lines represent a linear fit to them. An increasing ε and l_s are observed with increasing WCAs. Source: Own elaboration.

Chapter 7

Conclusions

In this thesis the molecular dynamics technique is employed to study the enhancement in nanoconfined transport of water, induced by the use of graphitic materials as wall coatings. A study of the flow of water at high shear rates, confined inside a pristine graphene channel, is conducted. Our results show that, at high flow rates, the crystallographic features of graphene can induce a difference of up to 10% in the flow rates of water, depending on the direction of the flow. This difference is linked to a directional variation of the momentum transfer between solid and fluid and an enhanced effect of the surface energy corrugation felt by the water molecules. Subsequently, we study the water flow enhancement in hydrophilic silica nano slits, induced by the use of monolayer graphene as coatings. Our model reproduces the wettability of graphene coated silica, reported by Rafiee et al.. [35] The simulations demonstrate that, despite a decrease in the available cross section of the channel, the graphene coatings still induce an important flow enhancement. Finally, we study the reduction of viscous losses, resultant of the use of single walled carbon nanotubes (SWCNT) as wall coatings in a cylindrical nanopore of amorphous silica. The atomistic model of a cylindrical silica pore, coated by a (39,39) SWCNT is successfully characterized. Furthermore, we study two possible scenarios, that reproduce phenomena observed in experiments for graphene coated substrates. In the first scenario the SWCNT is translucent to the wettability of silica therefore allowing the direct interaction between silica and water. In the second scenario the SWCNT is opaque to the interactions between underlying substrate and water, achieving the correct wettability of the coated pore by tuning the strength of the water-carbon interaction. The flow measured for both scenarios displays different slippage which is associated to the different surface energy corrugations reproduced by each surface interaction models, with water filling different surface energy barries. Furthermore, our results for both models indicate a dependence between wettability and slippage. Despite the different slip computed for both models, a significant flow enhancement is calculated therefore demonstrating that the use of SWCNT as coatings is a feasible alternative to reduce the viscous losses in fluidic nanoconduits.

Appendix A

Interaction potentials and models

A.1 SPC/E Water model

The SPC/E model [184] is used to describe the water molecules in the system. This model corresponds to a rigid model of water, with an $O-H$ bond length of $0.1\,nm$ and a $H-O-H$ angle of 109.47°. The constrained bonds and angle are treated by employing the SHAKE algorithm [229] The partial charges are: $q_O = -0.847e$ and $q_H = +0.4235e$. The interatomic interaction is described using a Lennard-Jones potential, that has the form:

$$U_{ij} = 4\epsilon \left[\left(\frac{\sigma}{r_{ij}} \right)^{12} - \left(\frac{\sigma}{r_{ij}} \right)^{6} \right] \tag{A.1}$$

with, $\sigma = 0.3166$ nm and $\epsilon = 0.650$ KJ mol^{-1}.

A.2 Carbon-carbon interactions

The interaction between carbon atoms inside a graphene sheet are described using Morse, harmonic angle and torsional potentials [150]. The bond and angle torsion terms are original obtained from ref [230] and successfully reproduce the structures of graphite and fullerene crystals. The torsion term is employed to maintain the structural properties in graphene sheets. [150] The potential has the form:

$$U(r_{ij}, \theta_{ijk}, \phi_{ijkl}) = K_{Cr}(\xi_{ij} - 1)^2 + \frac{1}{2} K_{C\theta}(cos\,\theta_{ijk} - cos\,\theta_C)^2 + \frac{1}{2} K_{C\phi}(1 - cos\,2\phi_{ijkl}) \tag{A.2}$$

where θ_{ijk} represents the bending angle, ϕ_{ijkl} is the torsion angle, r_{ij} is the distance between atoms (nm), $\xi_{ij} = e^{-\gamma(r_{ij} - r_c)}$. $K_{Cr} = 47890$ kJ Mol^{-1} nm^{-2}, $K_{C\phi} = 562.2$ kJ mol^{-1}, $r_C = 0.1418$ nm, $\theta_C = 120.0^{\circ}$ and $\gamma = 21.867$ nm^{-1}.

The non bonding interactions in graphene, fullerenes and carbon nanotubes are described using Lennard-Jones potentials, whose parameters are $\epsilon_{CC} = 0.4396\,$kJ mol^{-1} and $\sigma_{CC} = 0.3851\,$nm. [231]

A.3 Silica-silica interactions

The interactions between silica atoms are described using the TTAMm potential [216]. The TTAMm is a modification of the classical TTAM model developed by Tsuneyuki et al. [217] The partial charges for this potential are: $q_{Si} = +2.4e$ and $q_O = -1.2e$. The potential has the following form:

$$U_{ij} = \frac{q_i q_j}{4\pi\epsilon_0 r_{ij}^2} + \alpha_{ij} \exp\left(-r_i j \rho_{ij}\right) - \frac{C_{ij}}{r_{ij}^6} + 4\epsilon_{ij}\left[\left(\frac{\sigma_{ij}}{r_{ij}}\right)^{18} - \left(\frac{\sigma_{ij}}{r_{ij}}\right)^{6}\right] \tag{A.3}$$

with the following parameters:

Table A.1: Silica interaction parameters. Source: Own elaboration.

Pair	ϵ_{ij} (kJ mol^{-1})	σ_{ij} (nm)	C_{ij} (kJ nm^6 mol-1)	α_{ij} (kJ mol^{-1})	ρ_{ij} (nm^{-1})
Si-Si	1.277×10^3	0.040	2.240×10^{-3}	8.417×10^{10}	1.522×10^2
Si-O	1.083	0.130	6.82510×10^{-3}	1.0347×10^6	0.480×10^2
O-O	4.60×10^{-2}	0.220	2.07×10^{-2}	1.696×10^5	0.283×10^2

A.4 Water-carbon interactions

The water-carbon interactions are described using the potential calibrated by Werder et al. [80] which reproduce a macroscopic WCA of 86°. This potential corresponds to a Lennard-Jones potential, with $\sigma = 0.319\ nm$ and $\epsilon = 0.392\ kJ/mol$

A.5 Carbon-silica interactions

The carbon-silica interactions are described employing a Lennard Jones potential with parameters from Zhang and Li [219] which reproduces the proper substrate-regulated morphology of GE. The parameters for this potential are summarized in the following table:

Table A.2: Graphene-Silica interaction parameters. Source: Own elaboration.

Pair	ϵ_{ij} (kJ mol^{-1})	σ_{ij} (nm)
C-Si	0.20551	0.1506
C-O_{SiO_2}	0.48145	0.2256

Appendix B

Appendix for: Water flow in graphene nanochannels: Slip divergence and the role of chirality (Chapter 4)

B.1 Temperature profiles

The fluid temperature profiles for the cases with an armchair direction and 2.8 nm channel height are presented in Figure B.1. For the cases with lower applied fields, a constant temperature around 296 K is calculated in the bulk zone (below $4 \cdot 10^{11}$ m/s^2). As divergence is attained (around $6 \cdot 10^{11}$ m/s^2) the temperature increases, indicating a decrease in the momentum transfer between fluid and wall. The temperature profiles display a non-newtonian behavior at the interface. When compared to the density profiles the temperature peaks seem to coincide with the depletion layer. Note that the temperature increase affects the whole channel cross section as shown in the temperature profile. When normalizing the temperature profiles to the bulk temperature no difference is found between cases, as shown in Figure B.2.

To ensure that the obtained velocity increase is not related to a decrease in the fluid viscosity due to the temperature increase, we coupled the thermostat to both graphene and water for cases with higher applied filed where divergence is obtained. A clear difference in the temperature is observed when comparing cases where the thermostat is couplet to water and graphene to the cases where only the carbon atoms of the graphene sheets are coupled to the thermostat (Figure B.3). When comparing the flow velocity (mean velocity) no significant difference is observed for both cases. Indeed, for the case where only the graphene atoms are coupled to the thermostat a mean velocity of 179 m/s is computed and for the case where both water molecules and graphene atoms are coupled to the thermostat, a mean velocity of 183 m/s ($\sim$ 2 % difference). The same behavior is observed in other cases, where a different acceleration is applied ($8 \cdot 10^{11}$ m/s^2 and $12 \cdot 10^{11}$ m/s^2). When comparing cases where GE and water atoms are coupled to the thermostat and the same force is applied in different direction, a difference between the flow velocities is computed ($\sim$ 10 % difference between AC an ZZ), which is similar to the difference calculated for the cases where only the carbon atoms of the graphene sheets are coupled to the thermostat.

Figure B.4A shows a comparison of the temperature profiles for the AC and ZZ cases when

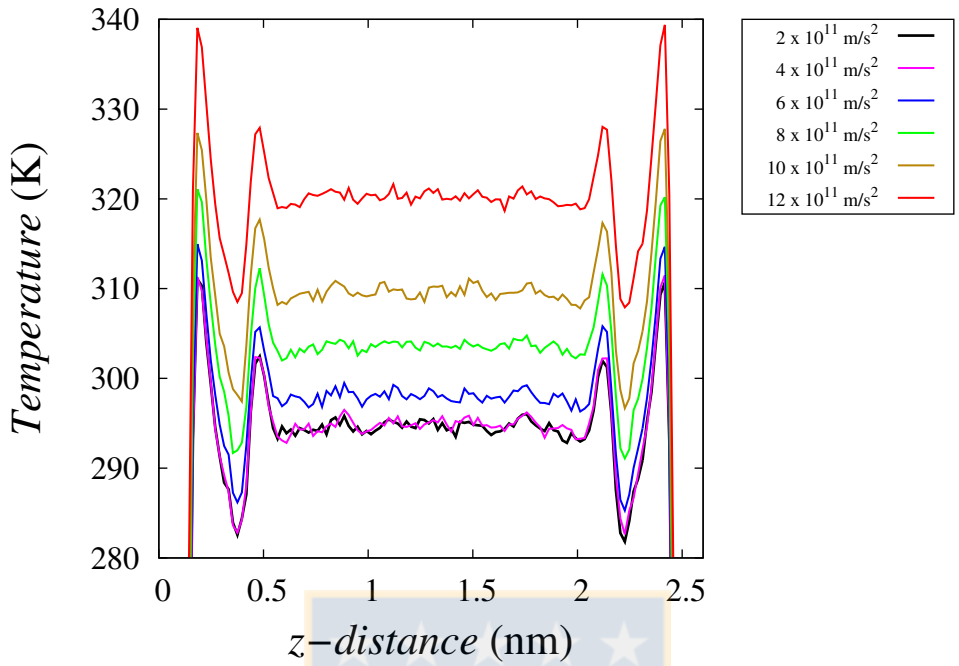

Figure B.1: Temperature profiles for the different applied external force for the 2.8 nm armchair case. The wall temperature was maintained constant at 300 K by coupling its atoms to a Berendsen thermostat. Source: Own elaboration.

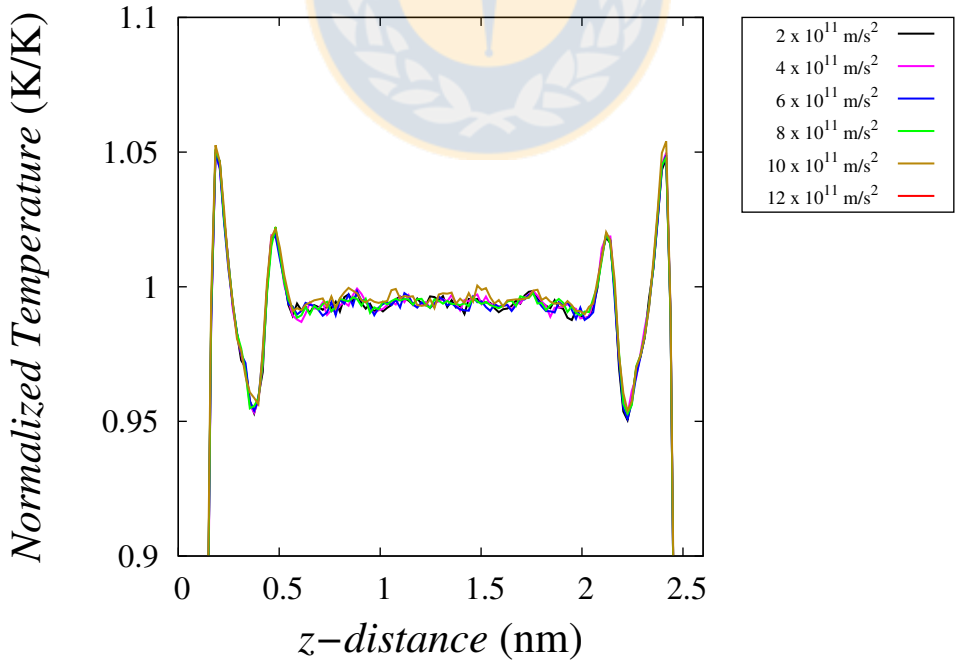

Figure B.2: Normalized temperature profiles for the different applied external force for the 2.8 nm armchair case. Source: Own elaboration.

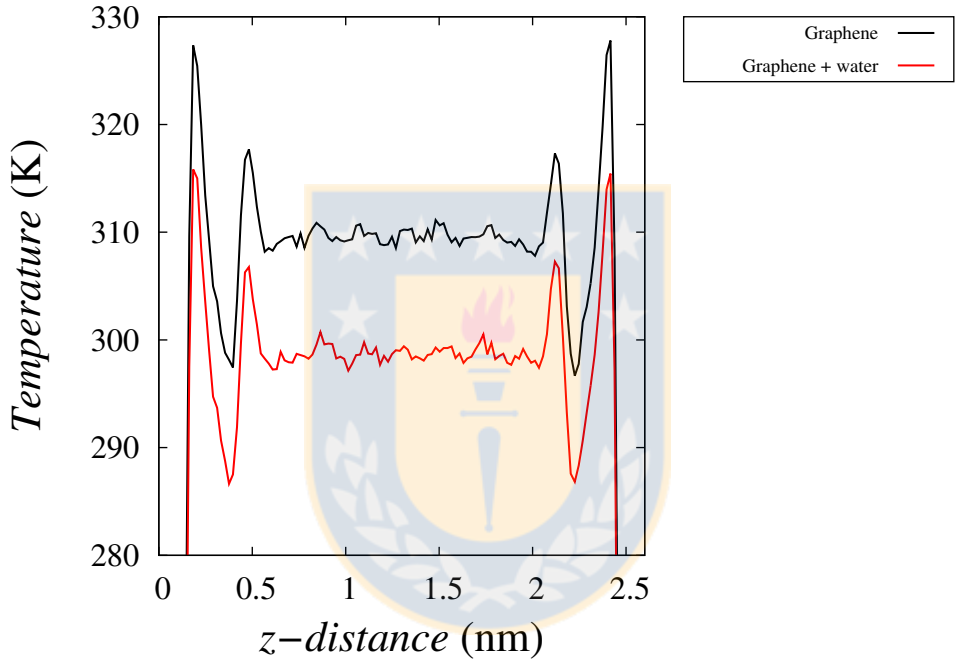

Figure B.3: Temperature profiles for the cases with $10 \cdot 10^{11}$ m/s^2 applied external force in armchair and zigzag channels with height of 2.8 nm. The thermostat was coupled to the graphene atoms (black line) and to graphene atoms and water molecules (red line). Source: Own elaboration.

slip length divergence is reached. In particular, we observe that the temperature for the cases are higher than the ones observed for the ZZ case. It can be better appreciated when a zoom is made to the bulk zone (Figure B.4B). This temperature difference can be related to a change in the wall-fluid momentum transfer. A lower momentum transfer between wall-fluid would result in a lower friction and thus greater flow velocities.

B.2 Shear rate

Figure B.5 shows the calculated shear rate as a function of the shear stress. The shear rate shows a linear dependence to the shear stress, demonstrating that the bulk fluid remains Newtonian.

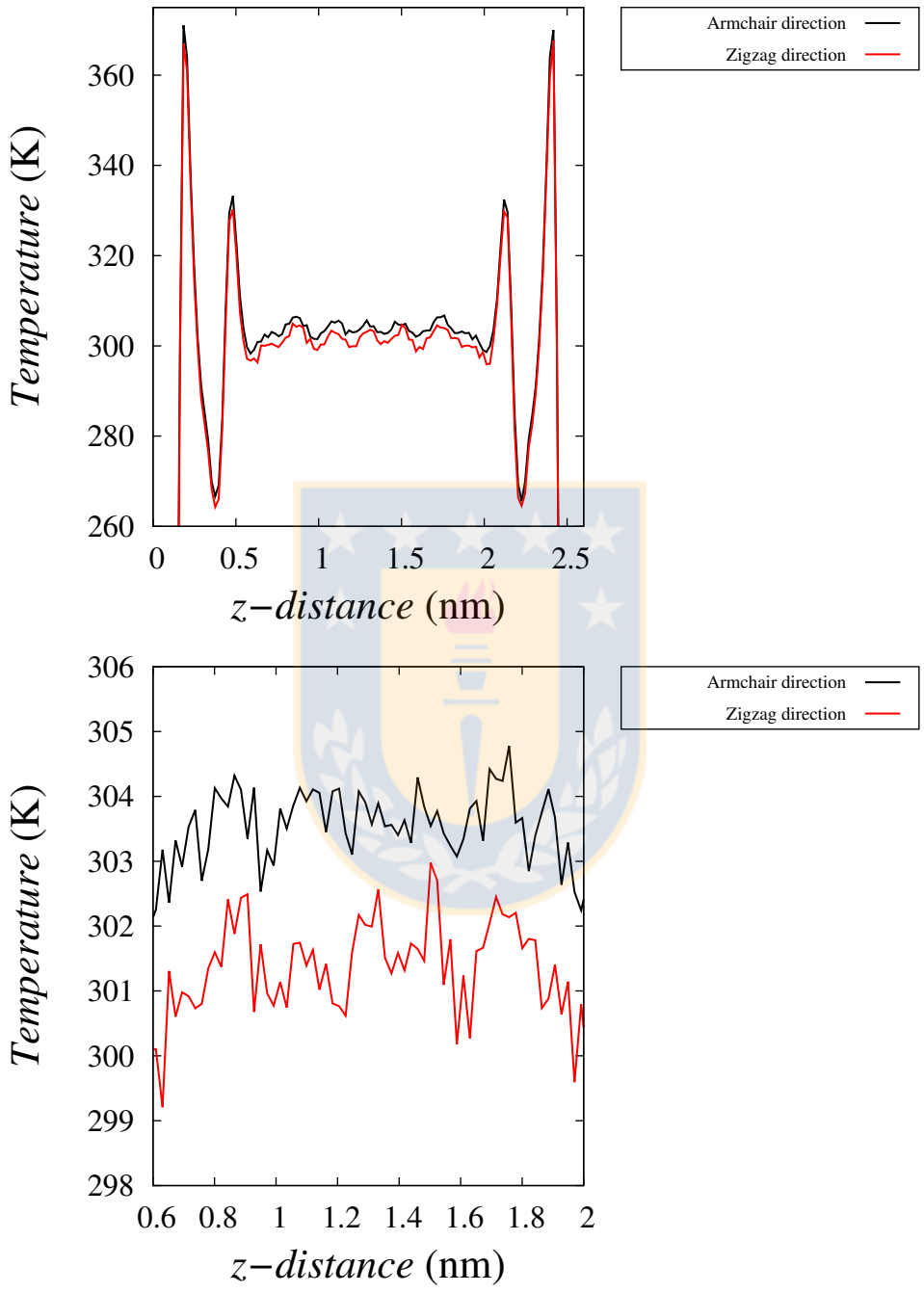

Figure B.4: A) Temperature profiles for the $8 \cdot 10^{11}\,\mathrm{m/s^2}$ applied external force for the 2.8 nm armchair and zigzag cases. The thermostat was coupled to the graphene atoms B) Zoom to the bulk zone of the same cases. Source: Own elaboration.

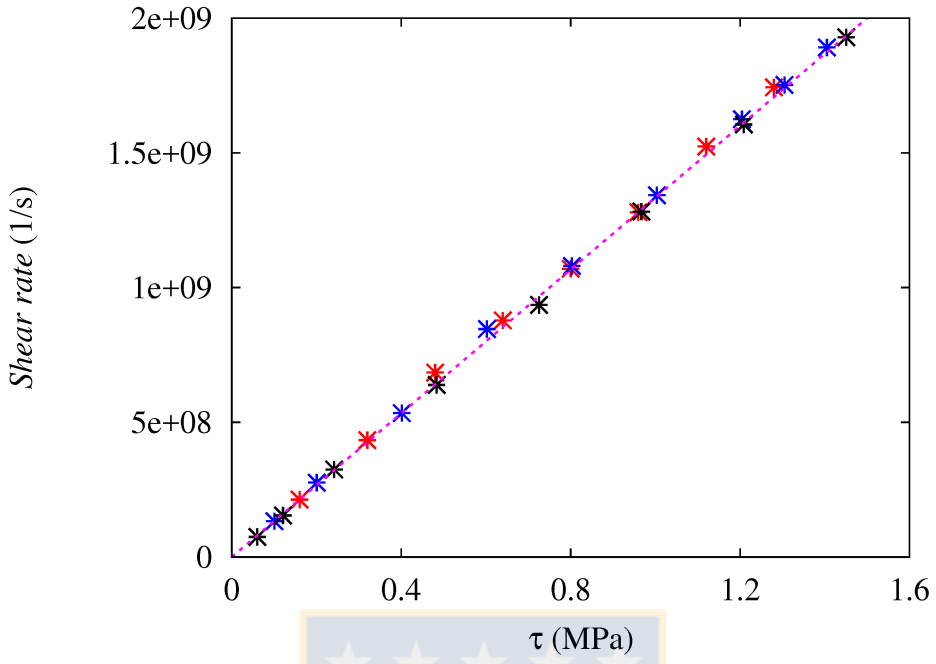

Figure B.5: Shear rate as a function of the shear stress. Source: Own elaboration.

Appendix C

Appendix for: Monolayer graphene-based coating to induce water flow enhancement in silica nanochannels (Chapter 5)

C.1 Silica slab amorphization

The silica slabs are created by replicating a β crystoballite unit cell and then applying a thermal annealing to the crystallline silica. The initial slab dimensions are; 4.424 nm x 10.744 nm x 2.528 nm. Each slab is composed of 3808 Si atoms and 7616 O atoms. The simulation box dimensions are 4.666476 nm x 11.0604 nm x 15 nm. Boundary condition are applied on the x and y direction, while free space is given in the z direction, large enough to avoid interaction between surfaces. Therefore, the resultant surfaces are annealed. The atoms of each slab interact with each other, but not with the atoms of the other slab. A timestep of 1 fs is used. The Si and O atoms are connected to a Berendsen thermostat, with a coupling constant of 0.005 ps. The silica is first heated to 3000 K for 10 ps, then the system is quenched to 300 K using a cooling rate of 70 K/ps. After the target temperature is reached the system is given more time to equilibrate (the total simulation time is 100 ps).

C.2 Solvent Accessible Surface Area

Solvent Accessible Surface Area (SASA) fwas calculated for each surface using the SASA command provided in VMD. [227] An expanded atom radius of 2 Å was used for this purpose. The SASA was for the atoms with position within 3 Åand 43 Åalong the x axis and within positions between 3 Åand 100 Å, along the y axis. This section of the slab has a projected area in the xy plane of 3880 Å^2. As a reference the SASA of a flat pristine graphene sheet was also measured. The following SASAs were obtained; 4159 Å^2 for the pristine graphene, 4288 Å^2 for the graphene on top of a silica slab and 5521 Å^2 for the silica surface. The resulting SASA per projected area for each case is 1.072 for the pristine graphene sheet, 1.105 for the graphene layer on top of the silica surface and 1.422 for the silica surface.

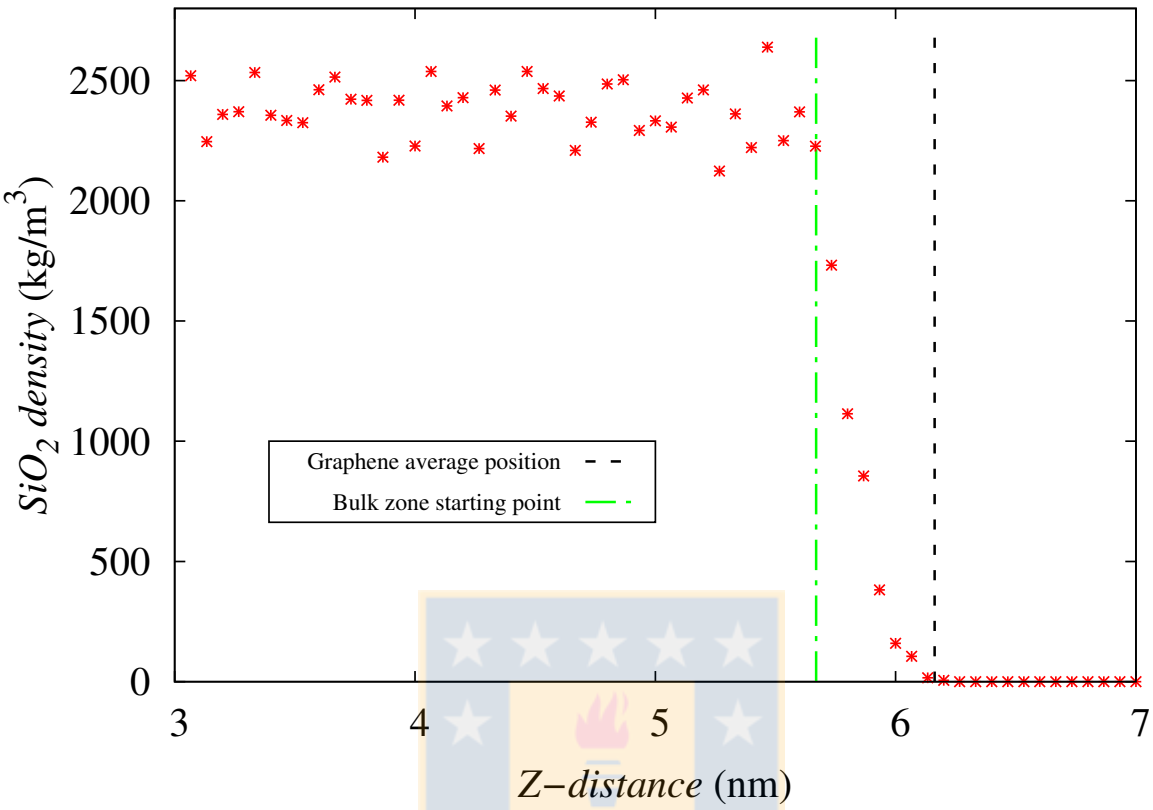

Figure C.1: Schematic representation of the contact distance separation calculation in the studied graphene coated silica channels cases. Source: Own elaboration.

C.3 Contact distance

Contact distance is estimated as the distance from the average graphene sheet position to the point on which the silica density profile displays bulk behaviour, as seen on Figure C.1.

C.4 Water contact angle measurement

Equilibrium molecular dynamics simulations were conducted to compute the WCA. In particular, WCA of a periodic cylindrical water droplet on top was measured on coated and uncoated amorphous silica substrates. The amorphous silica slab is created following the protocols described in Zambrano et al. [218]. The simulation box and substrate dimensions were chosen to minimize graphene strain, and correspond to 44.2416 nm in the x direction and 4.66654 nm in the y direction. For the coated cases, a graphene sheet periodic along the x and y direction is released 0.5 nm away from the slab surface and is allowed to equilibrate. Carbon atoms are coupled to the thermostat, while the silica atoms are kept fixed. Measured C-C bond mean distance correspond to 0.1423 nm, representing a stretch of 0.34%. After 1 ns of simulation the carbon atoms are frozen. A periodic cylindrical water droplet of 3600 molecules is previously equilibrated by coupling its molecules to the thermostat. During this step the droplet does not interact with the substrate. Then, the droplet is released 0.5 nm away from the substrate surface.

The water molecules are connected to the thermostat during the first 0.5 ns of simulation, then the system is equilibtrated for another 0.5ns in the NVE ensamble. Data is collected every 0.1 ps during 1 ns of simulation. Density distribution is obtained by a binning sampling method, on which the simulation box is divided along the x and z directions. Density is obtained by averaging the mass on each bin over time and dividing it by the bin volume. WCA is obtained from a circle fit to the $650 kg/m^3$ isochore [151]. The near wall layering zone is not considered in the circle fit (Near wall exclusion zone). The water contact angle is measured on the graphene surface, following the method described by Werder et al. [80].

C.5 Channel filling

An internal pressure of 1 bar is achieved by using the bottom slab as a piston, while the top one is kept fixed. To this end an acceleration of 0.000135888 nm/ps^2 in the positive z direction is imposed to all the Si and O atoms of the bottom slab. The water molecules are coupled to the thermostat to attain a temperature of 300 K during all the simulation. After steady state, which is ensured by checking the botom silica slab position, the atoms in the outermost region of 0.4 nm width, measured from the external surface of each wall, is maintained fixed, while the rest of the silica atoms (in both slabs) are maintain active and coupled to the thermostat at 300K. The number of water molecules for each studied channel height are: 3437 for the 2.4nm channel, 5156 for 3.4 nm and 6800 for 4.4 nm.

C.6 Temperature profile

The temperature profile for the case with height of 3.4 nm and an applied external field of $9.324 \cdot 10^{11} m/s^2$ is presented of Figure C.2.

C.7 Binning sampling method

The used binning sampling method divides the simulation box in the z dimension (for the velocity and density profile calculation) in bins of $0.113333\,nm$ height. Velocity profiles are computed by dividing the sum of all particle's momentum over time, per bin, by the sum of the total mass in each bin over time. This can be summarized by the formula:

$$u_k = \frac{\sum_i^{n_k} m_i v_i}{\sum_i^{n_k} m_i}$$

density profiles al computed by dividing the sum of all mass per bin over time by the number of time steps averaged and the bin's volume;

$$\rho_k = \frac{\sum_i^{n_k} m_i}{N \cdot V_k}$$

In the WCA cases the box is divided along the x and z direction, with a bin size of $0.113333\,nm$ for both directions.

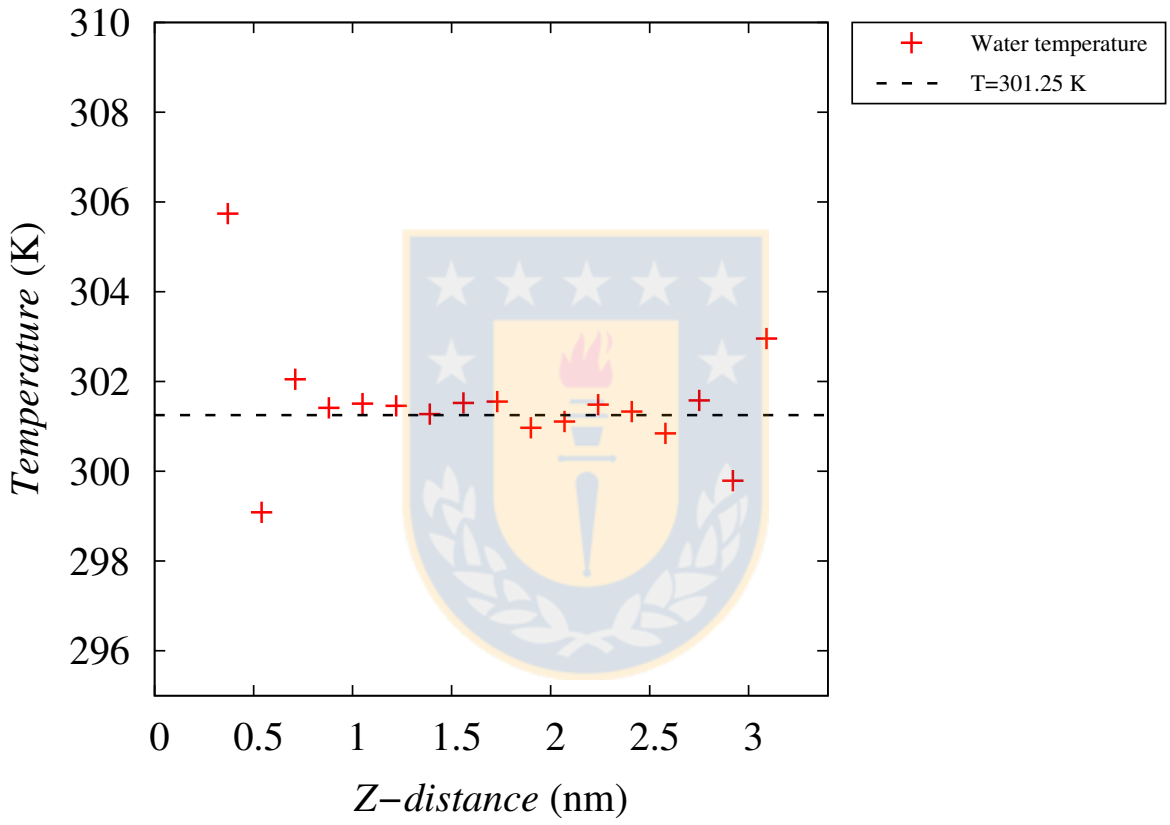

Figure C.2: Temperature profile for the graphene coated silica channel case with a height of 3.4 nm, with an applied external field of $9.324 \cdot 10^{11} m/s^2$. Source: Own elaboration.

Appendix D

Appendix for: Reduction of viscous losses in silica nanopores induced by carbon nanotube coatings (Chapter 6).

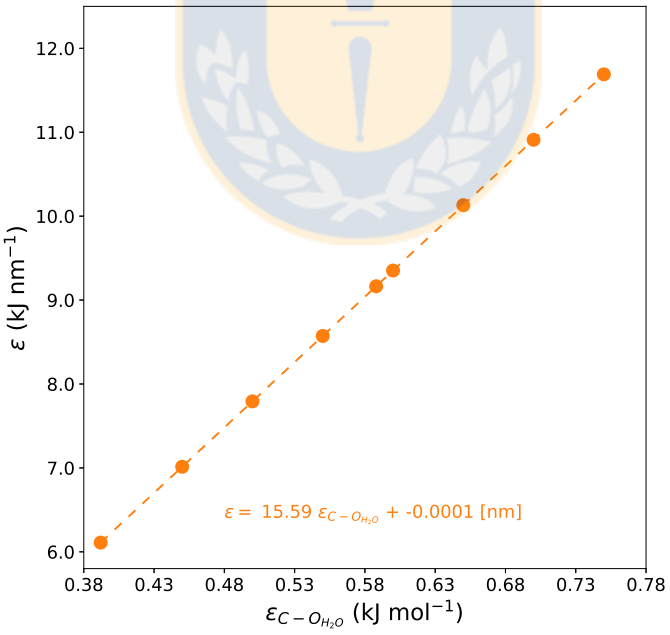

Figure D.1: Calculated ϵ of the fit to the Mie potential, for the opaqueness cases. The dashed line represents a linear fit to ϵ. Source: Own elaboration.

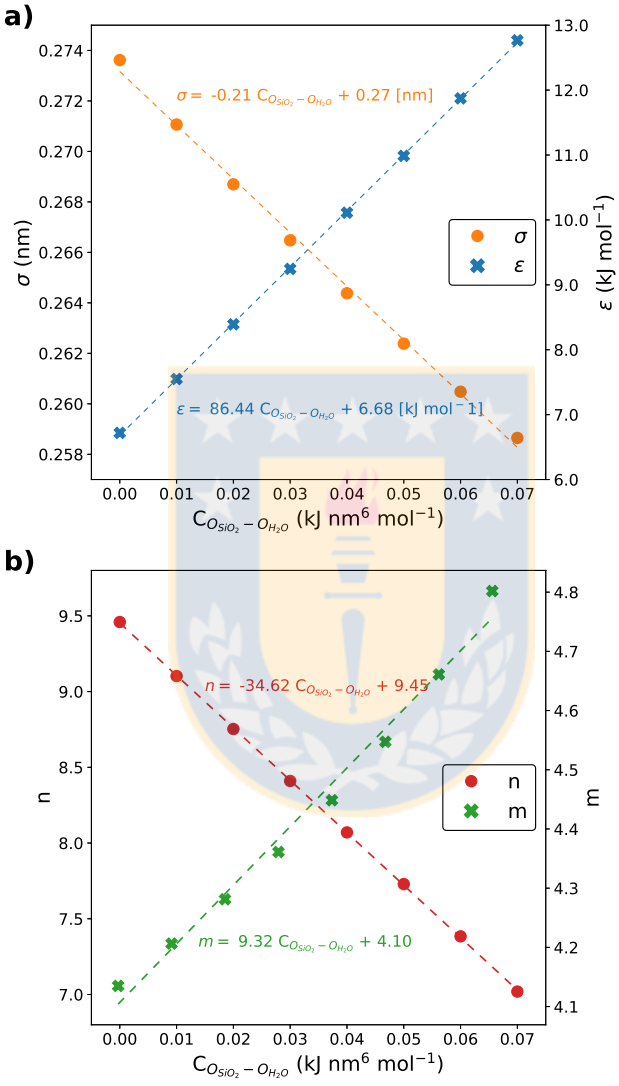

Figure D.2: Calculated parameters of the fit to the Mie potential, for the translucency cases. a) ϵ and σ. b) n and m. The dashed lines represent a linear fit to the parameters. Source: Own elaboration.

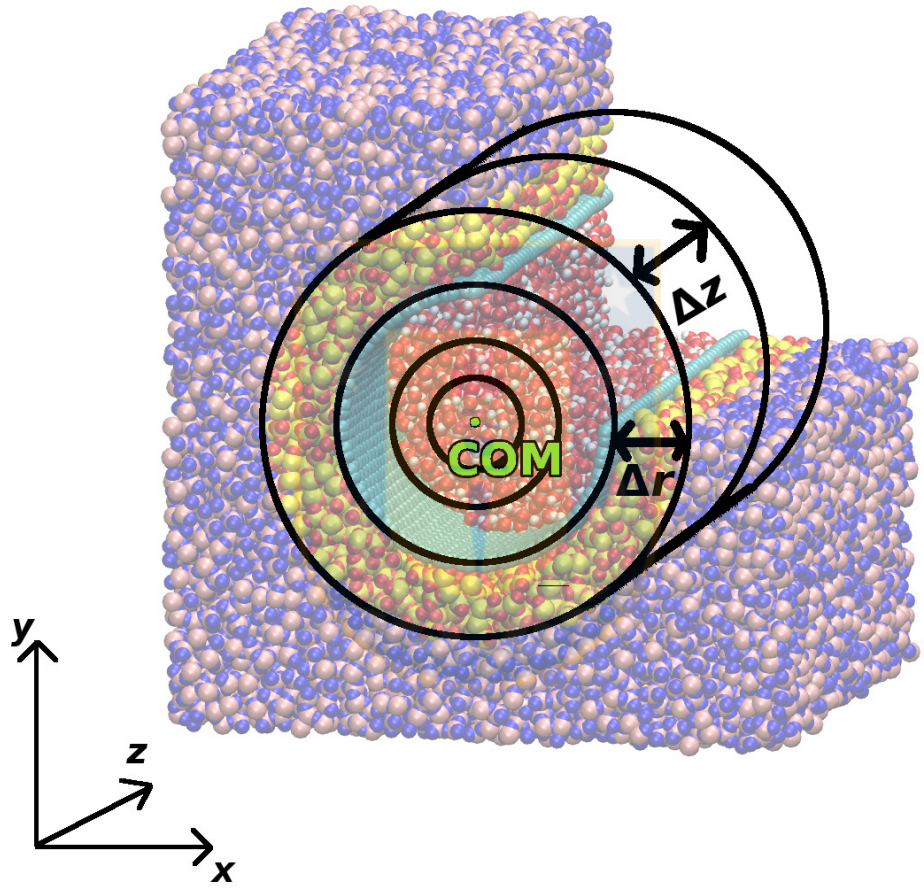

Figure D.3: Schematic representation of the employed binning sampling method to measure the WCA of a droplet inside the coated pore. Source: Own elaboration.

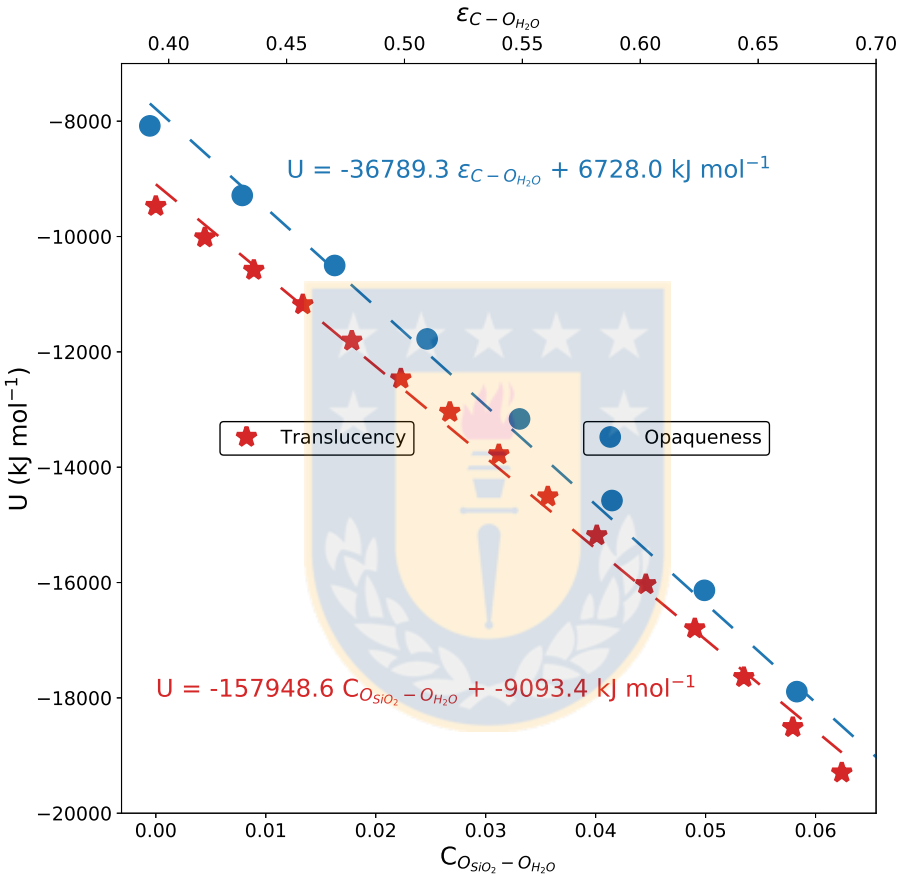

Figure D.4: Computed potential energy between the water droplet and coated pore in the WCA simulations, as a function of the tuned parameters. The dashed lines represent a linear fit to the potential energy. Source: Own elaboration.

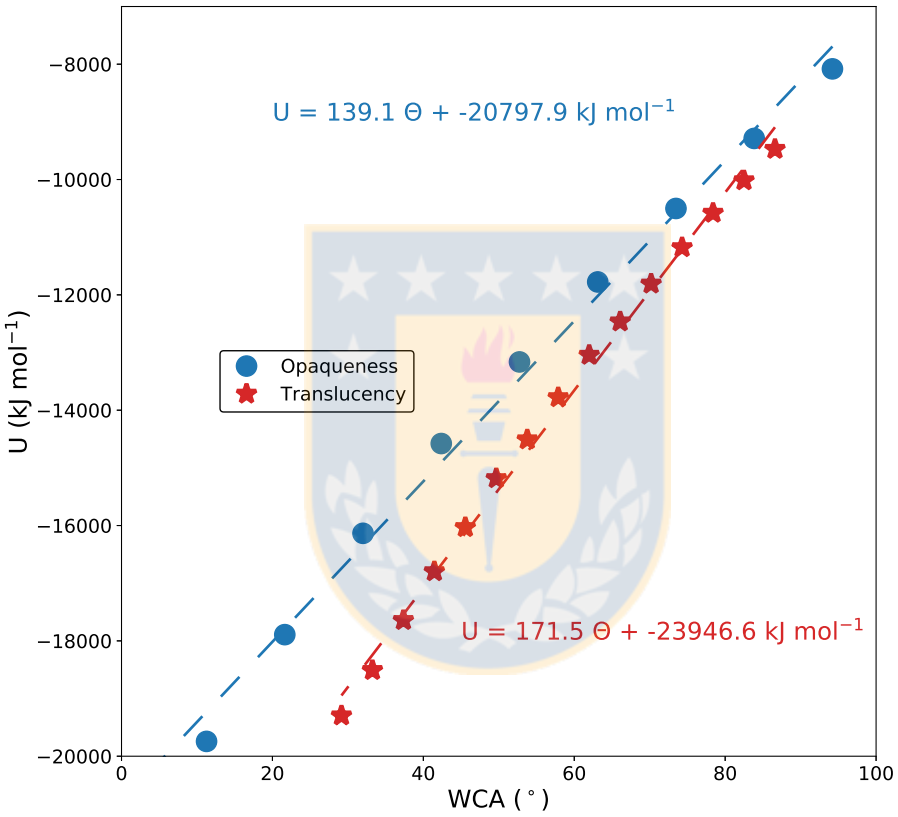

Figure D.5: Computed potential energy between the water droplet and coated pore in the WCA simulations as a function of WCA. The dashed lines represent a linear fit to the potential energy. Source: Own elaboration.

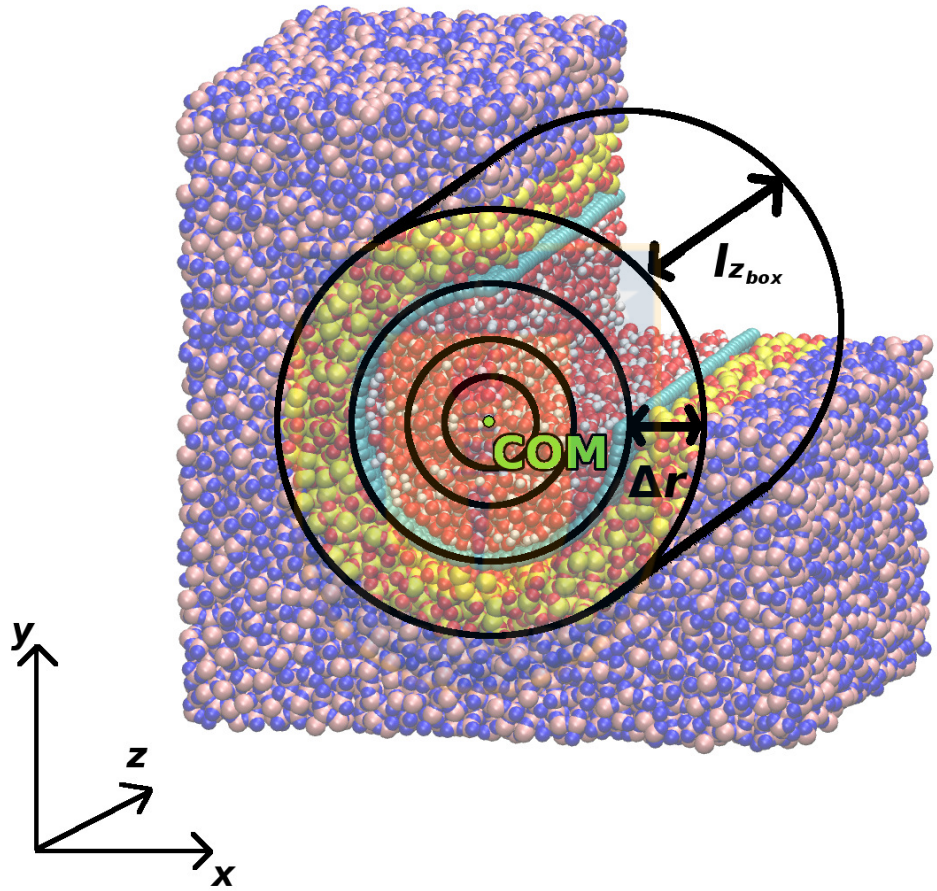

Figure D.6: Schematic representation of the employed binning sampling method to measure the hydrodynamic properties of water confined inside the pore. Source: Own elaboration.

Publications and Conferences

First author publications

1. Enrique Wagemann, Elton Oyarzua, Jens H. Walther, and Harvey A. Zambrano. "Slip divergence of water flow in graphene nanochannels: the role of chirality." *Phys. Chem. Chem. Phys.* 19(13):8646-8652, 2017.

Co-author publications

1. Harvey A. Zambrano, Nicolás Vásquez, and Enrique Wagemann. "Wall embedded electrodes to modify electroosmotic flow in silica nanoslits." *Phys. Chem. Chem. Phys.* 18(2):1202-1211, 2016.

2. Nabin Kumar Karna, Ándres Rojano Crisson, Enrique Wagemann, Jens H. Walther, and Harvey A. Zambrano. "Effect of an external electric field on capillary filling of water in hydrophilic silica nanochannels." *Phys. Chem. Chem. Phys.* 20(27):18262-18270, 2018.

Conferences

1. Harvey A. Zambrano, Enrique Wagemann, Elton Oyarzua, and Jens H. Walther. Flow enhancement of water flow through silica slit pores with graphene-coated walls. In 68th Annual Meeting of The American Physical Society – DFD, Boston, Massachusetts USA. 2015.

2. Enrique Wagemann, Elton Oyarzua, Jens H. Walther, and Harvey A. Zambrano. Water transport in graphene nano-channels. In 68th Annual Meeting of The American Physical Society – DFD, Boston, Massachusetts USA. 2015.

3. Enrique Wagemann, Jens H. Walther, and Harvey A. Zambrano. Carbon nanotube-based coatings to induce flow enhancement in hydrophilic nanopores. In 69th Annual Meeting of The American Physical Society – DFD, Portland, Oregon USA. 2016.

4. Enrique Wagemann, Jens H. Walther, and Harvey A. Zambrano. Drag reduction in silica nanochannels induced by graphitic wall coatings. In 70th Annual Meeting of The American Physical Society – DFD, Denver, Colorado USA. 2017.

Bibliography

[1] X. Wan, Y. Huang, and Y. Chen, "Focusing on energy and optoelectronic applications: a journey for graphene and graphene oxide at large scale," *Accounts of chemical research*, vol. 45, no. 4, pp. 598–607, 2012.

[2] E. T. Thostenson, Z. Ren, and T.-W. Chou, "Advances in the science and technology of carbon nanotubes and their composites: a review," *Composites science and technology*, vol. 61, no. 13, pp. 1899–1912, 2001.

[3] M. P. Allen and D. J. Tildesley, *Computer simulation of liquids*. Oxford university press, 2002.

[4] A. Hinchliffe, *Molecular modelling for beginners*. John Wiley & Sons, 2005.

[5] D. Frenkel and B. Smit, *Understanding molecular simulation: from algorithms to applications*, vol. 1. Elsevier, 2001.

[6] P. Abgrall and N.-T. Nguyen, *Nanofluidics*. Artech House, 2009.

[7] A. T. Conlisk, "Essentials of micro-and nanofluidics," *Mechanical Engineering*, vol. 2014, p. 15, 2013.

[8] B. D. Gates, Q. Xu, M. Stewart, D. Ryan, C. G. Willson, and G. M. Whitesides, "New approaches to nanofabrication: molding, printing, and other techniques," *Chemical Reviews.*, vol. 105, no. 4, pp. 1171–1196, 2005.

[9] S. Prakash, A. Piruska, E. N. Gatimu, P. W. Bohn, J. V. Sweedler, and M. A. Shannon, "Nanofluidics: systems and applications," *IEEE Sensors Journal*, vol. 8, no. 5, pp. 441–450, 2008.

[10] S. Gravelle, L. Joly, F. Detcheverry, C. Ybert, C. Cottin-Bizonne, and L. Bocquet, "Optimizing water permeability through the hourglass shape of aquaporins," *Proceedings of the National Academy of Sciences*, p. 201306447, 2013.

[11] J. Lee, T. Laoui, and R. Karnik, "Nanofluidic transport governed by the liquid/vapour interface," *Nature Nanotechnol.*, vol. 9, no. 4, pp. 1–7, 2014.

[12] L. Bocquet, D. Quéré, T. A. Witten, and L. F. Cugliandolo, *Soft Interfaces: Lecture Notes of the Les Houches Summer School: Volume 98, July 2012*, vol. 98. Oxford University Press, 2017.

[13] S. Joseph and N. Aluru, "Why are carbon nanotubes fast transporters of water?," *Nano Lett.*, vol. 8, no. 2, pp. 452–458, 2008.

[14] G. Tocci, L. Joly, and A. Michaelides, "Friction of water on graphene and hexagonal boron nitride from ab initio methods: very different slippage despite very similar interface structures," *Nano Lett.*, vol. 14, no. 12, pp. 6872–6877, 2014.

[15] P. A. Thompson and M. O. Robbins, "To slip or not to slip?," *Physics World*, vol. 3, no. 11, p. 35, 1990.

[16] P. A. Thompson and S. M. Troian, "A general boundary condition for liquid flow at solid surfaces," *Nature*, vol. 389, no. 6649, pp. 360–362, 1997.

[17] D. M. Huang, C. Sendner, D. Horinek, R. R. Netz, and L. Bocquet, "Water slippage versus contact angle: a quasiuniversal relationship," *Phys. Rev. Lett.*, vol. 101, no. 22, p. 226101, 2008.

[18] S. K. Kannam, B. Todd, J. S. Hansen, and P. J. Daivis, "How fast does water flow in carbon nanotubes?," *J. Chem. Phys.*, vol. 138, no. 9, p. 094701, 2013.

[19] S. K. Kannam, B. Todd, J. S. Hansen, and P. J. Daivis, "Slip length of water on graphene: Limitations of non-equilibrium molecular dynamics simulations," *J. Chem. Phys.*, vol. 136, no. 2, p. 024705, 2012.

[20] K. Falk, F. Sedlmeier, L. Joly, R. R. Netz, and L. Bocquet, "Molecular origin of fast water transport in carbon nanotube membranes: superlubricity versus curvature dependent friction," *Nano Lett.*, vol. 10, no. 10, pp. 4067–4073, 2010.

[21] E. Secchi, S. Marbach, A. Niguès, D. Stein, A. Siria, and L. Bocquet, "Massive radius-dependent flow slippage in carbon nanotubes," *Nature*, vol. 537, no. 7619, pp. 210–213, 2016.

[22] B. Liu, R. Wu, J. A. Baimova, H. Wu, A. W.-K. Law, S. V. Dmitriev, and K. Zhou, "Molecular dynamics study of pressure-driven water transport through graphene bilayers," *Phys. Chem. Chem. Phys.*, vol. 18, no. 3, pp. 1886–1896, 2016.

[23] E. Wagemann, E. Oyarzua, J. H. Walther, and H. A. Zambrano, "Slip divergence of water flow in graphene nanochannels: the role of chirality," *Phys. Chem. Chem. Phys.*, vol. 19, no. 13, pp. 8646–8652, 2017.

[24] J. H. Walther, K. Ritos, E. R. Cruz-Chu, C. M. Megaridis, and P. Koumoutsakos, "Barrier to superfast water transport in carbon nanotube membranes," *Nano Lett.*, vol. 13, no. 5, pp. 1910–1914, 2013.

[25] M. Whitby and N. Quirke, "Fluid flow in carbon nanotubes and nanopipes," *Nature Nanotechnol.*, vol. 2, pp. 87–94, 2007.

[26] M. Whitby, L. Cagnon, M. Thanou, and N. Quirke, "Enhanced fluid flow through nanoscale carbon pipes," *Nano Lett.*, vol. 8, no. 9, pp. 2632–2637, 2008.

[27] M. Majumder, N. Chopra, R. Andrews, and B. J. Hinds, "Nanoscale hydrodynamics: enhanced flow in carbon nanotubes," *Nature*, vol. 438, no. 7064, pp. 44–44, 2005.

[28] J. A. Thomas and A. J. McGaughey, "Reassessing fast water transport through carbon nanotubes," *Nano Lett.*, vol. 8, no. 9, pp. 2788–2793, 2008.

[29] J. A. Thomas, A. J. McGaughey, and O. Kuter-Arnebeck, "Pressure-driven water flow through carbon nanotubes: Insights from molecular dynamics simulation," *Internat. J. Thermal Sci.*, vol. 49, no. 2, pp. 281–289, 2010.

[30] R. Das, M. E. Ali, S. B. A. Hamid, S. Ramakrishna, and Z. Z. Chowdhury, "Carbon nanotube membranes for water purification: a bright future in water desalination," *Desalination*, vol. 336, pp. 97–109, 2014.

[31] K. B. Mogensen, L. Gangloff, P. Boggild, K. Teo, W. Milne, and J. P. Kutter, "Carbon nanotubes integrated in electrically insulated channels for lab-on-a-chip applications," *Nanotechnol.*, vol. 20, no. 9, p. 095503, 2009.

[32] S. P. Koenig, L. Wang, J. Pellegrino, and J. S. Bunch, "Selective molecular sieving through porous graphene," *Nature Nanotechnol.*, vol. 7, no. 11, p. 728, 2012.

[33] Z. Li, Y. Wang, A. Kozbial, G. Shenoy, F. Zhou, R. McGinley, P. Ireland, B. Morganstein, A. Kunkel, S. P. Surwade, *et al.*, "Effect of airborne contaminants on the wettability of supported graphene and graphite," *Nature Mat.*

[34] Y. Wei and C. Q. Jia, "Intrinsic wettability of graphitic carbon," *Carbon*, vol. 87, pp. 10–17, 2015.

[35] J. Rafiee, X. Mi, H. Gullapalli, A. V. Thomas, F. Yavari, Y. Shi, P. M. Ajayan, and N. A. Koratkar, "Wetting transparency of graphene," *Nature Mat.*, vol. 11, no. 3, pp. 217–222, 2012.

[36] C.-J. Shih, Q. H. Wang, S. Lin, K.-C. Park, Z. Jin, M. S. Strano, and D. Blankschtein, "Breakdown in the wetting transparency of graphene," *Phys. Rev. Lett.*, vol. 109, no. 17, p. 176101, 2012.

[37] B. Ramos-Alvarado, S. Kumar, and G. Peterson, "On the wettability transparency of graphene-coated silicon surfaces," *J. Chem. Phys.*, vol. 144, no. 1, p. 014701, 2016.

[38] B. Ramos-Alvarado, S. Kumar, and G. Peterson, "Wettability transparency and the quasiuniversal relationship between hydrodynamic slip and contact angle," *Appl. Phys. Lett.*, vol. 108, no. 7, p. 074105, 2016.

[39] P. Gong, Z. Ye, L. Yuan, and P. Egberts, "Evaluation of wetting transparency and surface energy of pristine and aged graphene through nanoscale friction," *Carbon*, vol. 132, pp. 749–759, 2018.

[40] J. E. Andrews, S. Sinha, P. W. Chung, and S. Das, "Wetting dynamics of a water nanodrop on graphene," *Phys. Chem. Chem. Phys.*, vol. 18, no. 34, pp. 23482–23493, 2016.

[41] J. Driskill, D. Vanzo, D. Bratko, and A. Luzar, "Wetting transparency of graphene in water," *J. Chem. Phys.*, vol. 141, no. 18, p. 18C517, 2014.

[42] R. Raj, S. C. Maroo, and E. N. Wang, "Wettability of graphene," *Nano Lett.*, vol. 13, no. 4, pp. 1509–1515, 2013.

[43] S.-W. Hung, P.-Y. Hsiao, C.-P. Chen, and C.-C. Chieng, "Wettability of graphene-coated surface: Free energy investigations using molecular dynamics simulation," *J. Phys. Chem. C*, vol. 119, no. 15, pp. 8103–8111, 2015.

[44] D. G. Haywood, A. Saha-Shah, L. A. Baker, and S. C. Jacobson, "Fundamental studies of nanofluidics: nanopores, nanochannels, and nanopipets," *Anal. Chem.*, vol. 87, no. 1, pp. 172–187, 2014.

[45] J. C. Eijkel and A. Van Den Berg, "Nanofluidics: what is it and what can we expect from it?," *Microfluidics and Nanofluidics*, vol. 1, no. 3, pp. 249–267, 2005.

[46] C. Liu and Z. Li, "On the validity of the Navier-Stokes equations for nanoscale liquid flows: The role of channel size," *AIP advances*, vol. 1, no. 3, p. 032108, 2011.

[47] P. Koumoutsakos, R. Jaffe, T. Werder, and J. Walther, "On the validity of the no-slip condition in nanofluidics," *Nanotech*, vol. 1, pp. 148–151, 2003.

[48] J. S. Hansen, J. C. Dyre, P. Daivis, B. D. Todd, and H. Bruus, "Continuum nanofluidics," *Langmuir*, vol. 31, no. 49, pp. 13275–13289, 2015.

[49] J.-L. Barrat *et al.*, "Influence of wetting properties on hydrodynamic boundary conditions at a fluid/solid interface," *Faraday Discuss.*, vol. 112, pp. 119–128, 1999.

[50] L. Bocquet and E. Charlaix, "Nanofluidics, from bulk to interfaces," *Chem. Soc. Rev.*, vol. 39, pp. 1073–1095, 2010.

[51] L. Li, J. Mo, and Z. Li, "Flow and slip transition in nanochannels," *Phys. Rev. E*, vol. 90, no. 3, p. 033003, 2014.

[52] A. Alexiadis and S. Kassinos, "The density of water in carbon nanotubes," *Chem. Eng. Sci.*, vol. 63, no. 8, pp. 2047–2056, 2008.

[53] X. Chen, G. Cao, A. Han, V. K. Punyamurtula, L. Liu, P. J. Culligan, T. Kim, and Y. Qiao, "Nanoscale fluid transport: size and rate effects," *Nano Lett.*, vol. 8, no. 9, pp. 2988–2992, 2008.

[54] E. R. Cruz-Chu, A. Aksimentiev, and K. Schulten, "Water- silica force field for simulating nanodevices," *J. Phys. Chem. B*, vol. 110, no. 43, pp. 21497–21508, 2006.

[55] K. Goh and Y. Chen, "Controlling water transport in carbon nanotubes," *Nano Today*, vol. 14, pp. 13–15, 2017.

[56] J. S. Hansen, B. Todd, and P. J. Daivis, "Prediction of fluid velocity slip at solid surfaces," *Phys. Rev. E*, vol. 84, no. 1, p. 016313, 2011.

[57] J. Janeček and R. R. Netz, "Interfacial water at hydrophobic and hydrophilic surfaces: Depletion versus adsorption," *Langmuir*, vol. 23, no. 16, pp. 8417–8429, 2007.

[58] S. K. Kannam, B. Todd, J. S. Hansen, and P. J. Daivis, "Slip flow in graphene nanochannels," *J. Chem. Phys.*, vol. 135, no. 14, p. 144701, 2011.

[59] N. K. Karna, E. Oyarzua, J. H. Walther, and H. A. Zambrano, "Effect of the meniscus contact angle during early regimes of spontaneous imbibition in nanochannels," *Phys. Chem. Chem. Phys.*, vol. 18, no. 47, pp. 31997–32001, 2016.

[60] E. Kotsalis, J. Walther, and P. Koumoutsakos, "Multiphase water flow inside carbon nanotubes," *Int. J. Multiphase Flow.*, vol. 30, no. 7, pp. 995–1010, 2004.

[61] E. Lauga and H. A. Stone, "Effective slip in pressure-driven stokes flow," *J. Fluid Mech.*, vol. 489, no. 1, pp. 55–77, 2003.

[62] A. Martini, H.-Y. Hsu, N. A. Patankar, and S. Lichter, "Slip at high shear rates," *Phys. Rev. Lett.*, vol. 100, no. 20, p. 206001, 2008.

[63] A. Martini, A. Roxin, R. Snurr, Q. Wang, and S. Lichter, "Molecular mechanisms of liquid slip," *J. Fluid Mech.*, vol. 600, pp. 257–269, 2008.

[64] A. Noy, H. G. Park, F. Fornasiero, J. K. Holt, C. P. Grigoropoulos, and O. Bakajin, "Nanofluidics in carbon nanotubes," *Nano Today*, vol. 2, no. 6, pp. 22–29, 2007.

[65] E. Oyarzua, J. H. Walther, A. Mejia, and Z. H. A., "Early regimes of water capillary flow in slit silica nanochannels," *Phys. Chem. Chem. Phys.*, vol. 17, no. 1, pp. 14731–14739, 2015.

[66] E. Oyarzua, J. H. Walther, C. M. Megaridis, P. Koumoutsakos, and H. A. Zambrano, "Carbon nanotubes as thermally induced water pumps," *ACS Nano.*, vol. 11, no. 10, pp. 9997–10002, 2017.

[67] E. Oyarzua, J. H. Walther, and H. A. Zambrano, "Water thermophoresis in carbon nanotubes: the interplay between thermophoretic and friction forces," *Phys. Chem. Chem. Phys.*, 2018.

[68] S. Prakash, H. A. Zambrano, K. K. Rangharajan, E. Rosenthal-Kim, N. Vasquez, and A. Conlisk, "Electrokinetic transport of monovalent and divalent cations in silica nanochannels," *Microfluid. Nanofluid.*, vol. 20, no. 1, p. 8, 2016.

[69] B. Ramos-Alvarado, S. Kumar, and G. Peterson, "Hydrodynamic slip length as a surface property," *Phys. Rev. E*, vol. 93, no. 2, p. 023101, 2016.

[70] K. Ritos, D. Mattia, F. Calabrò, and J. M. Reese, "Flow enhancement in nanotubes of different materials and lengths," *J. Chem. Phys.*, vol. 140, no. 1, p. 014702, 2014.

[71] G. Scocchi, D. Sergi, C. D'Angelo, and A. Ortona, "Wetting and contact-line effects for spherical and cylindrical droplets on graphene layers: A comparative molecular-dynamics investigation," *Phys. Rev. E*, vol. 84, no. 6, p. 061602, 2011.

[72] E. Secchi, S. Marbach, A. Nigues, D. Stein, A. Siria, and L. Bocquet, "Molecular transport through capillaries made with atomic-scale precision," *Nature*, vol. 537, no. 7619, pp. 210–213, 2016.

[73] J. J. Thalakkottor and K. Mohseni, "Unified slip boundary condition for fluid flows," *Phys. Rev. E*, vol. 94, no. 2, p. 023113, 2016.

[74] J. A. Thomas and A. J. McGaughey, "Water flow in carbon nanotubes: transition to subcontinuum transport," *Phys. Rev. Lett.*, vol. 102, no. 18, p. 184502, 2009.

[75] T. Ondarçuhu and J.-P. Aimé, *Nanoscale liquid interfaces: Wetting, patterning and force microscopy at the molecular scale*. CRC Press, 2013.

[76] L. Schimmele, M. Napiórkowski, and S. Dietrich, "Conceptual aspects of line tensions," *J. Chem. Phys.*, vol. 127, no. 16, p. 164715, 2007.

[77] J. Drelich, "The significance and magnitude of the line tension in three-phase (solid-liquid-fluid) systems," *Coll. Surf. A*, vol. 116, no. 1-2, pp. 43–54, 1996.

[78] J. H. Weijs, A. Marchand, B. Andreotti, D. Lohse, and J. H. Snoeijer, "Origin of line tension for a lennard-jones nanodroplet," *Phys. Fluids*, vol. 23, no. 2, p. 022001, 2011.

[79] H. Peng, G. R. Birkett, and A. V. Nguyen, "The impact of line tension on the contact angle of nanodroplets," *Mol. Sim.*, vol. 40, no. 12, pp. 934–941, 2014.

[80] T. Werder, J. H. Walther, R. L. Jaffe, T. Halicioglu, and P. Koumoutsakos, "On the water-graphite interaction for use in MD simulations of graphite and carbon nanotubes," *J. Phys. Chem. B*, vol. 107, pp. 1345–1352, 2003.

[81] J. N. Israelachvili, *Intermolecular and surface forces*. Academic press, 2011.

[82] P. A. Thiel and T. E. Madey, "The interaction of water with solid surfaces: fundamental aspects," *Surface Science Reports*, vol. 7, no. 6-8, pp. 211–385, 1987.

[83] A. Berezhkovskii and G. Hummer, "Single-file transport of water molecules through a carbon nanotube," *Phys. Rev. Lett.*, vol. 89, no. 6, p. 064503, 2002.

[84] C.-H. Choi, J. A. Westin, and K. S. Breuer, "Apparent slip flows in hydrophilic and hydrophobic microchannels," *Phys. Fluids*, vol. 15, no. 10, pp. 2897–2902, 2003.

[85] D. C. Tretheway and C. D. Meinhart, "Apparent fluid slip at hydrophobic microchannel walls," *Phys. Fluids*, vol. 14, no. 3, pp. L9–L12, 2002.

[86] M. Griebel, S. Knapek, and G. Zumbusch, "Numerical simulation in molecular dynamics. numerics, algorithms, parallelization, applications, volume 5 of texts in computational science and engineering," 2007.

[87] C. Neto, D. R. Evans, E. Bonaccurso, H.-J. Butt, and V. S. Craig, "Boundary slip in Newtonian liquids: a review of experimental studies," *Reports on Progress in Physics*, vol. 68, no. 12, p. 2859, 2005.

[88] C.-H. Choi, K. J. A. Westin, and K. S. Breuer, "To slip or not to slip: Water flows in hydrophilic and hydrophobic microchannels," in *ASME 2002 International Mechanical Engineering Congress and Exposition*, pp. 557–564, American Society of Mechanical Engineers, 2002.

[89] R. S. Voronov, D. V. Papavassiliou, and L. L. Lee, "Boundary slip and wetting properties of interfaces: correlation of the contact angle with the slip length," *J. Chem. Phys.*, vol. 124, no. 20, p. 204701, 2006.

[90] F.-C. Wang and Y.-P. Zhao, "Slip boundary conditions based on molecular kinetic theory: The critical shear stress and the energy dissipation at the liquid–solid interface," *Soft Matter*, vol. 7, no. 18, pp. 8628–8634, 2011.

[91] H. Bruus, "Theoretical microfluidics. oxford master series in condensed matter physics," 2008.

[92] C. Navier, "Mémoire sur les lois du mouvement des fluides," *Mémoires de l'Académie Royale des Sciences de l'Institut de France*, vol. 6, no. 1823, pp. 389–440, 1823.

[93] V. S. Craig, C. Neto, and D. R. Williams, "Shear-dependent boundary slip in an aqueous Newtonian liquid," *Phys. Rev. Lett.*, vol. 87, no. 5, p. 054504, 2001.

[94] W. Choi and J.-w. Lee, *Graphene: Synthesis and Applications*. CRC press, 2016.

[95] M. Monthioux and V. L. Kuznetsov, "Who should be given the credit for the discovery of carbon nanotubes?," *Carbon*, vol. 44, no. 9, pp. 1621–1623, 2006.

[96] S. Iijima, "Helical microtubules of graphitic carbon," *Nature*, vol. 354, no. 6348, p. 56, 1991.

[97] K. S. Novoselov, A. K. Geim, S. V. Morozov, D. Jiang, Y. Zhang, S. V. Dubonos, I. V. Grigorieva, and A. A. Firsov, "Electric field effect in atomically thin carbon films," *Science*, vol. 306, no. 5696, pp. 666–669, 2004.

[98] K. Novoselov, A. K. Geim, S. Morozov, D. Jiang, M. Katsnelson, I. Grigorieva, S. Dubonos, and A. Firsov, "Two-dimensional gas of massless dirac fermions in graphene," *Nature*, vol. 438, no. 7065, pp. 197–200, 2005.

[99] H.-S. P. Wong and D. Akinwande, *Carbon nanotube and graphene device physics*. Cambridge University Press, 2011.

[100] A. K. Geim and K. S. Novoselov, "The rise of graphene," *Nature Materials*, vol. 6, no. 3, pp. 183–191, 2007.

[101] M. J. Allen, V. C. Tung, and R. B. Kaner, "Honeycomb carbon: a review of graphene," *Chemical Reviews.*, vol. 110, no. 1, pp. 132–145, 2009.

[102] D. Das and H. Rahaman, *Carbon nanotube and graphene nanoribbon interconnects*. Crc Press, 2014.

[103] E. Malic and A. Knorr, *Graphene and Carbon Nanotubes: Ultrafast Optics and Relaxation Dynamics*. John Wiley & Sons, 2013.

[104] B. Anasori, M. R. Lukatskaya, and Y. Gogotsi, "2D metal carbides and nitrides (mxenes) for energy storage," *Nature Reviews Materials*, vol. 2, no. 2, p. 16098, 2017.

[105] M. Xu, T. Liang, M. Shi, and H. Chen, "Graphene-like two-dimensional materials," *Chemical Reviews.*, vol. 113, no. 5, pp. 3766–3798, 2013.

[106] E. Hwang, S. Adam, and S. D. Sarma, "Carrier transport in two-dimensional graphene layers," *Phys. Rev. Lett.*, vol. 98, no. 18, p. 186806, 2007.

[107] A. A. Balandin, S. Ghosh, W. Bao, I. Calizo, D. Teweldebrhan, F. Miao, and C. N. Lau, "Superior thermal conductivity of single-layer graphene," *Nano Lett.*, vol. 8, no. 3, pp. 902–907, 2008.

[108] Y. Xu, H. Bai, G. Lu, C. Li, and G. Shi, "Flexible graphene films via the filtration of water-soluble noncovalent functionalized graphene sheets," *J. Am. Chem. Soc.*, vol. 130, no. 18, pp. 5856–5857, 2008.

[109] A. Kuzmenko, E. Van Heumen, F. Carbone, and D. Van Der Marel, "Universal optical conductance of graphite," *Phys. Rev. Lett.*, vol. 100, no. 11, p. 117401, 2008.

[110] A. K. Geim, "Graphene: status and prospects," *Science*, vol. 324, no. 5934, pp. 1530–1534, 2009.

[111] K. I. Tserpes and N. Silvestre, *Modeling of carbon nanotubes, graphene and their composites*. Springer, 2014.

[112] M. C. G. Lim and Z. Zhong, *Carbon Nanotubes as Nanodelivery Systems: An Insight Through Molecular Dynamics Simulations*. Springer Science & Business Media, 2013.

[113] Y. Mao, X. Yan, Y. Xiao, J. Xiang, Y. Yang, and H. Yu, "The viability of 0.3 nm diameter carbon nanotubes," *Nanotechnol.*, vol. 15, no. 8, p. 1000, 2004.

[114] V. K. Thakur and M. K. Thakur, *Chemical functionalization of carbon nanomaterials: Chemistry and Applications*. CRC Press, 2015.

[115] Y. Wu, X. Zhang, A. Leung, and W. Zhong, "An energy-equivalent model on studying the mechanical properties of single-walled carbon nanotubes," *Thin-Walled Structures*, vol. 44, no. 6, pp. 667–676, 2006.

[116] J. K. Holt, H. G. Park, Y. Wang, M. Stadermann, A. B. Artyukhin, C. P. Grigoropoulos, A. Noy, and O. Bakajin, "Fast mass transport through sub-2-nanometer carbon nanotubes," *Science*, vol. 312, no. 5776, pp. 1034–1037, 2006.

[117] K. Wu, Z. Chen, J. Li, J. Xu, and X. Dong, "Wettability effect on nanoconfined water flow," *Proc. Natl. Acad. Sci. USA*, vol. 114, no. 13, pp. 3358–3363, 2017.

[118] W. Xiong, J. Z. Liu, M. Ma, Z. Xu, J. Sheridan, and Q. Zheng, "Strain engineering water transport in graphene nanochannels," *Phys. Rev. E*, vol. 84, no. 5, p. 056329, 2011.

[119] C.-J. Shih, M. S. Strano, and D. Blankschtein, "Wetting translucency of graphene," *Nature Mat.*, vol. 12, no. 10, pp. 866–869, 2013.

[120] A. Ashraf, Y. Wu, M. C. Wang, K. Yong, T. Sun, Y. Jing, R. T. Haasch, N. R. Aluru, and S. Nam, "Doping-induced tunable wettability and adhesion of graphene," *Nano Lett.*, vol. 16, no. 7, pp. 4708–4712, 2016.

[121] G. Hong, Y. Han, T. M. Schutzius, Y. Wang, Y. Pan, M. Hu, J. Jie, C. S. Sharma, U. Müller, and D. Poulikakos, "On the mechanism of hydrophilicity of graphene," *Nano Lett.*, vol. 16, no. 7, pp. 4447–4453, 2016.

[122] H. Aoki and M. S. Dresselhaus, *Physics of graphene*. Springer Science & Business Media, 2013.

[123] R. R. Schaller, "Moore's law: past, present and future," *IEEE spectrum*, vol. 34, no. 6, pp. 52–59, 1997.

[124] H. J. Berendsen, *Simulating the physical world: hierarchical modeling from quantum mechanics to fluid dynamics*. Cambridge University Press, 2007.

[125] J. Barker, R. Fisher, and R. Watts, "Liquid argon: Monte carlo and molecular dynamics calculations," *Molecular Physics*, vol. 21, no. 4, pp. 657–673, 1971.

[126] A. Trokhymchuk and J. Alejandre, "Computer simulations of liquid/vapor interface in lennard-jones fluids: Some questions and answers," *J. Chem. Phys.*, vol. 111, no. 18, pp. 8510–8523, 1999.

[127] F. Zhu, E. Tajkhorshid, and K. Schulten, "Theory and simulation of water permeation in aquaporin-1," *Biophysical Journal*, vol. 86, no. 1, pp. 50–57, 2004.

[128] T. I. Cheatham, J. Miller, T. Fox, T. Darden, and P. Kollman, "Molecular dynamics simulations on solvated biomolecular systems: the particle mesh Ewald method leads to stable trajectories of dna, rna, and proteins," *J. Am. Chem. Soc.*, vol. 117, no. 14, pp. 4193–4194, 1995.

[129] H. Wong, H. Marie-Nelly, S. Herbert, P. Carrivain, H. Blanc, R. Koszul, E. Fabre, and C. Zimmer, "A predictive computational model of the dynamic 3d interphase yeast nucleus," *Current biology*, vol. 22, no. 20, pp. 1881–1890, 2012.

[130] D. C. Rapaport and D. C. R. Rapaport, *The art of molecular dynamics simulation*. Cambridge university press, 2004.

[131] W. F. van Gunsteren and H. J. Berendsen, "Computer simulation of molecular dynamics: methodology, applications, and perspectives in chemistry," *Angewandte Chemie International Edition in English*, vol. 29, no. 9, pp. 992–1023, 1990.

[132] A. Hospital, J. R. Goñi, M. Orozco, and J. L. Gelpí, "Molecular dynamics simulations: advances and applications," *Advances and applications in bioinformatics and chemistry: AABC*, vol. 8, p. 37, 2015.

[133] M. Karplus and J. A. McCammon, "Molecular dynamics simulations of biomolecules," *Nature Structural and Molecular Biology*, vol. 9, no. 9, p. 646, 2002.

[134] T. Norton and D.-W. Sun, "Computational fluid dynamics (cfd)–an effective and efficient design and analysis tool for the food industry: a review," *Trends in Food Science & Technology*, vol. 17, no. 11, pp. 600–620, 2006.

[135] B. Sanderse, S. Pijl, and B. Koren, "Review of computational fluid dynamics for wind turbine wake aerodynamics," *Wind energy*, vol. 14, no. 7, pp. 799–819, 2011.

[136] M. M. A. Bhutta, N. Hayat, M. H. Bashir, A. R. Khan, K. N. Ahmad, and S. Khan, "Cfd applications in various heat exchangers design: A review," *Appl. Thermal Engng.*, vol. 32, pp. 1–12, 2012.

[137] K. P. Travis, B. Todd, and D. J. Evans, "Departure from Navier-Stokes hydrodynamics in confined liquids," *Phys. Rev. E*, vol. 55, no. 4, p. 4288, 1997.

[138] M. J. Field, *A practical introduction to the simulation of molecular systems*. Cambridge University Press, 1999.

[139] F. Jensen, *Introduction to computational chemistry*. John wiley & sons, 2007.

[140] A. R. Leach, *Molecular modelling: principles and applications*. Pearson education, 2001.

[141] A. Stone, *The theory of intermolecular forces*. OUP Oxford, 2013.

[142] B. Alder and T. Wainwright, "Phase transition for a hard sphere system," *J. Chem. Phys.*, vol. 27, no. 5, pp. 1208–1209, 1957.

[143] S.-T. Lin, M. Blanco, and W. A. Goddard III, "The two-phase model for calculating thermodynamic properties of liquids from molecular dynamics: Validation for the phase diagram of lennard-jones fluids," *J. Chem. Phys.*, vol. 119, no. 22, pp. 11792–11805, 2003.

[144] M. A. González and J. L. Abascal, "The shear viscosity of rigid water models," *J. Chem. Phys.*, vol. 132, no. 9, p. 096101, 2010.

[145] M. Matsumoto, S. Saito, and I. Ohmine, "Molecular dynamics simulation of the ice nucleation and growth process leading to water freezing," *Nature*, vol. 416, no. 6879, p. 409, 2002.

[146] J. R. Ray and A. Rahman, "Statistical ensembles and molecular dynamics studies of anisotropic solids," *J. Chem. Phys.*, vol. 80, no. 9, pp. 4423–4428, 1984.

[147] M. Parrinello and A. Rahman, "Crystal structure and pair potentials: A molecular-dynamics study," *Phys. Rev. Lett.*, vol. 45, no. 14, p. 1196, 1980.

[148] J. Han and H. G. Craighead, "Separation of long dna molecules in a microfabricated entropic trap array," *Science*, vol. 288, no. 5468, pp. 1026–1029, 2000.

[149] J. Koplik, J. R. Banavar, and J. F. Willemsen, "Molecular dynamics of fluid flow at solid surfaces," *Phys. Fluids A*, vol. 1, no. 5, pp. 781–794, 1989.

[150] J. H. Walther, R. Jaffe, T. Halicioglu, and P. Koumoutsakos, "Carbon nanotubes in water: Structural characteristics and energetics," *J. Phys. Chem. B*, vol. 105, pp. 9980–9987, 2001.

[151] T. Werder, J. H. Walther, R. L. Jaffe, T. Halicioglu, F. Noca, and P. Koumoutsakos, "Molecular dynamics simulation of contact angles of water droplets in carbon nanotubes," *Nano Lett.*, vol. 1, no. 12, pp. 697–702, 2001.

[152] H. A. Zambrano, J. H. Walther, and R. L. Jaffe, "Thermally driven molecular linear motors: a molecular dynamics study," *J. Chem. Phys.*, vol. 131, no. 24, p. 241104, 2009.

[153] H. A. Zambrano, J. H. Walther, P. Koumoutsakos, and I. F. Sbalzarini, "Thermophoretic motion of water nanodroplets confined inside carbon nanotubes," *Nano Lett.*, vol. 9, no. 1, pp. 66–71, 2009.

[154] H. A. Zambrano, N. Vásquez, and E. Wagemann, "Wall embedded electrodes to modify electroosmotic flow in silica nanoslits," *Phys. Chem. Chem. Phys.*, vol. 18, no. 2, pp. 1202–1211, 2016.

[155] W. F. Van Gunsteren and H. Berendsen, "A leap-frog algorithm for stochastic dynamics," *Mol. Sim.*, vol. 1, no. 3, pp. 173–185, 1988.

[156] H. J. C. Berendsen, J. P. M. Postma, W. F. van Gunsteren, A. DiNola, and J. R. Haak, "Molecular dynamics with coupling to an external bath," *J. Chem. Phys.*, vol. 81, no. 8, pp. 3684–3684, 1984.

[157] L. Greengard, "The numerical solution of the n-body problem," *Computers in Physics*, vol. 4, no. 2, pp. 142–152, 1990.

[158] L. Verlet, "Computer "experiments" on classical fluids. i. thermodynamical properties of lennard-jones molecules," *Phys. Rev.*, vol. 159, no. 1, p. 98, 1967.

[159] A. Y. Toukmaji and J. A. Board Jr, "Ewald summation techniques in perspective: a survey," *Computer physics communications*, vol. 95, no. 2-3, pp. 73–92, 1996.

[160] T. Darden, D. York, and L. Pedersen, "Particle mesh Ewald: An n log (n) method for Ewald sums in large systems," *J. Chem. Phys.*, vol. 98, no. 12, pp. 10089–10092, 1993.

[161] U. Essmann, L. Perera, M. L. Berkowitz, T. Darden, H. Lee, and L. G. Pedersen, "A smooth particle mesh Ewald method," *J. Chem. Phys.*, vol. 103, no. 19, pp. 8577–8593, 1995.

[162] H. A. Stone, A. D. Stroock, and A. Ajdari, "Engineering flows in small devices: microfluidics toward a lab-on-a-chip," *Annu. Rev. Fluid Mech.*, vol. 36, pp. 381–411, 2004.

[163] R. Daw and J. Finkelstein, "Lab on a chip," *Nature*, vol. 442, no. 7101, pp. 367–367, 2006.

[164] C. D. Chin, V. Linder, and S. K. Sia, "Lab-on-a-chip devices for global health: Past studies and future opportunities," *Lab on a Chip*, vol. 7, no. 1, pp. 41–57, 2007.

[165] H. Craighead, "Future lab-on-a-chip technologies for interrogating individual molecules," *Nature*, vol. 442, no. 7101, pp. 387–393, 2006.

[166] C. Duan, W. Wang, and Q. Xie, "Review article: Fabrication of nanofluidic devices," *Biomicrofluidics*, vol. 7, no. 2, pp. 1–41, 2013.

[167] P. Kral and B. Wang, "Material drag phenomena in nanotubes," *Chemical Reviews.*, vol. 113, no. 5, pp. 3372–3390, 2013.

[168] L. H. Thamdrup, K. F. Persson, H. Bruus, A. Kristensen, and H. Flyvbjerg, "Experimental investigation of bubble formation during capillary filling of SiO2 nanoslits," *Appl. Phys. Lett.*, vol. 91, no. 16, pp. 1–3, 2007.

[169] C. Bakli and S. Chakraborty, "Slippery to sticky transition of hydrophobic nanochannels," *Nano Lett.*, vol. 15, no. 11, pp. 7497–7502, 2015.

[170] T. A. Ho, D. V. Papavassiliou, L. L. Lee, and A. Striolo, "Liquid water can slip on a hydrophilic surface," *Proc. Natl. Acad. Sci. USA*, vol. 108, no. 39, pp. 16170–16175, 2011.

[171] T. Q. Vo and B. Kim, "Transport phenomena of water in molecular fluidic channels," *Scientific Reports*, vol. 6, 2016.

[172] B. Radha, A. Esfandiar, F. Wang, A. Rooney, K. Gopinadhan, A. Keerthi, A. Mishchenko, A. Janardanan, P. Blake, L. Fumagalli, *et al.*, "Molecular transport through capillaries made with atomic-scale precision," *Nature*, vol. 538, no. 7624, pp. 222–225, 2016.

[173] C. Almeida, V. Carozo, R. Prioli, and C. Achete, "Identification of graphene crystallographic orientation by atomic force microscopy," *J. Appl. Phys.*, vol. 110, no. 8, p. 086101, 2011.

[174] S. Stankovich, D. A. Dikin, G. H. Dommett, K. M. Kohlhaas, E. J. Zimney, E. A. Stach, R. D. Piner, S. T. Nguyen, and R. S. Ruoff, "Graphene-based composite materials," *Nature*, vol. 442, no. 7100, pp. 282–286, 2006.

[175] X. Li, X. Wang, L. Zhang, S. Lee, and H. Dai, "Chemically derived, ultrasmooth graphene nanoribbon semiconductors," *Science*, vol. 319, no. 5867, pp. 1229–1232, 2008.

[176] M. D. Stoller, S. Park, Y. Zhu, J. An, and R. S. Ruoff, "Graphene-based ultracapacitors," *Nano Lett.*, vol. 8, no. 10, pp. 3498–3502, 2008.

[177] H. Li, L. Zou, L. Pan, and Z. Sun, "Novel graphene-like electrodes for capacitive deionization," *Environ. Sci. Technol.*, vol. 44, no. 22, pp. 8692–8697, 2010.

[178] V. Chandra, J. Park, Y. Chun, J. W. Lee, I.-C. Hwang, and K. S. Kim, "Water-dispersible magnetite-reduced graphene oxide composites for arsenic removal," *ACS nano*, vol. 4, no. 7, pp. 3979–3986, 2010.

[179] D. Cohen-Tanugi, L.-C. Lin, and J. C. Grossman, "Multilayer nanoporous graphene membranes for water desalination," *Nano Lett.*, vol. 16, no. 2, pp. 1027–1033, 2016.

[180] E. Lauga, M. Brenner, and H. Stone, *Microfluidics: the no-slip boundary condition*. Springer, 2007.

[181] M. T. Matthews and J. M. Hill, "A note on the boundary layer equations with linear slip boundary condition," *Applied Mathematics Letters*, vol. 21, no. 8, pp. 810–813, 2008.

[182] A. H. Palser, "Interlayer interactions in graphite and carbon nanotubes," *Phys. Chem. Chem. Phys.*, vol. 1, no. 18, pp. 4459–4464, 1999.

[183] M. Sega, M. Sbragaglia, L. Biferale, and S. Succi, "The importance of chemical potential in the determination of water slip in nanochannels," *Eur. Phys. J. E*, vol. 38, no. 11, pp. 1–7, 2015.

[184] H. J. C. Berendsen, J. R. Grigera, and T. P. Straatsma, "The missing term in effective pair potentials," *J. Phys. Chem.*, vol. 91, pp. 6269–6271, 1987.

[185] L. Xia, C. Choi, S. C. Kothekar, and D. Dutta, "On-chip pressure generation for driving liquid phase separations in nanochannels," *Anal. Chem.*, vol. 88, no. 1, pp. 781–788, 2015.

[186] M. D. Ma, L. Shen, J. Sheridan, J. Z. Liu, C. Chen, and Q. Zheng, "Friction of water slipping in carbon nanotubes," *Phys. Rev. E*, vol. 83, no. 3, p. 036316, 2011.

[187] M. Sega, M. Sbragaglia, L. Biferale, and S. Succi, "Regularization of the slip length divergence in water nanoflows by inhomogeneities at the Angstrom scale," *Soft Matter*, vol. 9, no. 35, pp. 8526–8531, 2013.

[188] A. Maali, T. Cohen-Bouhacina, and H. Kellay, "Measurement of the slip length of water flow on graphite surface," *Appl. Phys. Lett.*, vol. 92, no. 5, p. 053101, 2008.

[189] N. V. Priezjev and S. M. Troian, "Molecular origin and dynamic behavior of slip in sheared polymer films," *Phys. Rev. Lett.*, vol. 92, no. 1, p. 018302, 2004.

[190] R. Saito, R. Matsuo, T. Kimura, G. Dresselhaus, and M. Dresselhaus, "Anomalous potential barrier of double-wall carbon nanotube," *Chem. Phys. Lett.*, vol. 348, no. 3, pp. 187–193, 2001.

[191] L. Girifalco, M. Hodak, and R. S. Lee, "Carbon nanotubes, buckyballs, ropes, and a universal graphitic potential," *Phys. Rev. B*, vol. 62, no. 19, p. 13104, 2000.

[192] N. V. Priezjev and S. M. Troian, "Influence of periodic wall roughness on the slip behaviour at liquid/solid interfaces: molecular-scale simulations versus continuum predictions," *Journal of Fluid Mechanics*, vol. 554, pp. 25–46, 2006.

[193] Y.-C. Liu, J.-W. Shen, K. E. Gubbins, J. D. Moore, T. Wu, and Q. Wang, "Diffusion dynamics of water controlled by topology of potential energy surface inside carbon nanotubes," *Phys. Rev. B*, vol. 77, no. 12, p. 125438, 2008.

[194] D. Mijatovic, J. Eijkel, and A. van den Berg, "Technologies for nanofluidic systems: top-down vs bottom-up a review," *Lab on a Chip*, vol. 5, pp. 492–500, 2005.

[195] M. L. Kovarik and S. C. Jacobson, "Attoliter-scale dispensing in nanofluidic channels," *Anal. Chem.*, vol. 79, no. 4, pp. 1655–1660, 2007.

[196] D. Mark, S. Haeberle, G. Roth, F. von Stetten, and R. Zengerle, "Microfluidic lab-on-a-chip platforms: requirements, characteristics and applications," *Chem. Soc. Rev.*, vol. 39, no. 3, pp. 1153–1182, 2010.

[197] S.-W. Nam, , M. J. Rooks, , K.-B. Kim, and S. M. Rossnagel, "Ionic field effect transistors with sub-10 nm multiple nanopores," *Nano Lett.*, vol. 9, no. 5, pp. 2044–2048, 2009.

[198] H. Amiri, K. L. Shepard, C. Nuckolls, and R. Hernández Sánchez, "Single-walled carbon nanotubes: Mimics of biological ion channels," *Nano Lett.*, vol. 17, no. 2, pp. 1204–1211, 2017.

[199] B. Corry, "Designing carbon nanotube membranes for efficient water desalination," *J. Phys. Chem. B*, vol. 112, no. 5, pp. 1427–1434, 2008.

[200] M. Wanunu, "Nanopores: A journey towards DNA sequencing," *Physics of life reviews*, vol. 9, no. 2, pp. 125–158, 2012.

[201] O. C. Farokhzad and R. Langer, "Impact of nanotechnology on drug delivery," *ACS Nano.*, vol. 3, no. 1, pp. 16–20, 2009.

[202] Q. Xie, M. A. Alibakhshi, S. Jiao, Z. Xu, M. Hempel, J. Kong, H. G. Park, and C. Duan, "Fast water transport in graphene nanofluidic channels," *Nature Nanotechnol.*, p. 1, 2018.

[203] M. A. Alibakhshi, Q. Xie, Y. Li, and C. Duan, "Accurate measurement of liquid transport through nanoscale conduits," *Scientific reports*, vol. 6, pp. 1–8, 2016.

[204] D. Ortiz-Young, H.-C. Chiu, S. Kim, K. Voïtchovsky, and E. Riedo, "The interplay between apparent viscosity and wettability in nanoconfined water," *Nature Communications*, vol. 4, no. 2482, pp. 1–6, 2013.

[205] U. Raviv, P. Laurat, and J. Klein, "Fluidity of water confined to subnanometre films," *Nature*, vol. 413, pp. 51–54, 2001.

[206] O. Bjorneholm, M. H. Hansen, A. Hodgson, L.-M. Liu, D. T. Limmer, A. Michaelides, P. Pedevilla, J. Rossmeisl, H. Shen, G. Tocci, E. Tyrode, M.-M. Walz, J. Werner, and H. Bluhm, "Water at interfaces," *Chemical Reviews.*, vol. 116, no. 13, pp. 7698–7726, 2016.

[207] A. Bandopadhyay, S. S. Hossain, and S. Chakraborty, "Ionic size dependent electroviscous effects in ion-selective nanopores," *Langmuir*, vol. 30, no. 24, pp. 7251–7258, 2014.

[208] E. Secchi, S. Marbach, A. Niguès, A. Siria, and L. Bocquet, "The landau–squire plume," *J. Fluid Mech.*, vol. 826, 2017.

[209] X. Wei and T. Luo, "Effects of electrostatic interaction and chirality on the friction coefficient of water flow inside single-walled carbon nanotubes and boron nitride nanotubes," *J. Phys. Chem. C*, vol. 122, no. 9, pp. 5131–5140, 2018.

[210] J. Su and H. Guo, "Effect of nanochannel dimension on the transport of water molecules," *J. Phys. Chem. B*, vol. 116, no. 20, pp. 5925–5932, 2012.

[211] R. Khare, J. de Pablo, and A. Yethiraj, "Molecular simulation and continuum mechanics study of simple fluids in non-isothermal planar couette flows," *J. Chem. Phys.*, vol. 107, no. 7, pp. 2589–2596, 1997.

[212] V. P. Sokhan, D. Nicholson, and N. Quirke, "Fluid flow in nanopores: Accurate boundary conditions for carbon nanotubes," *J. Chem. Phys.*, vol. 117, no. 18, pp. 8531–8539, 2002.

[213] S. Bernardi, B. D. Todd, and D. J. Searles, "Thermostating highly confined fluids," *J. Chem. Phys.*, vol. 132, no. 24, p. 244706, 2010.

[214] V. P. Sokhan, D. Nicholson, and N. Quirke, "Fluid flow in nanopores: An examination of hydrodynamic boundary conditions," *J. Chem. Phys.*, vol. 115, no. 8, pp. 3878–3887, 2001.

[215] A. Chakradhar, N. Sivapragasam, M. T. Nayakasinghe, and U. Burghaus, "Support effects in the adsorption of water on cvd graphene: an ultra-high vacuum adsorption study," *Chem. Commun.*, vol. 51, no. 57, pp. 11463–11466, 2015.

[216] Y. Guissani and B. Guillot, "A numerical investigation of the liquid-vapor coexistence curve of silica," *J. Chem. Phys.*, vol. 104, no. 19, pp. 7633–7644, 1996.

[217] S. Tsuneyuki, M. Tsukada, H. Aoki, and Y. Matsui, "First-principles interatomic potential of silica applied to molecular dynamics," *Phys. Rev. Lett.*, vol. 61, no. 7, pp. 869–874, 1988.

[218] H. Zambrano, J. H. Walther, and R. Jaffe, "Molecular dynamics simulations of water on a hydrophilic silica surface at high air pressures," *J. Mol. Liq.*, vol. 198, pp. 107–113, 2014.

[219] Z. Zhang and T. Li, "A molecular mechanics study of morphologic interaction between graphene and si nanowires on a sio 2 substrate," *Journal of Nanomat.*, vol. 2011, pp. 1–7, 2011.

[220] I.-C. Yeh and M. L. Berkowitz, "Ewald summation for systems with slab geometry," *J. Chem. Phys.*, vol. 111, no. 7, pp. 3155–3162, 1999.

[221] F. Taherian, V. Marcon, N. F. van der Vegt, and F. Leroy, "What is the contact angle of water on graphene?," *Langmuir*, vol. 29, no. 5, pp. 1457–1465, 2013.

[222] P. K. Lee, H. Leese, and D. Mattia, "Water flow enhancement in hydrophilic nanochannels," *Nanoscale*, vol. 4, no. 8, pp. 2621–2627, 2012.

[223] W. R. Sanhai, J. H. Sakamoto, R. Canady, and M. Ferrari, "Seven challenges for nanomedicine," *Nature Nanotechnol.*, vol. 3, no. 5, p. 242, 2008.

[224] J. Geske and M. Vogel, "Creating realistic silica nanopores for molecular dynamics simulations," *Mol. Sim.*, vol. 43, no. 1, pp. 13–18, 2017.

[225] M. Rovere, M. Ricci, D. Vellati, and F. Bruni, "A molecular dynamics simulation of water confined in a cylindrical sio 2 pore," *J. Chem. Phys.*, vol. 108, no. 23, pp. 9859–9867, 1998.

[226] J. E. Andrews, Y. Wang, S. Sinha, P. W. Chung, and S. Das, "Roughness-induced chemical heterogeneity leads to large hydrophobicity in wetting-translucent nanostructures," *J. Phys. Chem. C*, vol. 121, no. 18, pp. 10010–10017, 2017.

[227] W. Humphrey, A. Dalke, and K. Schulten, "VMD: visual molecular dynamics," *J. Mol. Graph.*, vol. 14, no. 1, pp. 33–38, 1996.

[228] A. A. Hassanali and S. J. Singer, "Model for the water- amorphous silica interface: The undissociated surface," *J. Phys. Chem. B*, vol. 111, no. 38, pp. 11181–11193, 2007.

[229] J.-P. Ryckaert, G. Ciccotti, and H. J. Berendsen, "Numerical integration of the cartesian equations of motion of a system with constraints: molecular dynamics of n-alkanes," *J. Comput. Phys.*, vol. 23, no. 3, pp. 327–341, 1977.

[230] Y. Quo, N. Karasawa, and W. A. Goddard III, "Prediction of fullerene packing in C60 and C70 crystals," *Nature*, vol. 351, no. 6326, p. 464, 1991.

[231] A. K. Rappé, C. J. Casewit, K. Colwell, W. Goddard Iii, and W. Skiff, "UFF, a full periodic table force field for molecular mechanics and molecular dynamics simulations," *J. Am. Chem. Soc.*, vol. 114, no. 25, pp. 10024–10035, 1992.